Characterization of Image Quality for 3D Scatter Corrected Breast CT Images

by

Jan Harwin Pachon

Graduate Program In Medical Physics
Duke University

Date:_____

Approved:

_____
Martin Tornai, Supervisor

_____
Joseph Lo

_____
James Dobbins III

Thesis submitted in partial fulfillment of
the requirements for the degree of Master of Science in the Graduate Program in
Medical Physics in the Graduate School
of Duke University

2012

ABSTRACT

Characterization of Image Quality for 3D Scatter Corrected Breast CT Images

by

Jan Harwin Pachon

Graduate Program In Medical Physics
Duke University

Date:_____

Approved:

_____
Martin Tornai, Supervisor

_____
Joseph Lo

_____
James Dobbins III

An abstract of a thesis submitted in partial fulfillment of
the requirements for the degree of Master of Science in the Graduate Program in
Medical Physics in the Graduate School
of Duke University

2012

Copyright by
Jan Harwin Pachon
2012

Abstract

The goal of this study was to characterize the image quality of a dedicated, quasi-monochromatic x-ray spectrum, cone beam breast imaging system under scatter corrected and non-scatter corrected conditions for a variety of simulated breast compositions. Computed tomography (CT) projections were acquired of a breast phantom containing two concentric sets of acrylic spheres that varied in size (1-8mm) based on their azimuthal position. A 700 ml breast phantom was filled with 3 different concentrations of methanol and water, simulating a wide range of breast densities. Acrylic yarn was sometimes included to simulate the structural components and connective tissue of a breast. For each phantom condition, 2D scatter was measured for 360° of projection angles. Scatter correction was performed and scatter-corrected and uncorrected projections were then reconstructed with an iterative ordered subsets convex (OSC) algorithm. Reconstructed image quality of various phantom configurations and (non)corrected conditions was characterized using line profiles, non-uniformity index, signal-to-noise ratio (SNR) and contrast analysis. A human observer detection task and a two alternative forced choice (2-AFC) study for the spheres in the different concentric rings were used to determine the effects of scatter correction on signal detection. Line profiles, non-uniformity calculations, and contrast results consistently show that scatter correction effectively reduces the cupping artifact and

improves image contrast for the three concentrations used. SNR results indicate higher noise, and thus lower overall SNR, for the scatter corrected images in the lower density background. SNR of signals was found to be independent of scatter correction for the higher density background. Results from the observer study indicate that there was no statistical difference in the number or sizes of lesions observed in the scatter versus non-scatter corrected images for all densities. Results of the 2-AFC study indicate that for the lower density concentration, scatter correction did not play a role in the probability of detection of spheres greater than 3 mm for the inner radius and 2 mm for the outer radius, but it was effective in improving performance for spheres less than 2 mm for both the inner and outer radii. For the higher density, scatter correction was found to improve the detectability of spheres greater than 3 mm for the inner radius and greater than 2 mm for the outer radius. The statistical analysis of the 2-AFC study did however find that the overall effect of scatter correction was marginal though the combined effect of scatter correction and size was not significant except for 4 mm sphere across the densities examined.

While the results of the observer study are ambiguous as to whether scatter correction significantly improves signal detection, we believe applying scatter correction for differing breast conditions improves overall image quality and is recommended for subsequent use.

Dedication

To my son, Aiden Alexander, for inspiring and motivating me every day. Also to my family for their support through it all. Last but not least, this work is dedicated to my Grandmother Anna Pachon.

Te extrano mucho abuelita,

gracias por ser un angel en mi vida.

Contents

Abstract iv

List of Tables x

List of Figures xii

List of Abbreviations xvii

Acknowledgements xx

1.0 Introduction 1

1.1 Clinical Motivation 1

1.2 Current Breast Cancer Imaging Techniques 2

1.3 Computed Tomography (CT) 5

1.4 Tomosynthesis 7

1.5 MMIL Dedicated Breast CT system 8

1.6 Scatter in CT Imaging 10

1.7 Image quality Metrics 13

1.8 Specific Aims 15

2.0 Materials and Methods 17

2.1 Experimental setup 17

2.2 Data Collection with Dedicated Breast CT System 19

2.3 CT Scatter Correction 21

2.3.1 CT Scatter Correction Introduction 21

2.3.2 BSA specifications 22

2.3.3 Scatter correction algorithm 23
2.4 Acquisition and Scatter Correction 24
2.5 Reconstruction and Analysis 25
2.6 Non-uniformity and Line Profile Analysis 25
2.7 SNR and Contrast analysis 26
2.8 Detectability Observer Study 27
2.8.1 Detectability Observer Study Setup 29
2.8.2 Statistical Analysis of Detectability Observer Study 30
2.9 2-AFC Background 34
2.9.1 2-AFC Background 34
2.9.2 2-AFC Setup 38
2.9.3 Statistical Analysis of 2-AFC Observer Study 45
3. Results 46
3.1 Line profiles 46
3.2 Non-uniformity 49
3.3 SNR and Contrast Analysis 50
3.4 Detectability Observer Study 62
3.5 2-AFC Observer Study 71
3.6 Statistical Analysis of 2-AFC Observer Study 76
3.6.1 Effects of factors on Signal Detection 76
4. Discussion, Conclusions, and Future Directions 79
4.1 Line profiles 79

4.2 Non-uniformity 80
4.3 SNR 81
4.4 Contrast 81
4.5 Detectability Study 82
4.6 2-AFC study 83
4.6.1 Probability of Detection and Detectability Index 83
4.6.2 Statistical Analysis of 2-AFC 84
4.7 Conclusion 86
4.8 Recommendations 88
4.9 Future Directions 92
Appendix 93
References 97
Biography 100

List of Tables

Table 2-1: Concentration of methanol and water used to simulate different breast densities…….19

Table 2-2: Detectability index, d', values corresponding to the proportion of correct responses; P. M value indicates number of alternatives. This table shows that the same detectability index is used for ROC and 2-AFC experiments. This table has been adopted from [26]……....35

Table 3-1: Summary of paired two tail student t-test for uniform vs. yarn background detectability for inner radius spheres with no scatter correction……..……...…64

Table 3-2: Summary of paired two-tail student t-test for uniform vs. yarn background detectability for inner radius spheres under scatter correction……...…….65

Table 3-3: Summary of paired two-tail student t-test for uniform vs. yarn background detectability for outer radius spheres without scatter correction…….....…66

Table 3-4: Summary of paired two-tail student t-test for uniform vs. yarn background detectability for outer radius spheres under scatter correction……...…....67

Table 3-5: Summary of paired two-tail student t-test for detectability of smallest sphere in inner vs. outer radius in uniform background without scatter correction……..…68

Table 3-6: Summary of paired two-tail student t-test for detectability of smallest sphere in inner vs. outer radius in uniform background under scatter correction…….69

Table 3-7: Summary of paired two-tail student t-test for detectability of smallest sphere under scatter and non scatter corrected conditions in uniform background for inner radius
spheres……...70

Table 3-8: Summary of multiple comparisons using paired two-tail student t-test to measure statistically significant difference in detectability between various phantom configuration pairs. …….71

Table 3-9 Table indicating total number of scatter and non-scatter corrected cases, independent of size, location, concentration, and reader. The resultant Chi square, χ^2, p-

value indicates marginal significance between scatter and non-scatter corrected detection of
signals……76

Table 3-10 Table indicating total number of cases detected for 50%Methanol 50% water, and 100% water concentration, independent of size, location, scatter correction, and reader. The resultant Chi square, χ^2, p-value indicates highly significance difference between scatter and non-scatter corrected detection of signals……76

Table 3-11 Table indicating total number of cases detected for each sphere size, independent of concentration, location, scatter correction, and reader. The resultant Chi square, χ^2, p-value indicates highly significance difference between the detection of different sphere
sizes……76

Table 3-12 Table indicating total number of inner and outer radius cases detected, independent of size, scatter correction, concentration, and reader. The resultant Chi square, χ^2, p-value indicates highly significant difference between signal detection in inner and outer
radius……
……..76

Table 3-13 Table indicating the performance of each observer for 240 signals presented. A 0 means signal was not detected and 1 means signal was detected. The resultant Chi square, χ^2, p-value indicates no significant difference in the inter-observer performance……..…78

Appendix Table 1 Analysis of deviance for logistic regression model (Appendix eq. 1)**…...…..**94

Appendix Table 2 Estimated coefficients, standard errors and p-values for equation 1 in appendix..……..95

Appendix Table 3 Estimated coefficients, standard errors and p-values for three factor interactions. **……..**96

List of Figures

Figure 1-1: Patient in an upright position with breast compressed between paddle and film plate ……..……...3

Figure 1-2: Mammogram of breast indicating breast cysts, micro calcifications and macro
calcifications…….4

Figure 1-3: Illustration of helical CT scanner showing that as the ring gantry rotates the bed simultaneously translates through the bore of scanner ……..…6

Figure 1-4: Schematic of acquisition for breast tomosynthesis system.……....7

Figure 1-5: Photograph of the Duke University Medical Center prototype breast tomosynthesis system ……...…….……...8

Figure 1-6: Photograph of current MMIL dedicated Breast CT system with X-ray tube and flat panel detector mounted on a circular gantry which allows for 360 degrees of azimuthal rotation. Breast incident energy spectrum of the unconventional, ultra thick K-edge Ce-filtered beam at 60kVp ……..10

Figure 1-7: Schematic illustration of side view and top view of cone beam of MMIL dedicated breast CT system indicating the fan angle $\emptyset_{\text{fan}}$and the cone angle $\emptyset_{\text{cone}}$…….10

Figure 1-8: Effects of x-ray scatter on CBCT contrast and CN…….....13

Figure 2-1: Photo of the lesion phantom used in this study containing acrylic spheres at two radial distances. Spheres ranged in size from 1-8 mm. Photo of yarn used in the breast phantom to simulate structural noise with characteristics identical to the spheres is also presented……...17

Figure 2-2: Data matrix: Measurements for each condition were repeated 5 times: (1) breast phantom was without and with spheres; (2) with each previous condition, phantom was with and without yarn as structural background; (3) all conditions additionally had the background fluid density changed for 3 methanol-water concentrations; (4) all conditions had measured scatter correction, and data was reconstructed with and without scatter correction. These measurements yielded 120 data

sets……..17

Figure 2-3: Photo of the anthropomorphic breast phantom containing acrylic yarn hanging in the MMIL system……...……..18

Figure 2-4: Photo of CT sub-system. Primary features include a cone beam tungsten target x-ray source, and a Paxscan 2520 digital flat panel detector. SID is 60cm and SOD is 38 cm……..20

Figure 2-5: 2D SPR profile through the center of Anthropomorphic breast phantom ….21

Figure 2-6: Photograph of beam stop array (BSA) developed by Dr. Priti Madhav used for scatter correction. The BSA is a 9.5x9.5x2mm acrylic plate that consists of 108 2mm diameter lead balls spaced 5mm apart in 2-dimensions on a Cartesian grid…….22

Figure 2-7: Projection image of a water-filled breast phantom at the center of FOV superimposed with a segment of the beam stop array…….....24

Figure 2-8: Representation of ROI selection. Black circle represents boundary of signal, green circle is the signal ROI, and red circles represent the background ROIs. Signal ROI was chosen such that it was large as possible but within the signal boundaries. Four background ROIs of the same area as the signal ROI were selected non-uniformly around the signal ROI and allowed for 4 SNR and contrast calculations per signal…....26

Figure 2-9: Matrix of reconstructed CT Acquisitions of the breast phantom for 3 background concentrations x 2 background noise conditions x 2 reconstruction conditions with and without scatter correction. Additional measurements included same conditions but without beads present. By combining the shown images with those others mentioned, and all their repetitions 5 times, there were a total of 60 scans. Image pairs are displayed in the same global maximum……....28

Figure 2-10: Screen Capture of Observer Study setup. Observers were given a stack of TIFF images and were allowed to scroll through the stack to determine number of visible spheres in the inner and outer radius……...30

Figure 2-11: Instructions given to observers with illustration indicating the approximate location of the spheres, and how to input data into the survey sheet…….....31

Figure 2-12: Spreadsheet given to observers so that they could record the sphere sizes they saw on both the inner and outer rings of the lesion phantom……..…32

Figure 2-13: d' vs. SNR for 5 AFC study's, M indicates number of alternatives in each stud….....35

Figure 2-14: Power analysis for worst-case scenario (1.25 % difference in detectability between scatter corrected and non scatter corrected images)……...38

Figure 2-15: Power analysis for best-case scenario (6.25 % difference in detectability between scatter corrected and non-scatter corrected images)…….…..39

Figure 2-16: Screen capture of 2-AFC experimental setup, with illustration of GUI containing two panels, one of which contains the signal. Observer types "a" to indicate signal is on the left and "d" to indicate signal is on the right……..…..41

Figure 2-17: Data matrix: 6 sphere sizes (1-6 mm) from both inner and outer radius in breast phantom with 2 different concentrations were acquired 5x under 4 conditions: (1) in Uniform background (2) In yarn background (3) with and (4) without scatter correction……...42

Figure 2-18: Drawing of 2-AFC GUI with left and right panel. ……...43

Figure 3-1: L Matrix of Coronal slices of breast phantom containing 100% Methanol in uniform and yarn background under scatter and non-scatter corrected conditions. Arrows and dashed white line indicate where line profile was taken.……...….46

Figure 3-2: Line profiles in 100% Methanol density in (LEFT) uniform and (RIGHT) yarn background……...……..……..47

Figure 3-3: Matrix of Coronal slices of breast phantom containing 50% Meth. 50% Water in uniform and yarn background under scatter and non-scatter corrected conditions. Arrows and dashed white line indicate where line profile was taken……..…47

Figure 3-4: Line profiles in 50% water 50% Methanol density in (LEFT) uniform and (RIGHT) yarn background……..48

Figure 3-5: Matrix of Coronal slices of breast phantom containing 100% Water in uniform and yarn background under scatter and non-scatter corrected conditions. Arrows and dashed white line indicate where line profile was taken…….48

Figure 3-6: Line profiles in 100% water density in (LEFT) uniform and (RIGHT) yarn background……...…49

Figure 3-7: Coronal slice through (LEFT) scatter corrected and (RIGHT) non scatter corrected breast phantom containing 100% Methanol. Green ROI (radius of 100 pixels) represents central region used in non-uniformity calculation. 5 red (radius- 44.72 pixels) ROIs are the edge ROIs……...49

Figure 3-8: Plot of non-uniformity as a function of background fluid density in the breast phantom for scatter and non-scatter corrected images……...50

Figure 3-9: Signal and background ROI selection for spheres in 100% Methanol for SNR and contrast calculation…….……..…51

Figure 3-10: SNR plots for inner and outer radius spheres in 100% Methanol…….....52

Figure 3-11: Contrast plots for inner and outer radius spheres in 100% Methanol……..53

Figure 3-12: Signal and background ROI selection for spheres in 50% Methanol 50% Water for SNR and contrast calculations …….54

Figure 3-13: SNR plots for inner and outer radius spheres in 50% Methanol 50% water……..……....55

Figure 3-14: Contrast plots for inner and outer radius spheres in 50% Methanol 50% water…….…56

Figure 3-15: Signal and background ROI selection for spheres in 100% Water. for SNR and contrast calculations……...…..57

Figure 3-16: SNR plots for inner and outer radius spheres in 100% water……...….58

Figure 3-17: Contrast plots for inner and outer radius spheres in 100% water……...…..59

Figure 3-18: Comparison of contrast in inner and outer radius for scatter corrected images in 100% water and 50% water 50% methanol concentrations…….……60

Figure 3-19: Comparison of contrast in inner and outer radius for scatter corrected images in 100% Methanol…….…..…..61

Figure 3-20: Summary of Observer detectability study for smallest sphere detected in each phantom configuration……..62

Figure 3-21: Comparison of smallest sphere detected in uniform vs. yarn background for three concentrations. For comparison, both cases were not scatter corrected and the inner radius location was used. Error bars represent standard error over 5 observers…63

Figure 3-22: Comparison of smallest sphere detected in uniform vs. yarn background for three concentrations. For comparison, both cases were scatter corrected and the inner radius location was used. Error bars represent standard error over 5 observers……..65

Figure 3-23: Comparison of smallest sphere detected in uniform vs. yarn background for three concentrations. For comparison, both cases were not scatter corrected and the outer radius location was used. Error bars represent standard error over 5 observers....66

Figure 3-24: Comparison of smallest sphere detected in uniform vs. yarn background for three concentrations. For comparison, both cases were scatter corrected and the outer radius location was used. Error bars represent standard error over 5 observers……...67

Figure 3-25: Comparison of smallest sphere detected in inner vs. outer radius for three concentrations. For comparison, both cases were in uniform background and images were not scatter corrected. Error bars represent standard error over 5 observers…….68

Figure 3-26: Comparison of smallest sphere detected in inner vs. outer radius for three concentrations. For comparison, both cases were in uniform background and images were scatter corrected. Error bars represent standard error over 5 observers……...69

Figure 3-27: Comparison of smallest sphere detected under scatter and non scatter corrected conditions for three concentrations. For comparison, both cases were in uniform background and inner radius location was used. Error bars represent standard error over 5 observers…….……...…..70

Figure 3-28: Results of the 2-AFC study for the inner radius spheres in uniform 50% water 50% methanol in terms of probability of detection and detectability index, using transformation of probability values……..…..72

Figure 3-29: Results of the 2-AFC study for the outer radius spheres in uniform 50% water 50% methanol in terms of probability of detection and detectability index, using transformation of probability values……....73

Figure 3-30: Results of the 2-AFC study for the inner radius spheres in uniform 100% water in terms of probability of detection and detectability index, using transformation of probability values……...…….…..…..74

Figure 3-31: Results of the 2-AFC study for the outer radius spheres in uniform 100% water in terms of probability of detection and detectability index, using transformation of probability values……..……..75

Figure 4-1: SNR Plots for inner radius spheres in 50% water 50% methanol, annotated to indicate at what sphere sizes 90% P and JND values start. ……. ……...….90

Figure 4-2: SNR Plots for inner and outer radius spheres in 100% water, annotated to indicate at what sphere sizes 90% P and JND values start. …….……91

List of Abbreviations

2-AFC	Two Alternative Forced Choice
AIC	Akaike's information criterion
BKE	Background known exactly
BSA	Beam stop array
CT	Computed tomography
CBCT	Cone beam computed tomography
d'	Detectability index
df	Degrees of freedom
FBP	Filtered back projection
FOV	Field of View
FDA	Food and Drug Administration
GUI	Graphical user interface
JND	Just noticeable difference
keV	Kilo-electron volts
MMIL	Multi Modality Imaging Lab
MRI	Magnetic resonance imaging
MRMC	Multi-read-multi case
OSC	Ordered subset convex

P	Probability of detection
ROC	Receiver Operating Characteristics
SPR	Scatter to primary ratio
SKE	Signal known exactly
SNR	Signal-to-Noise ratio
US	Ultrasound

Acknowledgements

First and foremost, I would like to thank Dr. Tornai for the opportunity to complete this work in his lab. He provided valuable guidance and advice in completing this work.

I also owe great thanks to my committee, Dr. Dobbins and Dr. Lo both for their comments and guidance on this work.

I also extend a special thanks to Dr. Kingshuck Choudhury for all his work and help on the statistical analysis of the 2-AFC study.

Extensive use of the CPU-based OSC reconstruction algorithm was kindly provided by Dr. Randy McKinley of ZumaTek, Inc. Dr. Olga Baranova, Kathy Barbour, and Katherine Hand went to great lengths to help me administratively and were always very kind and available to answer any administrative questions I had. Dr. Turkington for his help in registering for the classes I needed to complete my degree. Steven Earp at the Pratt student machine shop was always very helpful in helping me machine parts for my research. Olav Christiansen for his help in the set-up and calibration of the equipment for the 2-AFC study. I would also like to thank all the participants in the 2-AFC and detectability study.

Last but not least, I owe great thanks to my friend and moral counselor, Jordan Rifis, for his administrative help and moral support.

This work has been funded by the National Institutes of Health grant R01-CA096821, and my stipend and graduate funding has come from and T32-EB001040

1. Introduction

In this chapter we begin with the clinical motivation for the research. We will then describe current breast cancer imaging techniques and modalities and also note their drawbacks. We then provide a description of the Multi Modality Imaging Lab (MMIL) dedicated breast CT system, and how this research machine provides patient comfort and meets the clinical needs of breast cancer diagnosis. We will then present the physical principals behind scatter in CT imaging and the effects of scatter on image quality. Thereafter we present image quality metrics used in this work to characterize the image quality of both scatter and non-scatter corrected images. Finally, we will present the purpose and aims of this research work.

1.1 Clinical Motivation

For women in the U.S, breast cancer ranks as the most common cancer. Based on the National Cancer Institute's (NCI) Surveillance, Epidemiology, and End Results (SEER), 1 in 8 women or 12.2 percent of women born in the United States today will be diagnosed with breast cancer at some time in their lives. This estimate is based on breast cancer statistics for the years 2005 through 2007 [1]. Additionally, the SEER report states that the mortality rate of breast cancer is 24.0 per 100,000 women in the U.S between 2003 and 2007 [2]. The prevalence of breast cancer in the U.S makes it critical to screen for breast cancer and identify the disease at an early stage. It's important that breast cancer gets detected at an early stage since it is a progressive disease and smaller tumors

have a better prognosis and are more successfully treated. By screening for breast cancer, tumors can be detected before they become palpable, and thus morbidity and mortality is reduced.

Furthermore, density of a breast plays a big role in the detection of breast cancers. This is mainly because each type of breast tissue reacts differently to x-rays. Fatty breast tissue (low density tissue) is relatively transparent to x-rays, and allows x-rays to pass through resulting in dark areas in the image. On the other hand, dense tissue, epithelial and stromal tissues, absorbs more x-rays therefore getting a higher relative dose to fatty tissue, and thus block x-rays and appear as white areas on the image. In denser breast, breast lesions are not easily discernable since there is reduced contrast between the dense tissue and the breast lesions [3]. Furthermore, since glandular and stromal tissue cells are more proliferative compared to fatty breast cells, they are more likely to react badly to (any) increased radiation.

1.2 Current Breast Cancer Imaging Techniques

Several breast cancer diagnostic test are commonly employed to determine breast malignancies. Currently, the most routinely and widely used screening technique for breast cancer is X-ray mammography. X-ray mammography provides 2-D images of the compressed breast. When getting a mammogram, the patient is in an upright position and has her breast compressed by two plates (Figure 1-1).

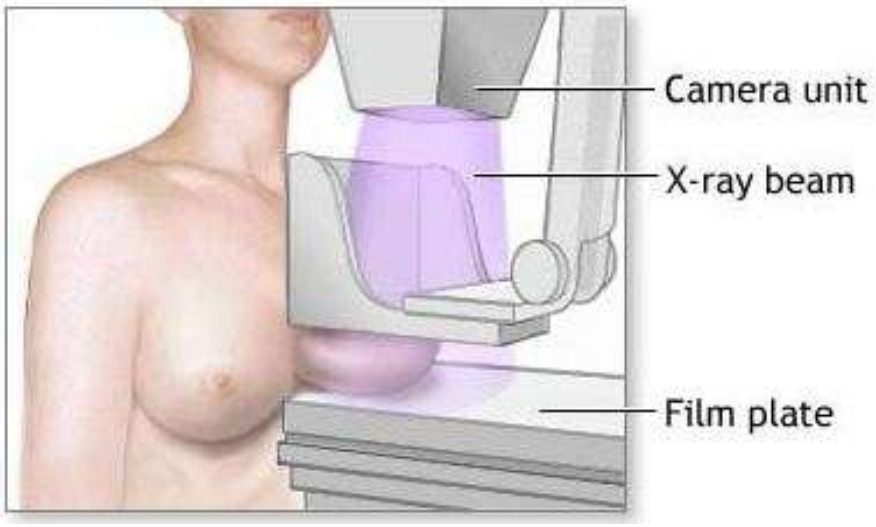

Figure 1-1: Patient in an upright position with breast compressed between paddle and film plate (figure obtained from [4]). Note that In more contemporary systems, the film plate is replaced by a digital x-ray receptor that performs the exact same function.

By compressing the breast, more of the breast is imaged, the thickness decreases and thus path length of the x-rays decreases, scatter gets reduced, and less blurring and motion artifacts arise since the breast is immobilized[5,6]. Once the breast is compressed and positioned, x-rays are transmitted through the breast with energies between 15-30 keV [6]. FDA regulations require that the mean glandular dose delivered during a single cranio-caudal view of an FDA-accepted phantom must not exceed 3 mGy (0.3 rad) per exposure [7]. The x-rays that make it through the breast interact with the detector to produce an image that is viewed and analyzed by a radiologist. Radiologists typically look for breast masses, breast cysts and calcifications. Breast cysts are tiny accumulations of fluid and are the most common cause of benign (non-cancerous) breast

lumps in women between age 30 and 50 [8]. Calcifications are calcium deposits in the breast that may be either benign or malignant. Usually the calcifications that are larger and have smoother boundaries (macro calcifications) are benign [9] (Figure 1-2).

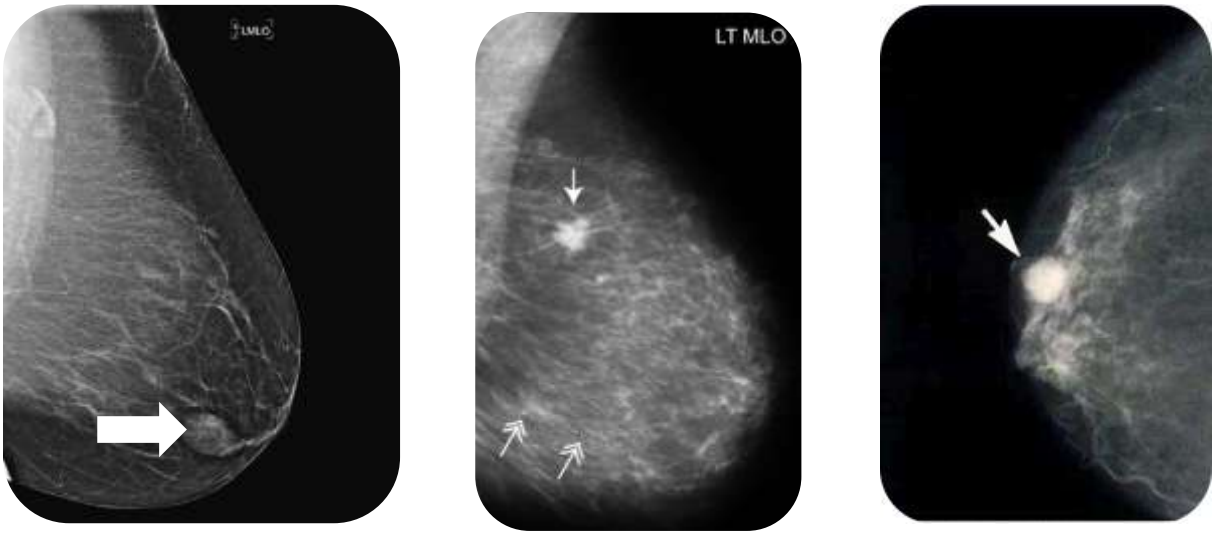

Figure 1-2: (LEFT) Mammogram of breast with white arrow indicating breast cysts (figure obtained from [10]). (CENTER) Mammogram of breast with double headed arrows indicating micro calcifications. (RIGHT) Mammogram indicating macro calcifications (figures obtained from [11]). These larger calcifications with smooth boundaries are usually benign.

While X-ray mammography is the most routinely used screening tool for breast cancer it has many shortcomings. The basic limitation of x-ray mammography is that it does not catch all cancers, simply because it is hard to distinguish between glandular tissue and tumors [11]. Another common problem x-ray mammography encounters is that inaccurate diagnoses arise when the patient has silicone implants. The inaccurate diagnosis is due to three factors. First, the visibility of small low-contrast objects gets

masked by the superposition of silicon and underlying tissue. Secondly, the density differences produced by a silicone implant result in a low radiographic density due to the radiopaque characteristics of these implants [12]. Lastly, the silicone prosthesis affects the compression of the breast, which as described earlier, decreases the pathlength that the x-rays traverse. In addition to these limitations, clinical studies have shown that mammography has a false negative rate ranging between 20-40%, and increases more when the patient has a dense breast [13]. The high rate of false negatives is particularly problematic with younger women who tend to have dense breast.

1.3 Computed Tomography (CT)

CT is an imaging modality that uses x-ray projection images at discrete angles around an object to produce 3-D reconstructed slices of the object. Reconstructions are highly computational and can either be iterative or filtered back projected (FBP) reconstructions. Unlike in projection radiography, the x-rays in CT traveling through the object to form projection images are collimated so that they travel within a 2-D fan beam [14]. Within each reconstructed image slice, each pixel value represents attenuation coefficients of the object being imaged.

There are different kinds of CT scanning operating modes. There's the standard single slice CT, helical CT, and multi-slice CT. In helical CT, a patient is continuously translated through the bore of the CT system in which the x-ray tube and detectors continuously rotate (Figure 1-3). Helical CT allows for rapid 3-D data acquisition of the

entire body in less than a minute [14]. In a multi-slice CT scanner, 3-D imaging of a patient is possible due to several rows of detectors that gather a cone of x-ray data.

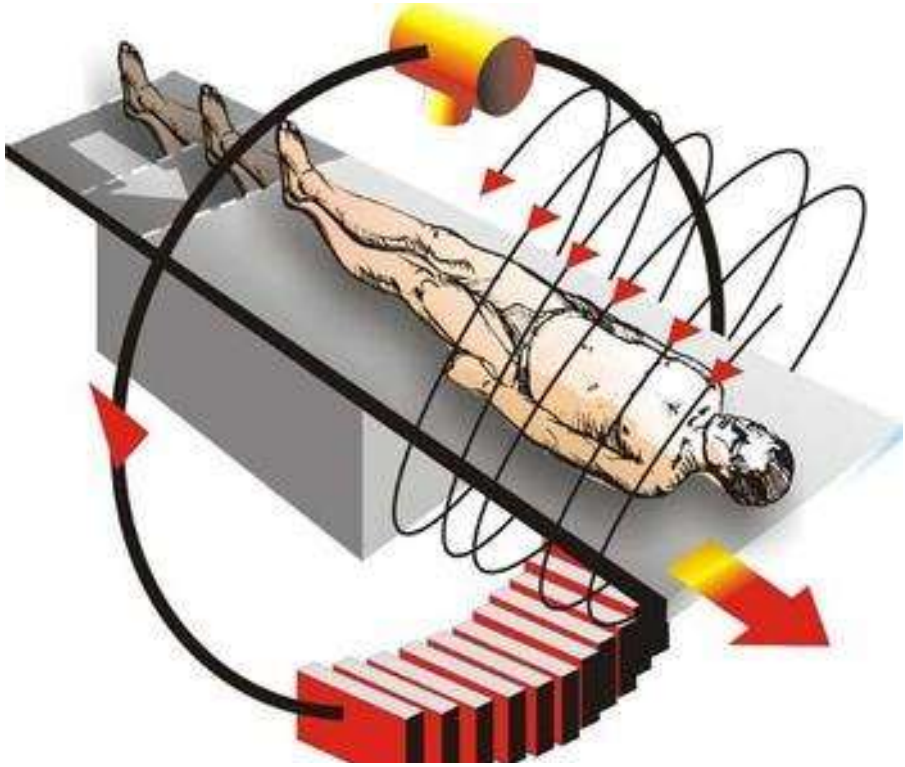

Figure 1-3: Illustration of helical CT scanner showing that as the ring gantry rotates the bed simultaneously translates through the bore of scanner (figure obtained from [15]).

The main advantage of CT imaging is that the images are volumetric representations of anatomical structures within a patient and have increase contrast-resolution characteristics due to the ability to remove overlapping tissues. Unlike the 2D images that result from planar radiography and mammography, anatomical structures are not collapsed in CT images. The 3-D information provided from CT imaging increases the sensitivity and specificity of cancerous nodules/lesion that would otherwise be hidden in the overlapping anatomy as is the case in planar imaging.

While CT imaging eliminates the problem of overlapping anatomy and provides nearly complete anatomical information of the patient, it has several disadvantages. One drawback to CT is that the radiation dose that a patient receives in a CT scan is much higher than planar radiography. State-of-the-art CT scanners are also limited in the sensitivity and specificity required to detect breast cancer. Finally the cost of whole body CT scanners and required maintenance poses a great barrier in using this modality to routinely screen for breast cancer.

1.4 Tomosynthesis

Like CT, digital tomosynthesis partly mitigates the problem of overlapping structures, and aims to provide non-overlapped in-plane slices of the object imaged. However, unlike CT imaging that requires many projections acquired over an angular range of 180-360°, tomosynthesis requires 11-60 projections over an angular span of only 30-60°.

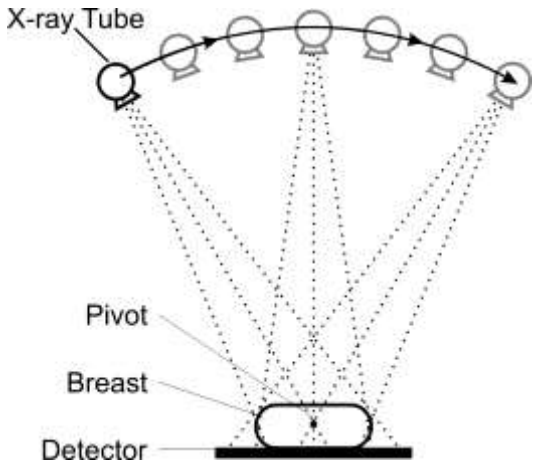

Figure 1-4: Schematic of acquisition for breast tomosynthesis system (figure obtained from [16]).

Additional requirements of tomosynthesis are that the object stays stationary and compressed. Thick tomographic slices are achieved in tomosynthesis by reconstructing the data by shifting the projections relative to one another [17].

The main advantage of tomosyntheisis is that the resolution of tomosynthesis slices are comparable to standard projection images in planes parallel to the image receptor [18]. Tomosynthesis also has the added benefit of lower cost and radiation exposure compared to CT, but higher dose and far higher cost than x-ray mammography.

The main shortcoming of tomosyntheis is that it requires compression of the breast.

Figure 1-5: Photograph of the Duke University Medical Center prototype breast tomosynthesis system (figure obtained from [19]).

1.5 MMIL Dedicated Breast CT system

The Multi-Modality imaging lab at Duke University has built and investigated a dual-modality single photon emission computed tomography (SPECT) and dedicated breast cone beam CT (CBCT) system. The aim of this system is to provide high quality diagnostic information without compressing the breast.

Currently, the dedicated CT system consists of a cone beam x-ray source and flat panel detector by *Varian* mounted on a circular gantry, which allows for 360 degrees of azimuthal rotation. The X-ray tube has a custom built collimator. A cerium (Z=58, $\rho = 6.77 \frac{g}{cm^3}, K-edge = 40. keV$) 100th value attenuating filter (0.0508 cm, evaluated at 60kVp) is inserted behind the collimator but down-stream from the source to yield a mean x-ray beam of approximately 36keV and a FWHM of 15% [20] (Figure 1-6). The geometry of the CBCT system is shown in figure 1-7 indicating the fan angle $\emptyset_{fan}$and the cone angle $\emptyset_{cone}$.

The advantages of the quasi-monochromatic source is that it lowers the x-ray dose, minimizes beam hardening effects, and improves image quality of small lesions that would not otherwise be seen due to close attenuation values with surrounding tissues [20]. Studies performed by a colleague, Dr. Dominic Crotty, show that the dose from the MMIL dedicated breast CT system (4.5 mGy) is comparable to that of dual-view mammography [20]. To acquire the CT data, the gantry with the x-ray tube and

detector rotate around the pendant uncompressed breast in a circular orbit. Projections can be acquired at a range of different angles around the breast, however 240 projections (a projection every 1.5 degree) or 360 projections (1 projection per degree) are usually acquired. The data is then reconstructed with an ordered subset convex (OSC) algorithm [21].

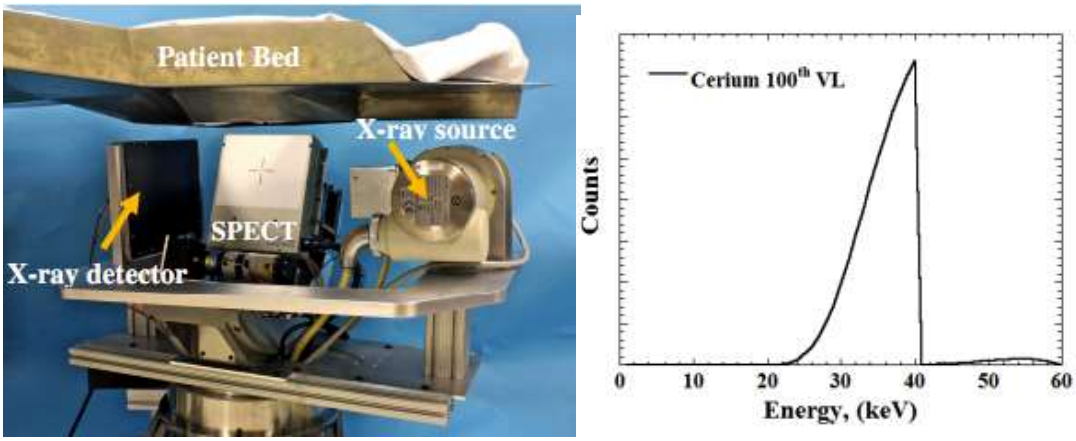

Figure 1-6: (LEFT)Photograph of current MMIL dedicated Breast SPECT-CT system with X-ray tube and flat panel detector mounted on a circular gantry which allows for 360 degrees of azimuthal rotation. (RIGHT) Breast incident energy spectrum of the unconventional, ultra thick K-edge Ce-filtered beam at 60kVp (figures adopted from [20]).

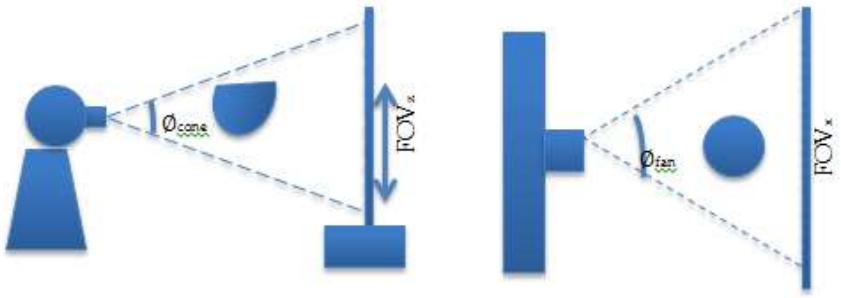

Figure 1-7: Schematic illustration of (LEFT) side view and (RIGHT) top view of cone beam of MMIL dedicated breast CT system indicating the fan angle $\emptyset_{fan}$and the cone angle $\emptyset_{cone}$.

1.6 Scatter in CT Imaging

In the CT imaging energy range, as well as projection radiography, there are three primary electromagnetic radiation interactions that can occur. Photons can interact with matter through (1) photoelectric effect, (2) Compton scatter, and (3) coherent scatter. The photoelectric effect is the primary mechanism that provides contrast between different tissue types, whereas Compton and coherent scatter are the main mechanism for limiting the resolution of the CT images [14]. Since the MMIL dedicated breast CT system has a mean x-ray beam of approximately 36keV,we will focus on Compton interactions since these are more prevalent (>60%) at energy's above 30keV [14]. We also mention coherent scatter for completeness since at energies <50keV, coherent scatter plays a consequential role but is indistinguishable from Compton scattering. Nonetheless, coherent scatter is indistinguishable from Compton scatter since the detectors used do not (currently) have energy discrimination; thus "scatter" is considered both from Compton and coherent components.

In Compton interactions, a photon interacts with the outer shell electrons of an atom, but instead of getting completely absorbed, the photon transfers some of its energy to an electron and changes its direction. The incident photon carries an energy of $E = \hbar\nu$, where ħ is Planck's constant and ν is the frequency of the photon. When it interacts with the electron, it loses energy and changes its direction. This resultant scattered photon is called the Compton photon and has an energy of:

$$\hbar\nu' = \frac{\hbar\nu}{1+{}^{\hbar\nu}/_{m_0c^2\,(1-cos\theta)}} \quad (1.1)$$

Where $m_0c^2 = 511$ keV is the rest energy of the electron, and θ is the angle through which the photon is scattered. As can be seen from this equation, the resultant energy of the Compton photon depends on the angle that it's scattered. The bigger θ, the more energy the incident photon looses.

In diagnostic imaging, we would like to minimize Compton scattering since it causes photons to take a nonlinear path through the object. Minimizing Compton scattering means minimizing the likelihood of a Compton interaction, which depends on the electron density of the object since Compton photons arise when the incident photon interacts with loosely bound electrons of the outer shell. The electron density of a material is given by:

$$ED = \frac{N_A Z}{W_m} \quad (1.2)$$

Where N_A is Avogadro's number, Z is the atomic number, and W_m is the molecular weight of the atom (grams/mole). The probability of Compton scattering can be said to be independent of Z since the ratio of Z/W_m is the same for all elements other than hydrogen [14]. In practical terms, equation 1.2 says that the amount of scatter increases as the object size increases, independent of object composition.

There are several ways that Compton photons are unfavorable to image quality. As can be seen from equation 1.1, the more the photon deflects the less energy it retains. Theses lower energy photons can, if they are headed toward the detector, get detected

and impact the final image with reduced contrast. Scattered photons also create a cupping artifact in the final CT image since they introduce a redistribution (apparent increase) of photons on portions of the detector. The effect of reduced contrast and cupping artifacts is detrimental to structure visualization as well as the accuracy of attenuation values that can be used for quantification [22]. It is for these reasons that methods have been developed to measure and correct for scatter in projection radiography and CT.

The amount of scatter in an image can be measured as the scatter to primary ratio (SPR). To measure SPR, projections are acquired with and without lead blockers. The ensemble of pixel values in the shadow of the blocker give the scatter only signal, and the values without the blocker give the "scatter and primary" signal [23]. SPR is then calculated by dividing the

"scatter only" signal by the difference between the "scatter only" and the "scatter +primary" signal. Figure 1-8 show the degradation of contrast and CNR as the SPR increases.

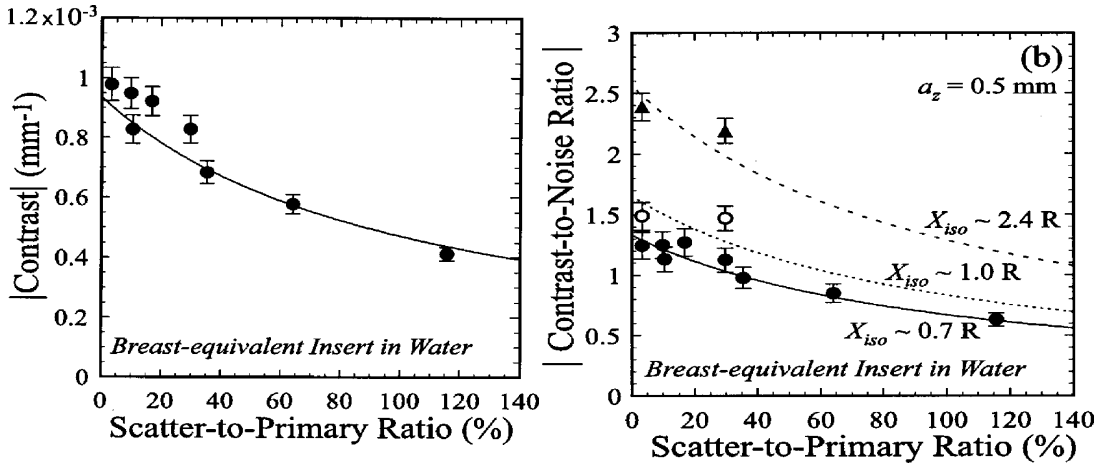

Figure 1-8: Effects of x-ray scatter on CBCT (LEFT) contrast and (RIGHT) CNR (figures obtained from [23]).

1.7 Image quality Metrics

There are a variety of ways to quantitatively evaluate an imaging system. Signal-to-noise-ratio (SNR) and contrast are most commonly used to quantitatively describe the detectability of structures in the final image. Observer studies are also commonly used to evaluate the degree to which objects can be detected.

Contrast is a metric that is used to measure how well an object stands out from the surrounding background. Mathematically it is defined as:

$$Contrast = \frac{S_{background} - S_{lesion}}{S_{background}} \qquad (1.3)$$

where $S_{background}$ is the background mean signal and S_{lesion} is the mean signal of your lesion or object of interest. As can be seen from equation 1.3, when S_{lesion} is close to $S_{backgroud}$ the contrast is very low, making the lesion hard, if not impossible, to detect.

Differential SNR (also called CNR in Fig. 1-8), like contrast, measures the difference between the mean pixel values of lesion and noise of the background. It is defined as:

$$SNR = \frac{S_{background} - S_{lesion}}{\sigma_{background}} \quad (1.4)$$

Here $\sigma_{background}$ is the standard deviation or noise of the background. Having a large SNR improves detectability, but the question remains as to what minimal SNR and contrast values are needed to distinguish an object from the background. The answer lies in the Rose criterion, which states that SNR has to be equal to or greater than 5 in order for an observer to accurately distinguish a lesion or object from the background noise [24].

Line profiles are also routinely used to measure the uniformity of the image. A uniform image will have a flat line profile, whereas an image with a cupping artifact will result in a line profile that dips in the center.

Non-uniformity can be further quantified by calculating the cupping index [23]:

$$t_{cup} = 100 * \frac{\langle \mu_{edge} - \mu_{center} \rangle}{\mu_{edge}} \quad (1.5)$$

1.8 Specific Aims

The goal of this work is to evaluate the image quality of both scatter and non-scatter corrected breast CT images, and to determine if scatter correction improves signal detectability for signals in different simulated breast densities, and at two radial positions. The hypothesis of this study is that scatter correction will increase the noise of

the images due to the propagation of error that results from applying the correction. An increase in noise will most likely reduce SNR, however I believe the resultant degradation of SNR will be minimal due to a relatively low increase in pixel-to-pixel variations. Additionally, scatter correction will boost attenuation values, especially in the center of the phantom (reflecting a reduction in the degree of cupping), which will increase contrast of the spheres at both radial locations. I believe that contrast will be slightly higher in the outer radius since other artifacts such as beam hardening will prevent scatter corrected images to have a completely flat profile (0 degree of cupping). Furthermore, I believe that the increase of contrast that results from scatter correction will lead to improved observer performance for all simulated breast densities tested, and will be most effective for smaller lesions in concentrations of higher density that already suffer from small difference in signal compared to background. Based on these hypotheses, this research aims to (a) show the advantages of scatter correction in breast CT through SNR, contrast, non-uniformity calculations, and line profiles for three simulated breast densities at 2 radial locations, (b) use detectability and 2-AFC observer studies to show the effect of scatter correction in signal detection, and finally (c) show the statistical significance of scatter correction in combination with radial location, size and concentration on detection response.

2.0 Materials and Methods

2.1 Experimental setup

Experiments were conducted using an anthropomorphic breast phantom (Radiology Support Devices, Newport Beach, CA) containing a lesion phantom specifically designed for this experiment (Figure 2-1). The lesion phantom consists of a thin (<0.5mm) plastic sheet supported by a thin acrylic annulus. Various acrylic spheres (Engineering Labs, Inc., Oakland, NJ) (density of 1.15g/cm^3) were cemented at two radial distances (2.5 and 5 cm). The uniform spheres varied in size from 1.0-8.0 mm diameter. An approximate volume of 500 mL of loosely packed 100% acrylic yarn was used to mimic structural noise in the background by simulating connective tissue of a breast and having identical density and attenuation coefficients as the acrylic spheres used in the study (Fig 2-1).

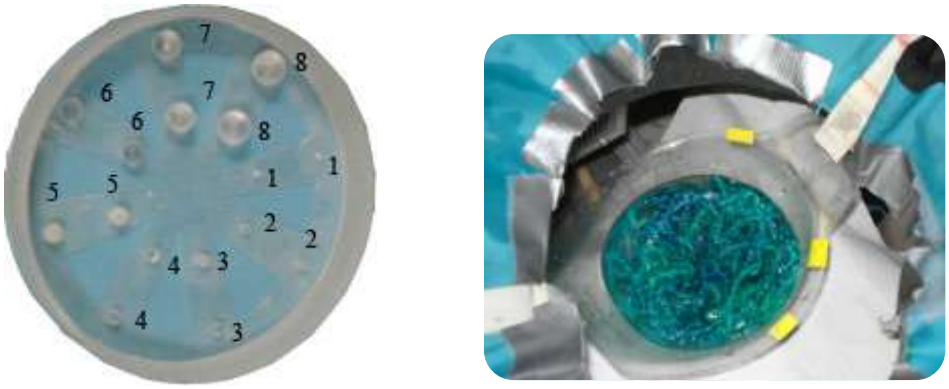

Figure 2-1: Photo of the lesion phantom used in this study containing acrylic spheres at two radial distances. Spheres ranged in size (mm) as indicated. (RIGHT) Photo of yarn used in the breast phantom to simulate structural noise with characteristics identical to the spheres.

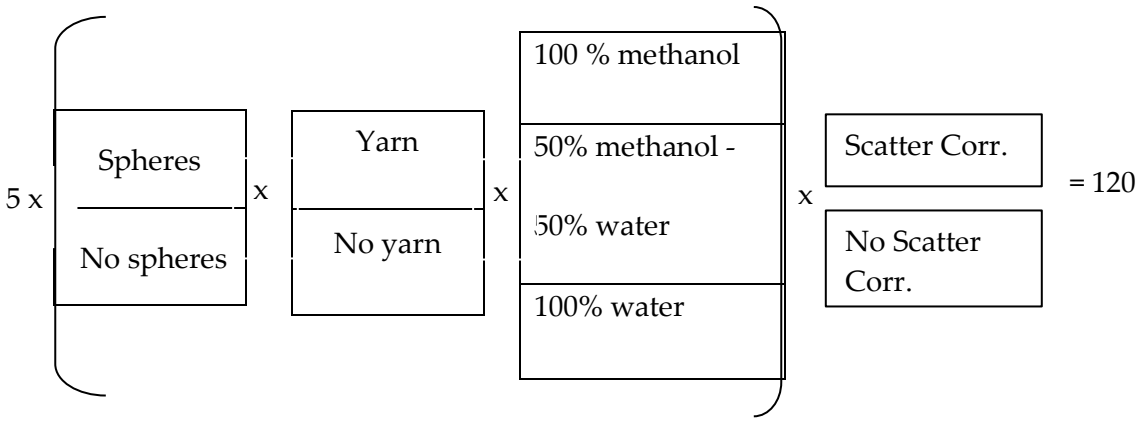

Figure 2-2: Data matrix: Measurements for each condition were repeated 5 times: (1) breast phantom was without and with spheres; (2) with each previous condition, phantom was with and without yarn as structural background; (3) all conditions additionally had the background fluid density changed for 3 methanol-water concentrations; (4) all conditions had measured scatter correction, and data was reconstructed with and without scatter correction. These measurements yielded 120 data sets.

Figure 2-3: Photo of the anthropomorphic breast phantom containing acrylic yarn hanging in the MMIL system.

To simulate the range of breast densities, and to have different levels of contrast, the breast phantom was filled in turn with 500mL of 3 different concentrations of methanol and water (Table 2-1). The complete data matrix of measurements is given in a progressive chart with the various variables indicated (Fig. 2-2). An example of the breast phantom with the simulated structural noise configuration is show in figure 2-3.

Table 2-1: Concentrations of methanol and water used to simulate different breast densities.

Composition/ Fluid	Density (g/cm^2)
100% methanol	0.791
50% methanol 50% water	0.896
100 % water	1.00

2.2 Data Collection with Dedicated Breast CT System

Acquisitions of the breast phantoms with the three different concentrations were performed 5 times under 4 conditions (Fig. 2-2): (1) with the lesions in uniform fluid (background) conditions, (2) with lesions and with acrylic yarn in addition to fluids, (3) without lesions under uniform background conditions, and (4) without lesions and with acrylic yarn and fluids. The images were then scatter corrected with the method described in section 2.3. This yielded 120 independent images that were reviewed by 5 Medical Physicists. One additional measurement was made for each concentration and structural background conditions but without any spheres.

The CT sub-system (Fig 2-4) is part of a dual-modality dedicated breast SPECT-CT scanner described in detail elsewhere [20,22]. Primary features include a cone beam tungsten target x-ray source (model Rad-94, *Varian Medical Systems*, Salt Lake City, UT) with a Paxscan 2520 (*Varian Medical Systems*, Salt Lake City, UT) digital flat panel detector having 127μm pixels; ultra-thick K-edge spectral beam forming filters produce a quasi-monochromatic beam [20]. At 60kVp tube potential, a 0.051cm cerium filter (Z = 58, ρ = 6.77 g/cm^3, K-edge = 40.4keV, *Santoku America, Inc.*, Tolleson, AZ) was used to produce a cone beam x-ray spectrum at a mean energy of 36keV and a FWHM of 15%. The source-to-image distance (SID) is 60 cm, and a 38 cm source-to-isocenter distance (SOD) results in a magnification of 1.57 for an object located at the system's center of rotation.

Figure 2-4: Photo of CT sub-system. Primary features include a cone beam tungsten target x-ray source, and a Paxscan 2520 digital flat panel detector. SID is 60cm and SOD is 38 cm.

2.3 CT Scatter Correction

As was described in section 1.5, Compton scattering in CT introduces cupping artifacts, reduces contrast, and leads to inaccurate reconstructed attenuation coefficients. Therefore it is crucial to the image quality of the system to manage the deleterious scatter effects.

2.3.1 CT Scatter Correction Introduction

Traditionally, the effects of scatter have been managed by selection of imaging geometry, the use of air gaps or scatter-rejection grids, selection of acquisition and reconstruction parameters consistent with a clinical task, or by the incorporation of scatter correction algorithms [14, 23]. For the MMIL dedicated breast CT system, a scatter correction algorithm is applied to improve contrast, image visualization, reduction of the cupping artifact, and accurate characterization of different tissues based on their absolute coefficients [22].

A previous study on SPR performed by an MMIL colleague, Jainil Shah, determined the SPR through the middle of an anthropomorphic breast phantom filled with fluids of densities ranging from 0.791-1.00 g/cm^2 (FIG. 2-5).

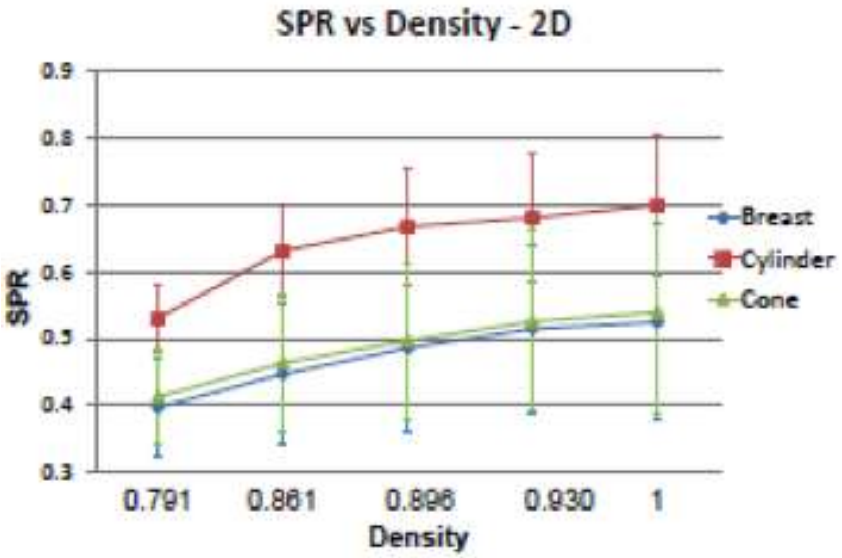

Figure 2-5: 2D SPR profile through the middle of the anthropomorphic breast phantom [23].

2.3.2 BSA specifications

Another MMIL lab member, Dr. Priti Madhav, has implemented a robust measured scatter correction algorithm that yields quantitative attenuation values within 5% of absolute narrow beam values [22, 25]. She performed scatter correction on CT projections by using a modified beam stop array (BSA) method that she developed. The BSA design consists of 180 holes (0.18 cm diameter and 0.1 cm depth) spaced 0.5 cm apart and drilled in a Cartesian grid arrangement on a 9.5x9.5x2 mm acrylic plate [22]. Lead spheres with 2.032 mm diameter are glued to fit over the holes (Figure 2-6). The BSA is attached to the front of the collimator at an approximate distance of 15 cm from the x-ray focal spot.

Figure 2-6: Photograph of beam stop array (BSA) developed by Dr. Priti Madhav used for scatter correction. The BSA is a 9.5x9.5x2mm acrylic plate that consists of 108 2mm diameter lead balls spaced 5mm apart in 2-dimensions on a Cartesian grid.

2.3.3 Scatter correction algorithm

To scatter correct the final CT images, a complete set of CT projections of the object get acquired with and without the BSA in front of the collimator (Figure 2-7). A projection is also taken with the BSA in place without an object in the field of view (FOV). The BSA in air gives the (x,y) positions of all the lead beads without an object. Additionally, a mask of the imaged object gets automatically generated by thresholding each projection with only the object in the FOV based on the k-means algorithm [22]. Next the projections taken with the BSA and object are used to measure the amount of scatter present. In this step, the average scatter value is measured over a 5x5 pixel ROI within each lead bead that is within the bounds of the object. Average scatter values get

extrapolated using a cubic spline calculation across each row containing the lead beads. This procedure gets repeated along each column with the lead beads. Thereafter, a 2D scatter profile over the entire projection image is obtained using a 2D cubic spline interpolation. Corrected projection images with minimal scatter are then obtained by subtracting the 2D scatter profile from the projections taken without the BSA at that azimuthal acquisition angle. The coding for this scatter correction algorithm was written in MATLAB (The Mathworks, Inc.,Natick, MA).

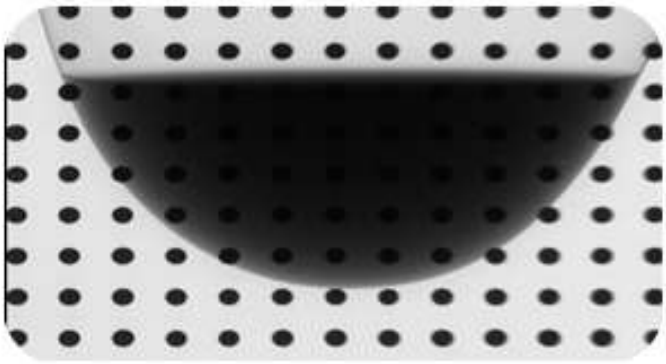

Figure 2-7: Projection image of a water-filled breast phantom at the center of FOV superimposed with a segment of the beam stop array.

2.4 Acquisition and Scatter Correction

For each phantom condition, 360 projections were collected azimuthally with and without a beam stop array (BSA). The BSA was statically mounted on the collimator, and scans were performed sequentially. The scatter correction algorithm (described in section 2.3.3) was used to determine the scatter distribution using the BSA [22]. In this algorithm, a 2D scatter distribution for each projection was estimated by cubic spline interpolating the measured average values located behind the shadow of

each beam stop inside the object. Previous studies have demonstrated that only 6 BSA projections are needed about the breast shaped object, but here all 360 degrees of BSA data was chosen to be acquired and calculated. The final scatter-corrected projections were calculated by subtracting the scatter images containing only a mask of the object from the original corresponding projections without the beam stops.

2.5 Reconstruction and Analysis

The data was reconstructed using a ray-driven ordered subset convex (OSC) algorithm which provided an estimate of the non-uniform attenuation distribution of the object. The OSC algorithm was provided by *Zumatek Inc* (Research Triangle Park, NC). Reconstruction parameters were set to 5 iterations, 16 subsets, 350x350x400 reconstruction grid, and 508μm^3 voxel size. Reconstructed images were all rotated so that the largest sphere was repositioned to approximately the 2 o'clock position. Rotation of the images was needed since the lesion phantom within the anthropomorphic breast phantom was rotated at each scan and at each distinct setup.

2.6 Non-uniformity and Line Profile Analysis

To quantify non-uniformity, and measure the degree of "cupping", pixel values near the center of the reconstructed slice were compared to the values at the edge of the phantom. The central ROI was chosen to have a radius of 100 pixels. 5 edge ROI were chosen to have a radius of 44.74 ($5 * \pi\sqrt{2000}^2 = \pi 1000^2$) to get approximately the same area covered as the central ROI.

Image J was used to make line profiles of each phantom condition under both scatter and non-scatter corrected conditions. Line profiles were used as a metric of uniformity .

2.7 SNR, and Contrast analysis

SNR and contrast analysis were performed using a MatLab script that calculates the SNR and contrast of each sphere in the phantom. Choosing the signal ROI depended on the signal of interest and involved scrolling through the stack of each reconstruction to determine at which slice the signal was visibly strongest. Metrics used to determine which slice most correctly represented the signal of interest included determining which slice provided the largest area of the signal with the largest contrast, the least geometrical distortion, and greatest sharpness. Once a representative slice of the each signal was chosen, a circular ROI was selected such that it was as big as possible but within the visible boundary of the signal. Once the signal ROI was determined, four circular ROIs of the same size were selected around the signal ROI and spaced such that there was no overlap between the ROIs (Fig 2-8). Selecting four background ROI's for each signal allowed us to calculate four SNR, and contrast values for each signal. The same signal and background ROI sizes and locations were used for both the scatter and non-scatter corrected images. This procedure was repeated for each realization of each

signal containing phantom configuration. Error bars for SNR and contrast were calculated from the standard deviation of each respective calculation.

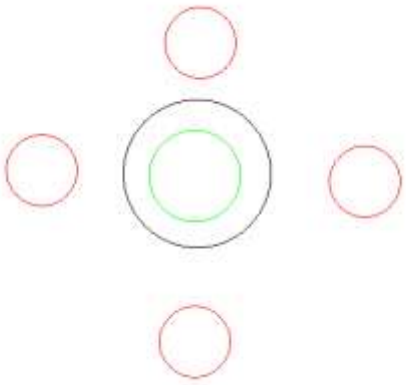

Figure 2-8: Representation of ROI selection. Black circle represents boundary of signal, green circle is the signal ROI, and red circles represent the background ROIs. Signal ROI was chosen such that it was large as possible but within the signal boundaries. Four background ROIs of the same area as the signal ROI were selected non-uniformly around the signal ROI and allowed for 4 SNR and contrast calculations per signal.

2.8 Detectability Observer Study

2.8.1 Detectability Observer Study Setup

Five medical physicists participated in a detectability observer study in order to determine the number of detectable spheres, and subsequently the smallest sphere detected, at the different radii under the different measurement and correction conditions. All image readings were done on a Sony Vaio E series laptop with a 15.5" LED backlit 1366x766 pixel display in a controlled environment, typical of a radiology reading room. Each study contained 120 randomly presented stacks of images, (approximately 20 slice-stacks per image set) of each phantom condition presented in Figure 2-2. An image stack was presented since the data is inherently 3D, and this allowed the reader to scroll through the data to try to find the spheres if they appeared more clearly on different planes. A representative slice of each sphere-containing configuration presented to each observer is shown in Figure 2-9.

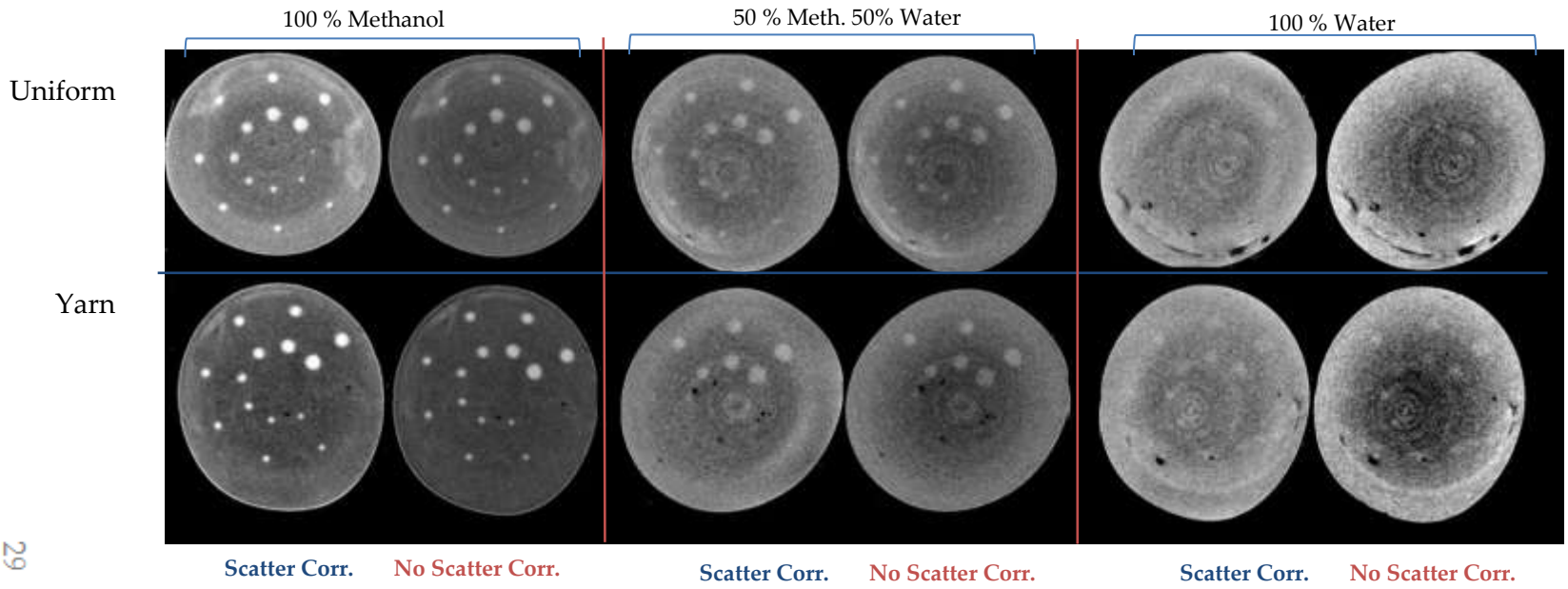

Figure 2-9: Matrix of reconstructed CT Acquisitions of the breast phantom for 3 background concentrations x 2 background noise conditions x 2 reconstruction conditions with and without scatter correction. Additional measurements included same conditions but without beads present. By combining the shown images with those others mentioned, and all their repetitions 5 times, there were a total of 60 scans. Image pairs are displayed in the same global maximum.

Presented images were in TIFF format and had a fixed window and level. Observers were able to scroll through the 20+ slices per image set. A screen capture of the setup is shown in Figure 2-10. The observers were provided with a schematic of the sphere locations (Figure 2-11) and given a short training set with obvious and not-so-obvious examples. Each reader was given a form and asked to indicate how many spheres they saw in each of the inner and outer radii (Figure 2-12).

2.8.2 Statistical Analysis of Detectability Observer Study

The resulting data was compared for significance using a Paired 2-tailed Student's t-test. Multiple comparisons of data pairs were made using the paired 2-tailed Student t-test, to determine if differences in detectability between given pairs were statistically significant. First, a comparison was done between uniform and yarn background for each of the inner and outer radii, respectively. Then the Student t-test was used to compare number of spheres observed in the inner vs. outer radius. Finally statistical differences were calculated between scatter and non-scatter corrected images. For each comparison 24 degrees of freedom were use since there were 5 repetitions of each case and there were 5 total observers resulting in 25 cases.

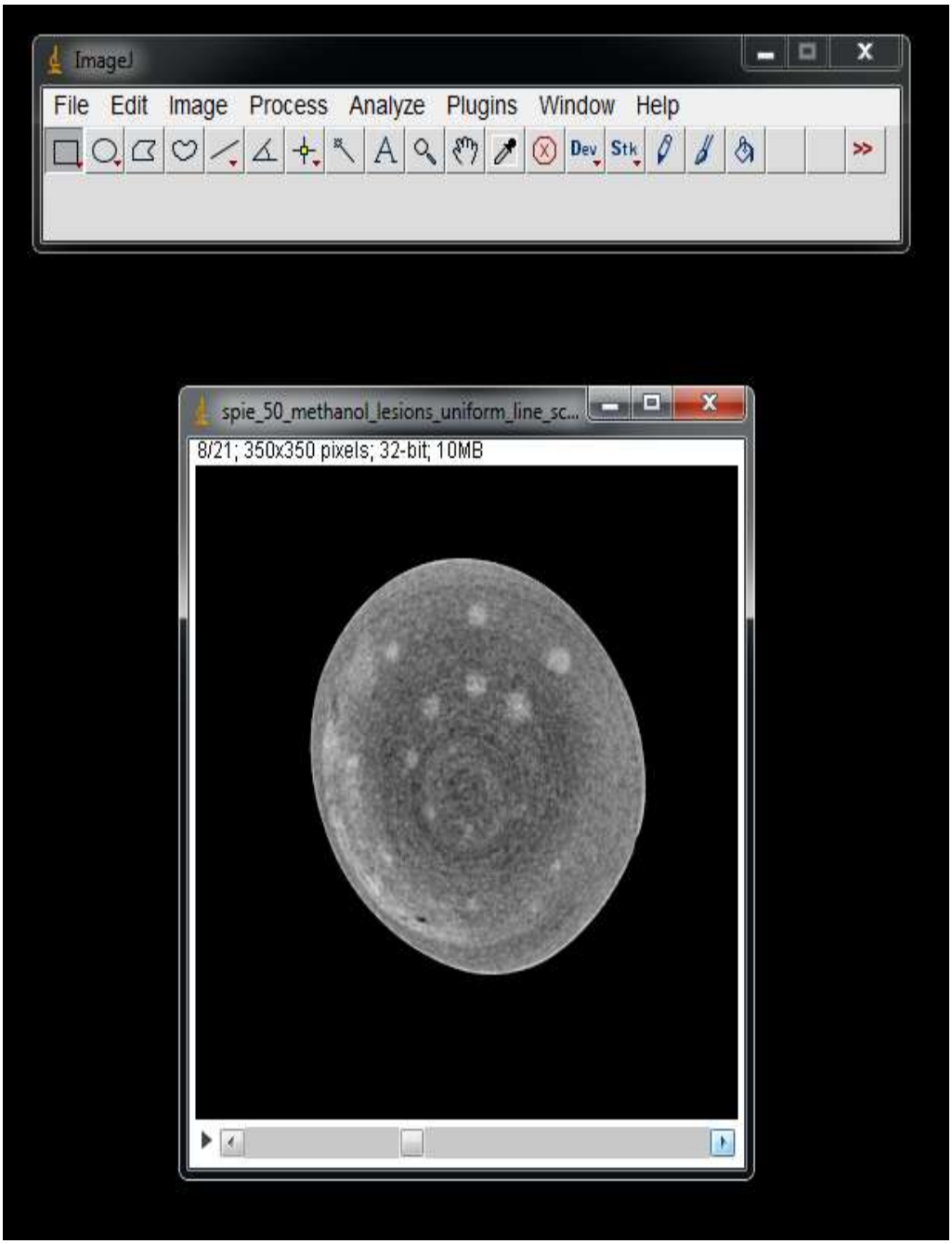

Figure 2-10: Screen Capture of Observer Study setup. Observers were given a stack of TIFF images and were allowed to scroll through the stack to determine number of visible spheres in the inner and outer radius.

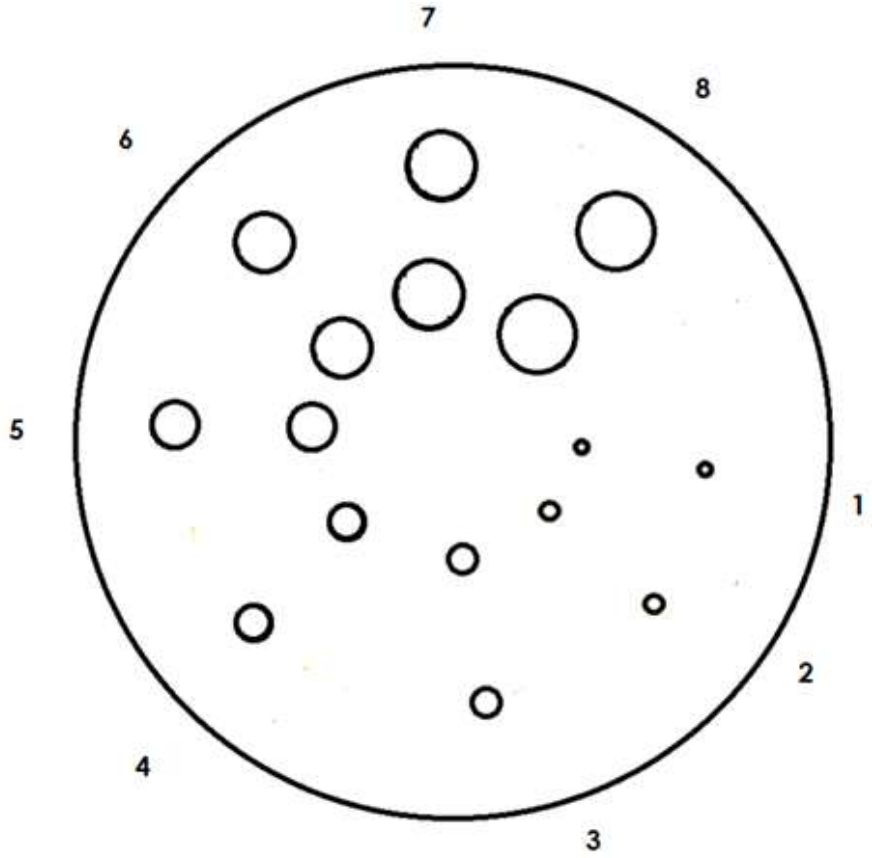

Figure 2-11: Instructions given to observers with illustration indicating the approximate location of the spheres, and how to input data into the survey sheet.

Instructions: Place an X in the appropriate numbered field in the spreadsheet for each sphere in the inner and outer rings, respectively. Largest Sphere should be at approximately the 2 o' clock position in all images.

Observer:										
		Smallest							Largest	
Set #										
		1	2	3	4	5	6	7	8	
1	Inner									Inner
	Outer									Outer
2	Inner									Inner
	Outer									Outer
3	Inner									Inner
	Outer									Outer
4	Inner									Inner
	Outer									Outer
5	Inner									Inner
	Outer									Outer
6	Inner									Inner
	Outer									Outer
7	Inner									Inner
	Outer									Outer
8	Inner									Inner
	Outer									Outer

Figure 2-12: Spreadsheet given to observers so that they could record the sphere sizes they saw on both the inner and outer rings of the lesion phantom.

2.9 2-AFC Observer Study

2.9.1 2-AFC background

In a two alternative forced choice (2-AFC) study, the observer is given two fields containing images of comparable noise. The signal has been randomly assigned to either field with equal probability. The observer is then asked to indicate which of the two fields has the image that contains the signal. This strategy of forcing the observer to pick one of the two images is based on the ideal Bayesian observer that uses all statistical information of the image to detect a signal [26]. By forcing the observer to choose between two noise containing images, the observer cross-correlates the signal with the image data at the two alternative locations and uses the two cross-correlation results as decision variables [26]. In other words, the observer determines two decision variable values (v_1 and v_2, with variances σ_1^2 and σ_2^2) one from the signal plus noise and the other from the noise only distribution. Then the observer is ”forced” to select the choice with the higher decision variable value. The experimenter determines the fraction of correct responses, P, for each case presented to the observer and then calculates the detectability index, explained below, that uses a transformation of the fraction of correct responses. In a 2-AFC study, chance performance is given as 50%, and thus P=75% means there is a 50% chance that the signal will be detected. A P value between 70-80% is known as just noticeable differences (JND) [26].

There are a couple of assumptions made in a 2-AFC experiment. One assumption is that the various sensory events involved in deciding between the two alternatives of

the detection task can be mapped onto a single parameter, probability of detection or detectability index. The other assumption is that the alternative observation intervals are statistically independent and that all probability density functions (PDFs) are Gaussian [26].

The detectability index comes from a z-score that depends on P. Detectability index is defined as

$$d' = \sqrt{2}z(P) \qquad (2.1)$$

Values corresponding to P have been calculated and put into a look up table (Table 2-2).

Table 2-2: Detectability index, d', values corresponding to the proportion of correct responses; P. M value indicates number of alternatives. This table shows that the same detectability index is used for ROC and 2-AFC experiments. This table has been adopted from [26].

P or A_z	ROC	M=2
0.1	…	…
0.2	…	…
0.3	…	…
0.4	…	…
0.5	0.0	0.0
0.6	0.36	0.36
0.7	0.74	0.74
0.8	1.19	1.19
0.9	1.81	1.81
0.95	2.32	2.32

d′ is a useful metric in addition to the fraction of correct responses because unlike P, d′ can range from 0 to infinity. Therefore since d′ does not have the compressive nature as is the case when P approaches unity, changes in detection as the signal amplitude increases are equally incremented in d′. Thus d′ can be viewed as a measure designed to scale reasonably with SNR. In this way, if SNR is zero then one should expect d′ to be zero. Similarly, equal changes in SNR will be reflected as equal changes in d′. A plot of d′ vs SNR is shown in Fig. 2-13.

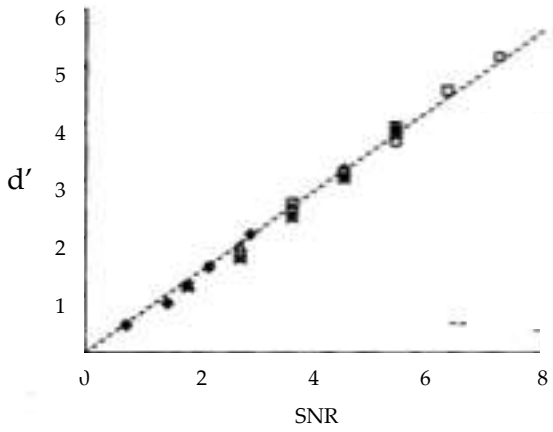

Figure 2-13: d′ vs. SNR for 2-AFC studies (figure obtained from [26]).

Detectability in 2AFC experiments is usually estimated assuming no observer bias, meaning that the observer does not have a preference of selecting one field over

another. Given N trials of fixed signal amplitude, the variability in the proportion of correct response, P, is determined by the binomial distribution with variance:

$$s(P)^2 = P(1-P)/N \tag{2.2}$$

the variance of d' is described by:

$$s(d')^2 = 4\pi \exp\left[\frac{(d')^2}{2}\right] s(P)^2 \tag{2.3}$$

The 2-AFC study has been traditionally applied to signal-known-exactly/background-known-exactly (SKE/BKE) cases where the signal is known exactly (size, shape, locations) and a known background that is usually uniform [26]. In a SKE/BKE case the only source of uncertainty comes from the image noise. Due to the simplifications provided by having SKE/BKE, 2-AFC studies have been highly used with synthetic computer-generated images or images produced from scanning a phantom where one has complete control of the "ground truth". Knowing exactly where the signal is allows the experimenter to place the signal approximately at the center of one of the two fields.

The main benefit of the 2-AFC study is that the efficiency of the study allows observers to go through the study relatively quickly. Unlike a receiver operating characteristic (ROC) study, where observers are shown images that may or may not contain a signal and observers respond with a rating of confidence as to whether they

detect a signal, the 2-AFC study allows users to decide the presence of a signal in matter of seconds. While the ROC method makes the fewest assumptions and hence is the most robust, under controlled experimental conditions the ROC and 2-AFC methods can be compared directly because the area under the ROC curve is equivalent to P [26]. However it is known that the ROC method requires half as many trial pairs as the 2-AFC method for a given variance. Deciding between an ROC study and 2-AFC study depends on the experiment. If the experiment is largely under the experimenter's control and images can be easily reproduced, the 2-AFC experiment is the better choice [26].

2.9.2 2-AFC setup

Prior to conducting the 2-AFC study, statistician Dr. Kingshuk Choudhury performed a power analysis based on a two sample proportions test to compare the proportion correct in each group. In this power analysis it was assumed that an equal number of cases were viewed in each group and that all cases were marked independently of each other. The test statistic was set up with a 5% false positive rate. Two different cases were considered, one a hard case, where there is a small difference in the detectability between scatter corrected and non-scatter corrected images (1.25%) and a second with a larger difference (6.2%). The resulting power curves indicate that at least 2600 cases are required to achieve 90% power in the first scenario (Figure 2-14). Assuming an experiment with 480 image cases this implies at least 6 readers.

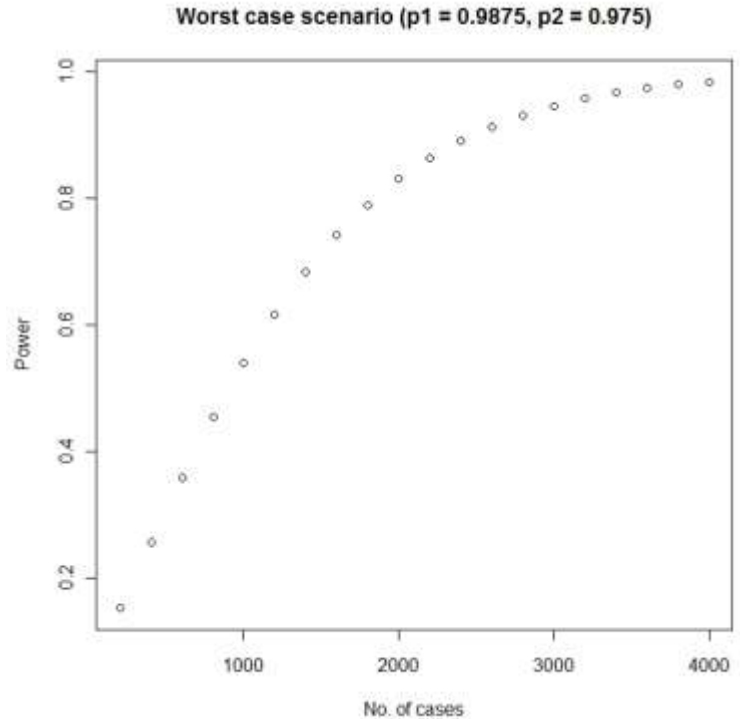

Figure 2-14: Power analysis for worst-case scenario (1.25 % difference in detectability between scatter corrected and non scatter corrected images).

In the best-case scenario (6.2% difference), at least 1400 cases are required to achieve 90% power (Figure 2-15). This translates to at least 3 readers.

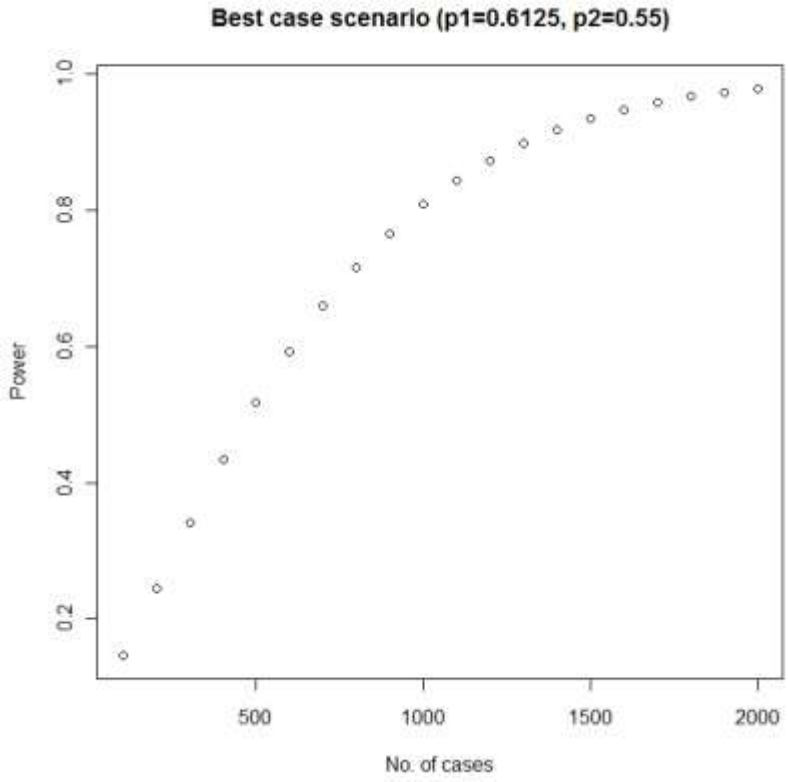

Figure 2-15: Power analysis for best-case scenario (6.25 % difference in detectability between scatter corrected and non-scatter corrected images).

While the power analysis represents a simplification of the actual experiment, which has a more complex structure than a two sample comparison, it gives a rough idea as to how many readers we should consider.

Matlab was used to create a graphical user interface (GUI) that randomly presents 480 image pairs (one containing a signal, and one without the signal simultaneously) of same noise structure to the observer. The signal containing a 40x40

pixel image pair was randomly presented in one of the 2 panels of the GUI. It was the task of the observer to determine which panel of the GUI contained the signal by typing "a" for left panel or "d" for right panel. A screen capture of the experimental setup is provided in Fig. 2-16.

A script in Matlab was used to crop 40x40 pixel ROIs of the signals within background and background-only data presented in Figure 2-16. A 40x40 pixel ROI was selected because it allowed cropping of the signals without overlap in the inner radius where the spacing between signals was limited. The Matlab script insured that same 40x40 ROI was selected for both the scatter and non scatter corrected images, the signal was approximately at the center of the ROI, and that the background ROI (no signal) was from the same relative location as the signal in a background-only phantom. In this way, the background ROI was selected on the same radial position as the signal. The 40x40 pixel ROIs of signal + background and background were magnified to 160% to fit in the window panel of the GUI. Presented images were at a fixed window and level, and both images in the presented image pair had the same background texture(yarn or uniform), were from the same location (inner or outer radius) were in the same concentration (50% methanol 50% water or 100% water) and under the same scatter conditions (scatter corrected or non-scatter corrected).

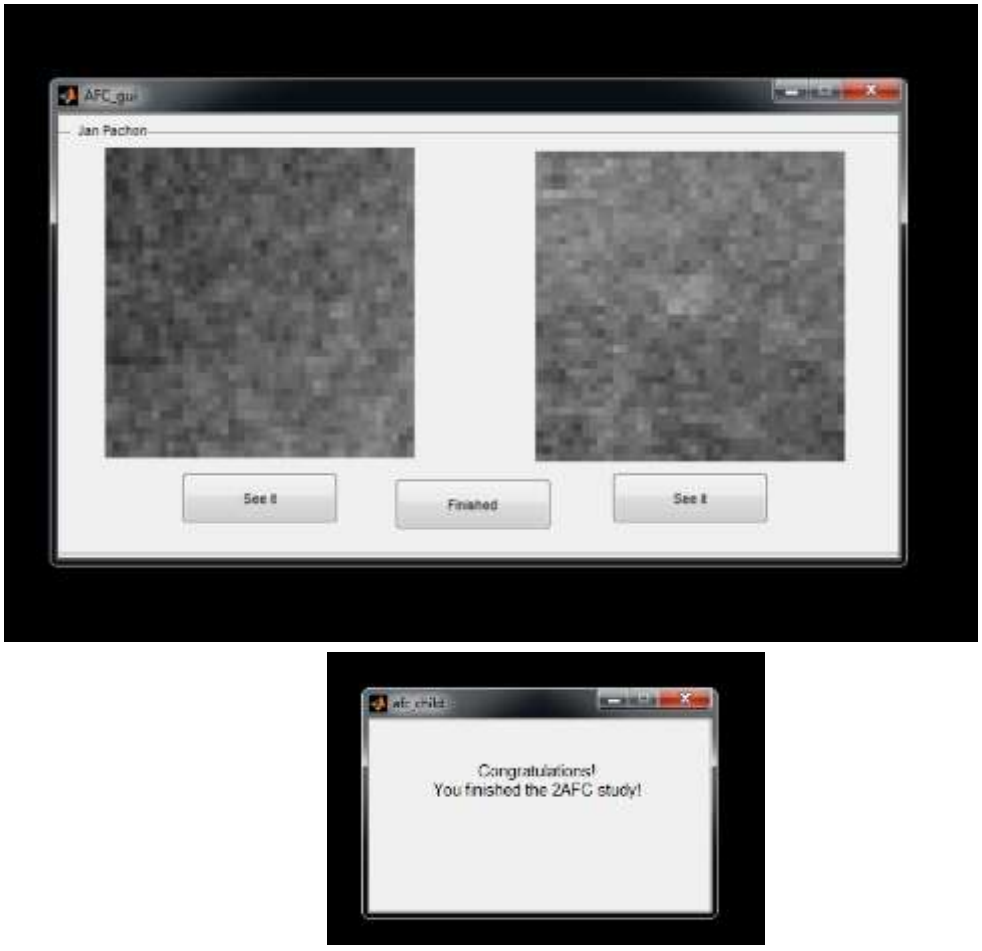

Figure 2-16: Screen capture of 2-AFC experimental setup. (TOP) GUI containing two panels, one of which contains the signal. Observer types "a" to indicate signal is on the left and "d" to indicate signal is on the right. (BOTTOM) window that shows up when observer has been presented with all 480 image pairs and thus completed the study.

A DICOM calibrated medical grade LCD display monitor, in accordance to AAPM TG18 guidelines, from Barco model number MDCG 3120-CB under low ambient lighting conditions (lights dimed to 1/3) was used for this study. Nine medical physicists participated in this study. Each observer was presented 480 image pairs representing 6 sphere sizes under each phantom configuration (Fig. 2-17).

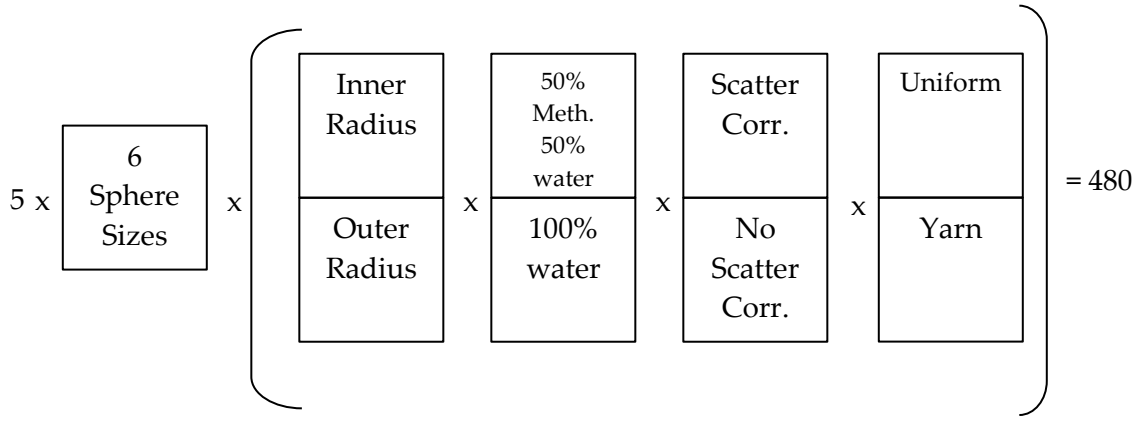

Figure 2-17: Data matrix: 6 sphere sizes (1-6 mm) from both inner and outer radius in breast phantom with 2 different concentrations were acquired 5x under 4 conditions: (1) in Uniform background (2) In yarn background (3) with and (4) without scatter correction.

The observers were provided a document with instructions (Fig 2-18) on how to use the GUI and a schematic of the sphere sizes they would be presented with. After reading the instructions, observers were given a short training set containing 40 image pairs with obvious and not-so-obvious examples.

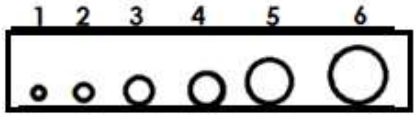

Signal Size ranging from 1-6 mm

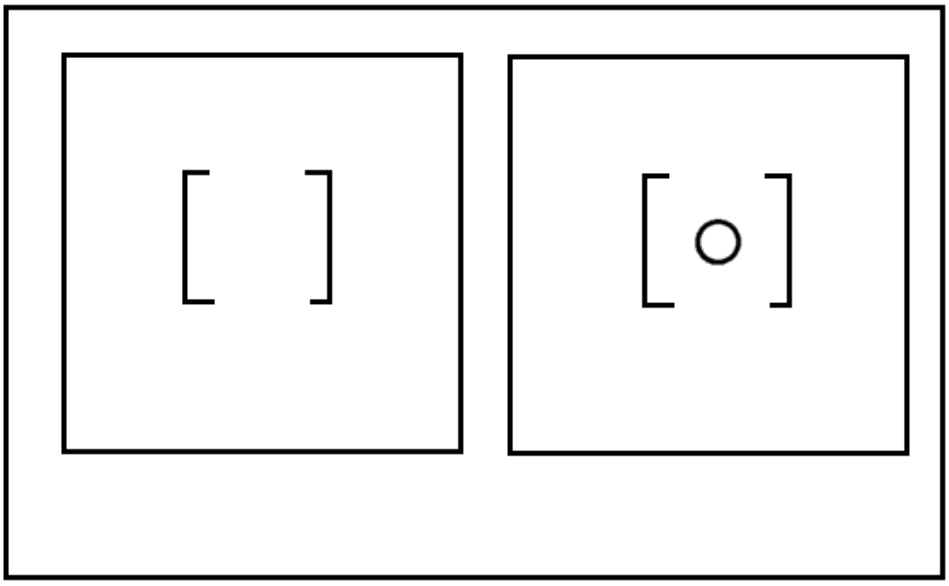

Instructions: A signal ranging in size as indicated in FIG.1 will be presented randomly in either the left or right panel, but not both, of the GUI. Select which panel contains the signal by typing "A" for left panel or "D" for right panel. The signal will be located in the central region of each panel, indicated by the brackets in FIG. 2. The selection should take about 5 seconds per image pair, but take as much time as you like.

Figure 2-18: Instructions given to the observer with drawing of GUI of left and right panel. Signal will be centrally located within the indicated bracket.

The GUI kept track of the correct responses for each case presented in figure 2-17 for each user. Data analysis used both the portion of correct responses, P, and

detectability index to compare detectability performance between scatter and non-scatter corrected images for each concentration and radial location.

2.9.3 Statistical Analysis of 2-AFC Observer Study

For the multi reader multi case (MRMC) 2-AFC observer study, Dr. Kingshuk Choudhury, performed a chi-square test to determine the overall effects of each variable (scatter correction, signal size, concentration, location, and reader) in our experiment on the detection task. He first measured the significance of scatter correction on the detection task by determining the total number of scatter and non-scatter corrected cases detected independent of size, concentration (contrast), reader, and location. He then measured the effect of concentration (independent of signal size, scatter correction, location and reader), size (independent of scatter correction, concentration, location, and reader), location (independent of scatter correction, concentration, size, and reader), and finally the inter-observer variability (independent of scatter correction, concentration, location, and size).

After performing the significance testing of each factor on the detection process, Dr. Choudhury used a logistic regression model to determine the response (probability of detection) as a linear combination of the factors, including two and higher order interactions between factors. The models were then fitted by the method of maximum likelihood. The quality of the fit was measured by the Akaike's information criterion

(AIC). The results of the logistic regression model are presented in the appendix since this is Dr. Choudhury's work.

3. Results

3.1 Line profiles

As expected, the line profiles through all the images (Fig. 3-1,3,5) show that attenuation values improve (increase) and cupping artifacts decrease for scatter corrected images (Fig. 3-2,4,6). The line profiles also suggest an increase in contrast of the spheres.

Results are presented so that the line profiles are underneath the coronal slices where the line profile was taken.

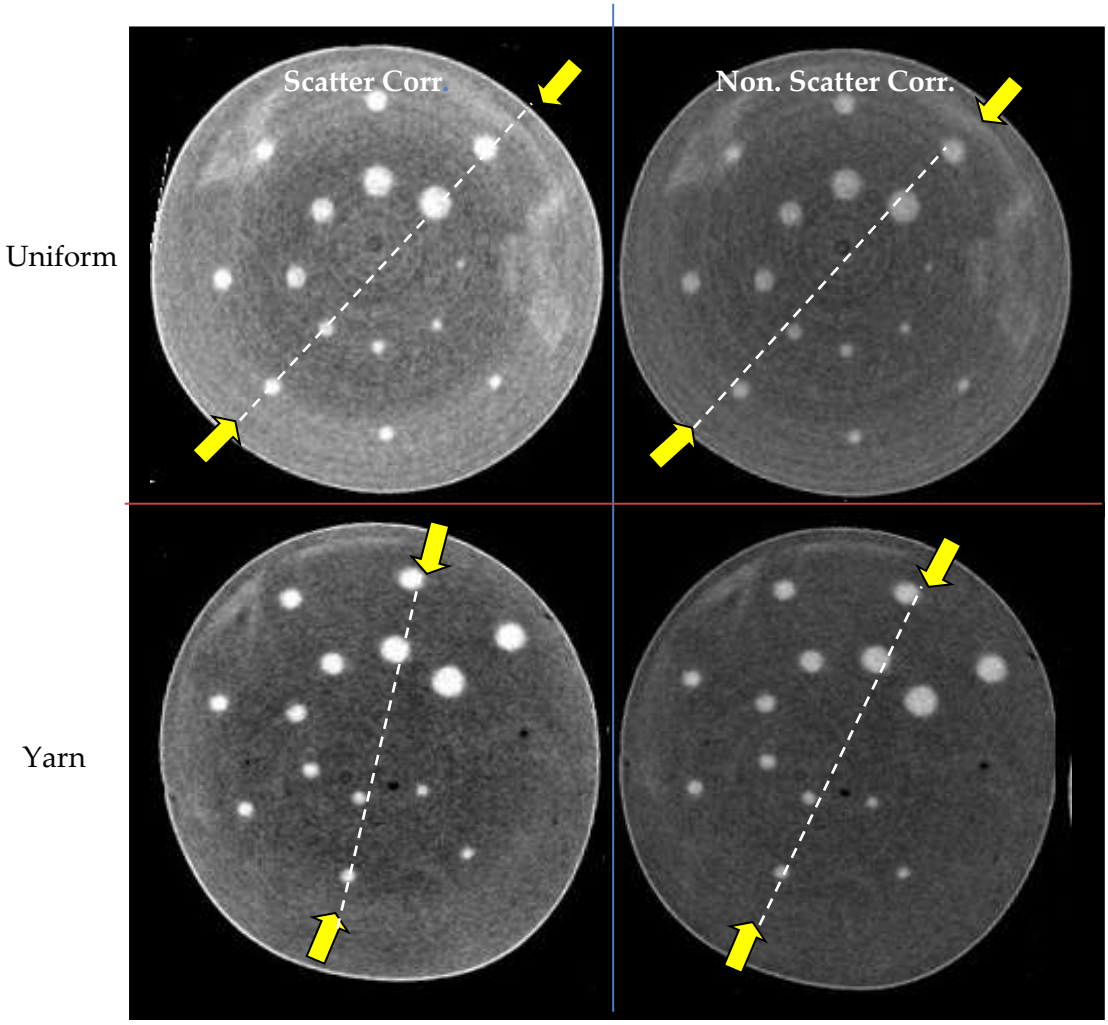

Figure 3-1: Matrix of Coronal slices of breast phantom containing 100% Methanol in uniform and yarn background under scatter and non-scatter corrected conditions. Arrows and dashed white line indicate where line profile was taken.

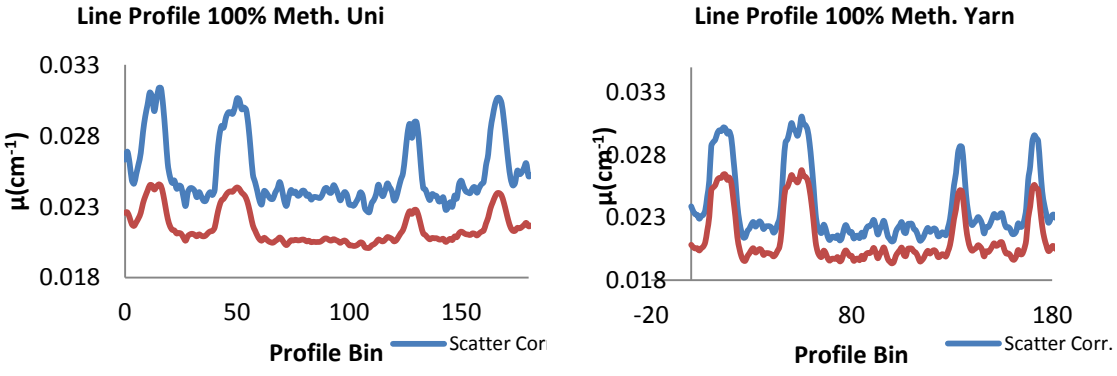

Figure 3-2: Line profiles in 100% Methanol density in (LEFT) uniform and (RIGHT) yarn background

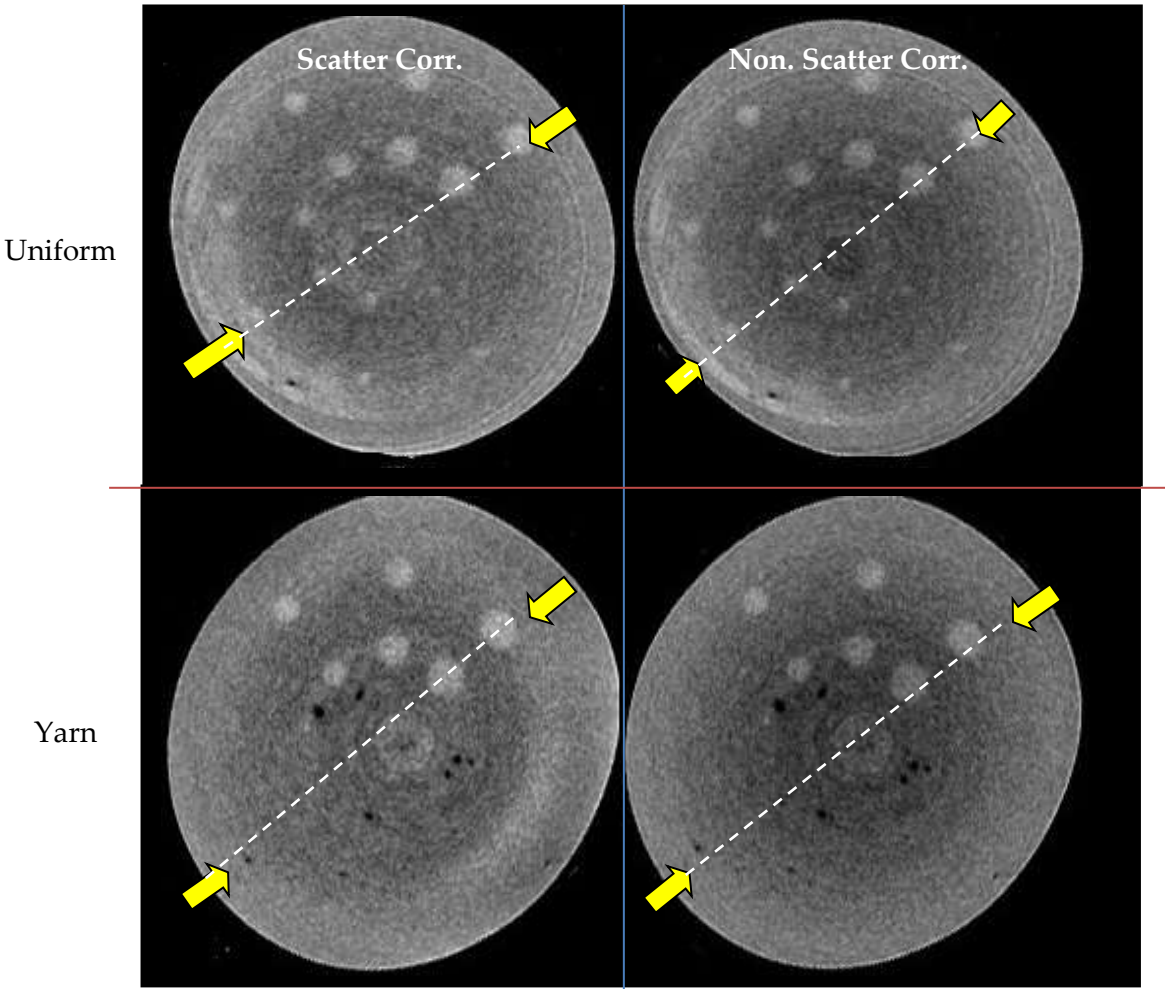

Figure 3-3: Matrix of Coronal slices of breast phantom containing 50% Meth. 50% Water

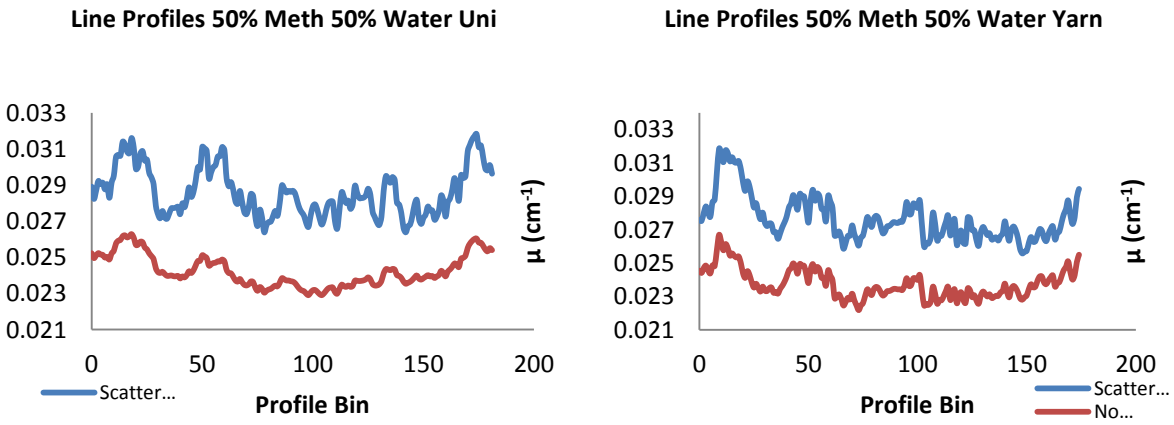

Figure 3-4: Line profiles in 50% water 50% Methanol density in (LEFT) uniform and (RIGHT) yarn background.

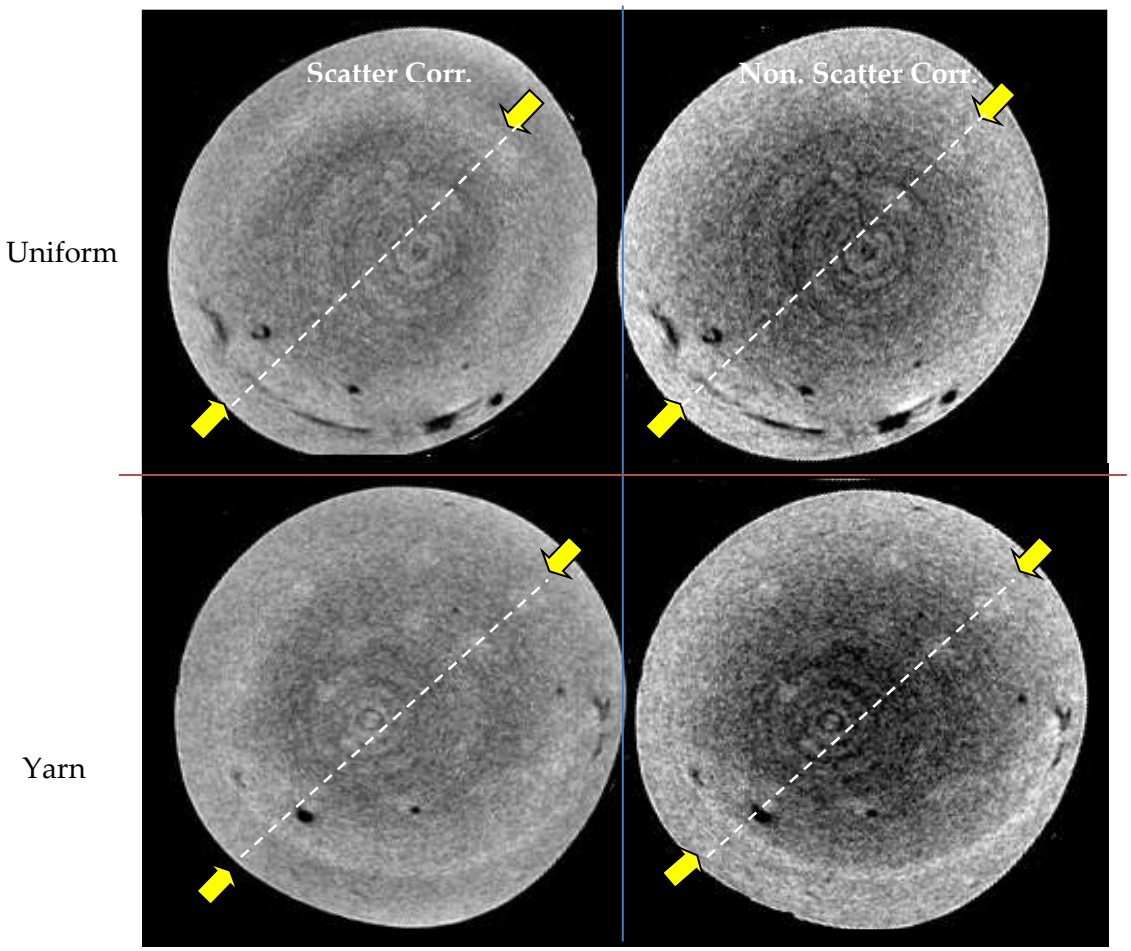

Figure 3-5: Matrix of Coronal slices of breast phantom containing 100% Water in uniform and yarn background under scatter and non-scatter corrected conditions. Arrows and dashed white line indicate where line profile was taken.

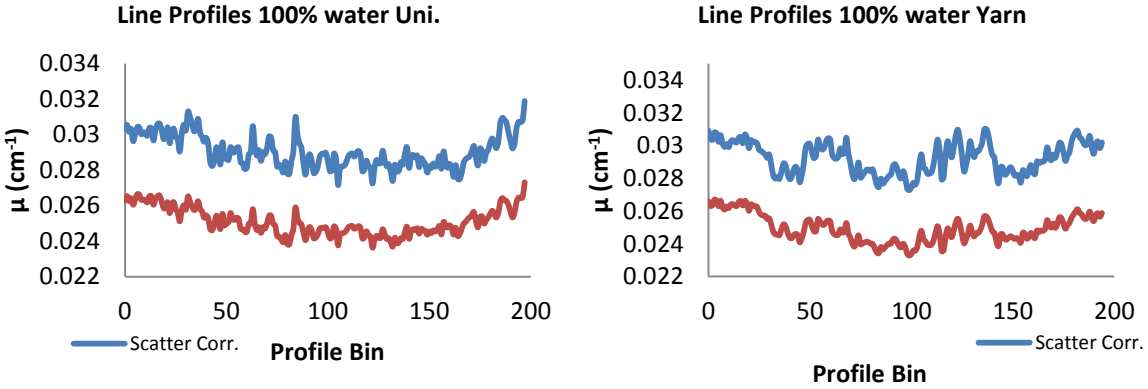

Figure 3-6: Line profiles in 100% water density in (LEFT) uniform and (RIGHT) yarn background.

3.2 Non-uniformity

Non-uniformity was calculated using equation 1.5 to characterize the degree of cupping in scatter and non-scatter corrected images. The central ROI had a radius of 100 pixel and each edge ROI had a radius of 44.74 to get approximately the same area covered in the central and edge region ($5 * \pi\sqrt{2000}^2 = \pi 100^2$). The non-uniformity results indicates less non-uniformity in the scatter corrected images (Fig 3-8).

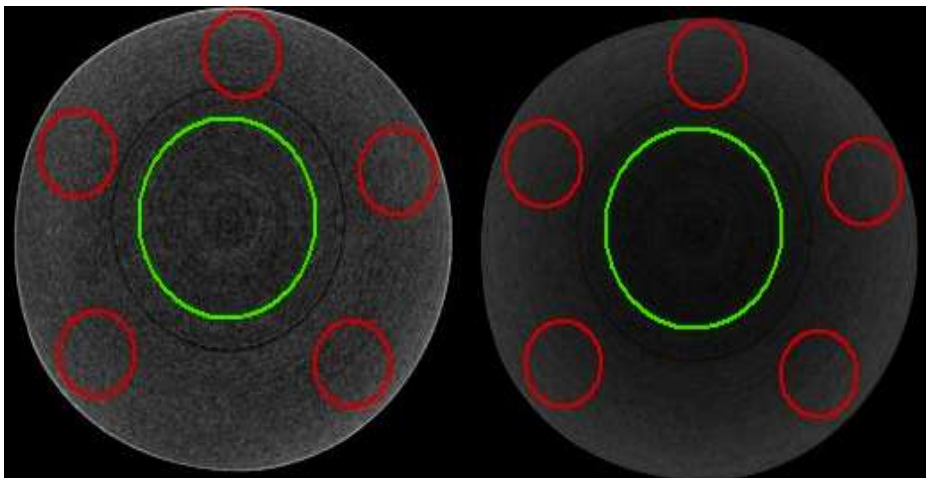

Figure 3-7: Coronal slice through (LEFT) scatter corrected and (RIGHT) non scatter corrected breast phantom containing 100% Methanol. Green ROI (radius of 100 pixels) represents central region used in non-uniformity calculation. 5 red (radius- 44.72 pixels) ROIs are the edge ROIs.

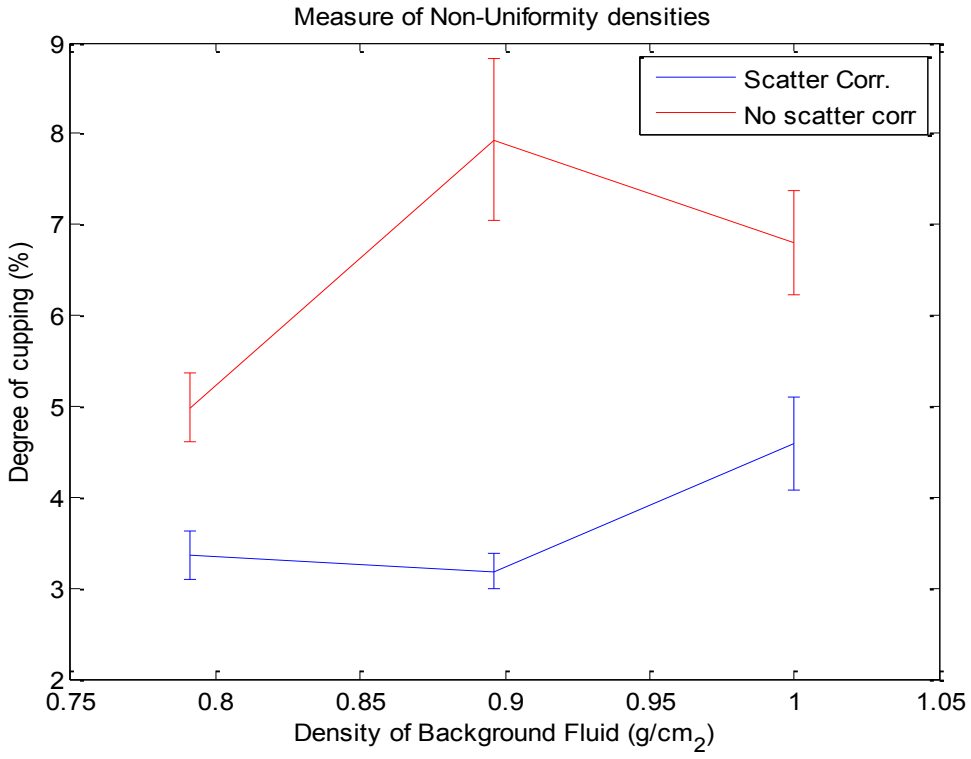

Figure 3-8: Plot of non-uniformity as a function of background fluid density in the breast phantom for scatter and non-scatter corrected images.

3.3 SNR and Contrast Analysis

Figures 3-14, 17, and 20 show representative ROIs for SNR and contrast calculations for each concentration examined. Plots of SNR (defined in eq. 1.4) indicate the increase in noise, and subsequent decrease in SNR, that results from scatter correcting (Figs 3-10,13,16). With scatter (or any) correction there is an increase in noise in the final data that in CT reconstruction is also exacerbated by the log of the ratio of the corrected data. This could amplify the decrease in reconstructed image SNR. Significant improvements in contrast (defined in eq.1.3) were seen for scatter corrected data for each

concentration examined (Figs 3-11,14,17). A comparison of contrast between inner and outer radius for scatter correction (Figs. 3-18,19) signifies that there is excellent similarity in the results comparing the bead contrast in the inner and outer radii. While the data is somewhat noisy, especially in the lowest contrast 100% water case, the mean values and trends indicate that scatter correction appears to equalize the contrast values regardless of bead location in the phantom

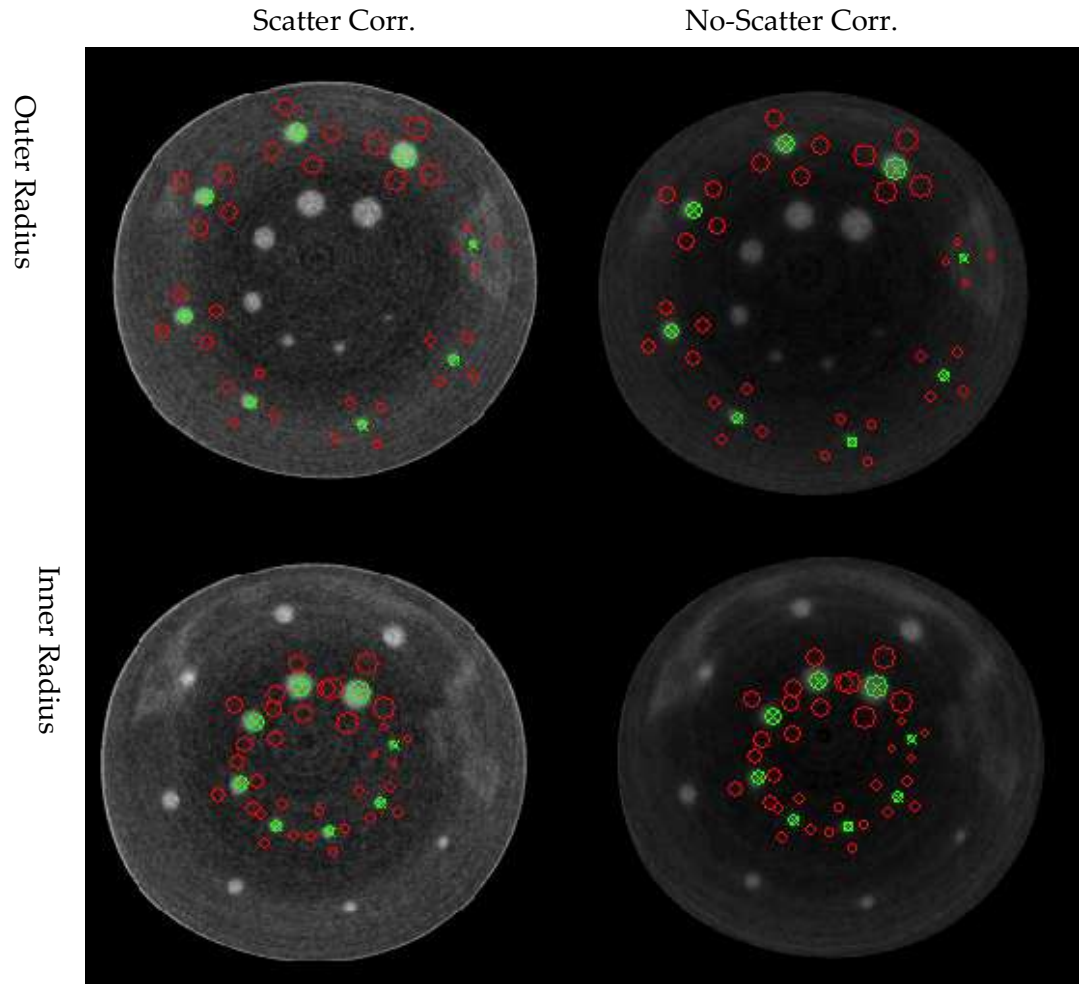

Figure 3-9: Signal (GREEN) and background (RED) ROI selection for spheres in 100% Methanol. Top row represents slice that contained all outer radius spheres, while bottom shows slice that best represented all inner radius spheres.

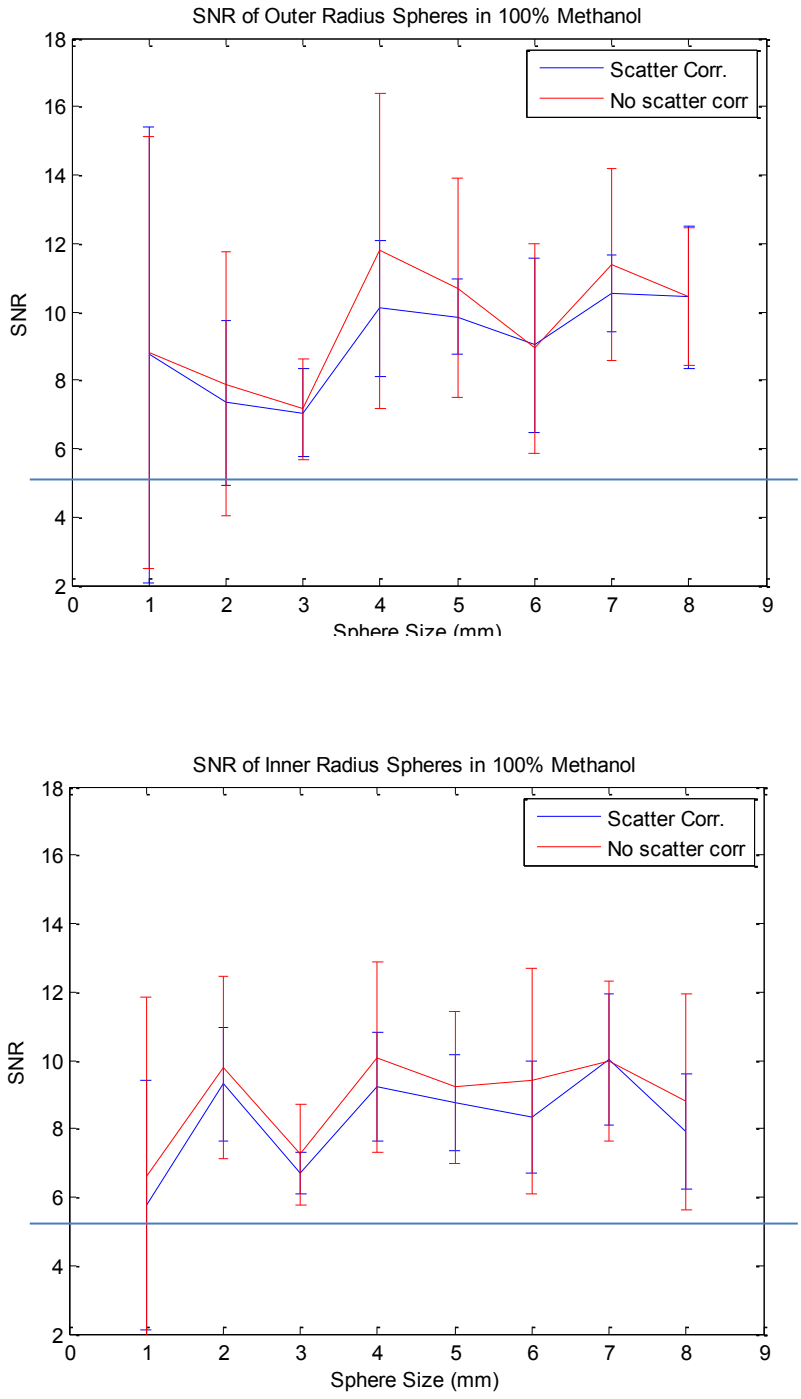

Figure 3-10: SNR plots for (TOP) outer radius spheres (BOTTOM) inner radius spheres in 100% Methanol. Blue bar signifies a SNR of 5 indicating the minimum criterion from the Rose model.

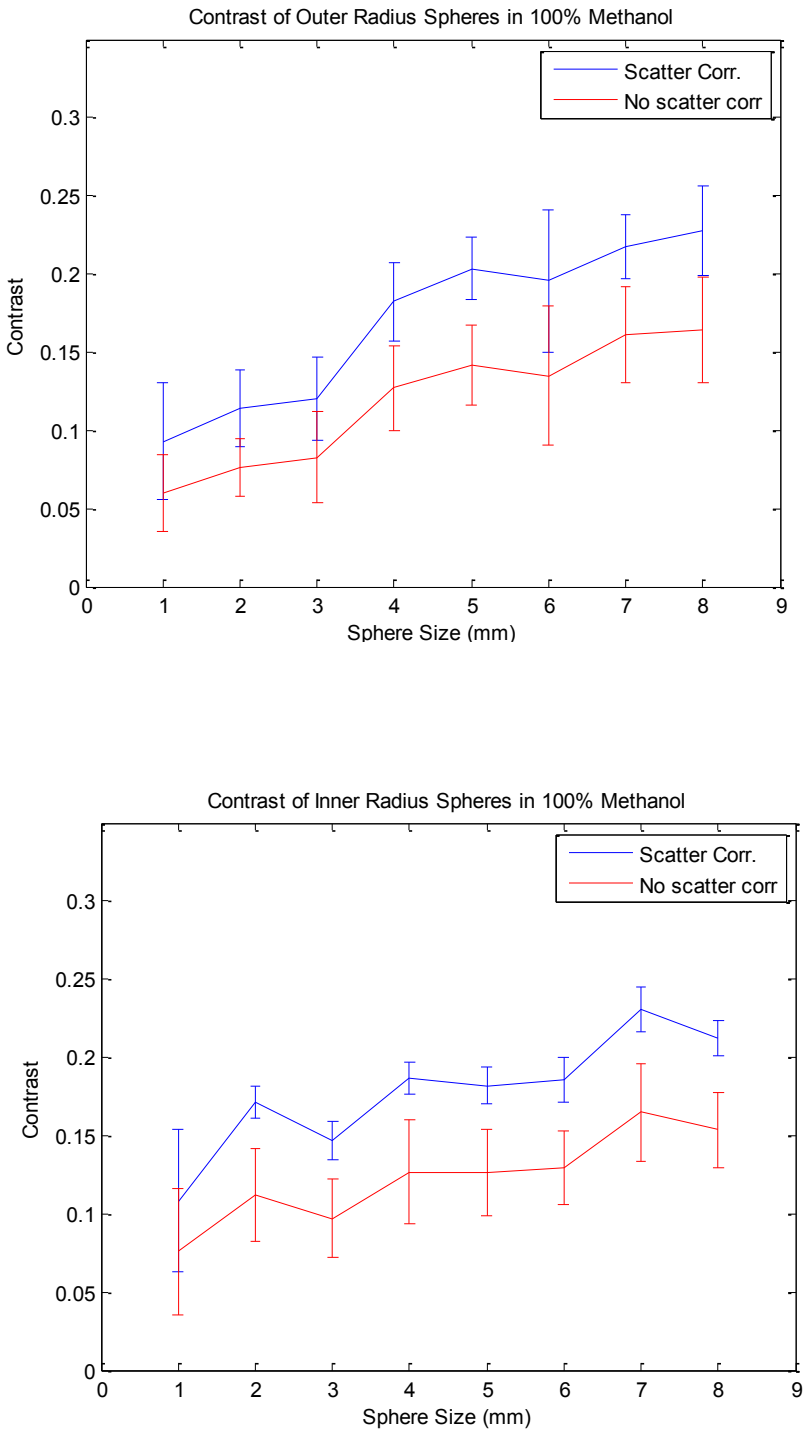

Figure 3-11: Contrast plots for (TOP) outer radius spheres (BOTTOM) inner radius spheres in 100% Methanol.

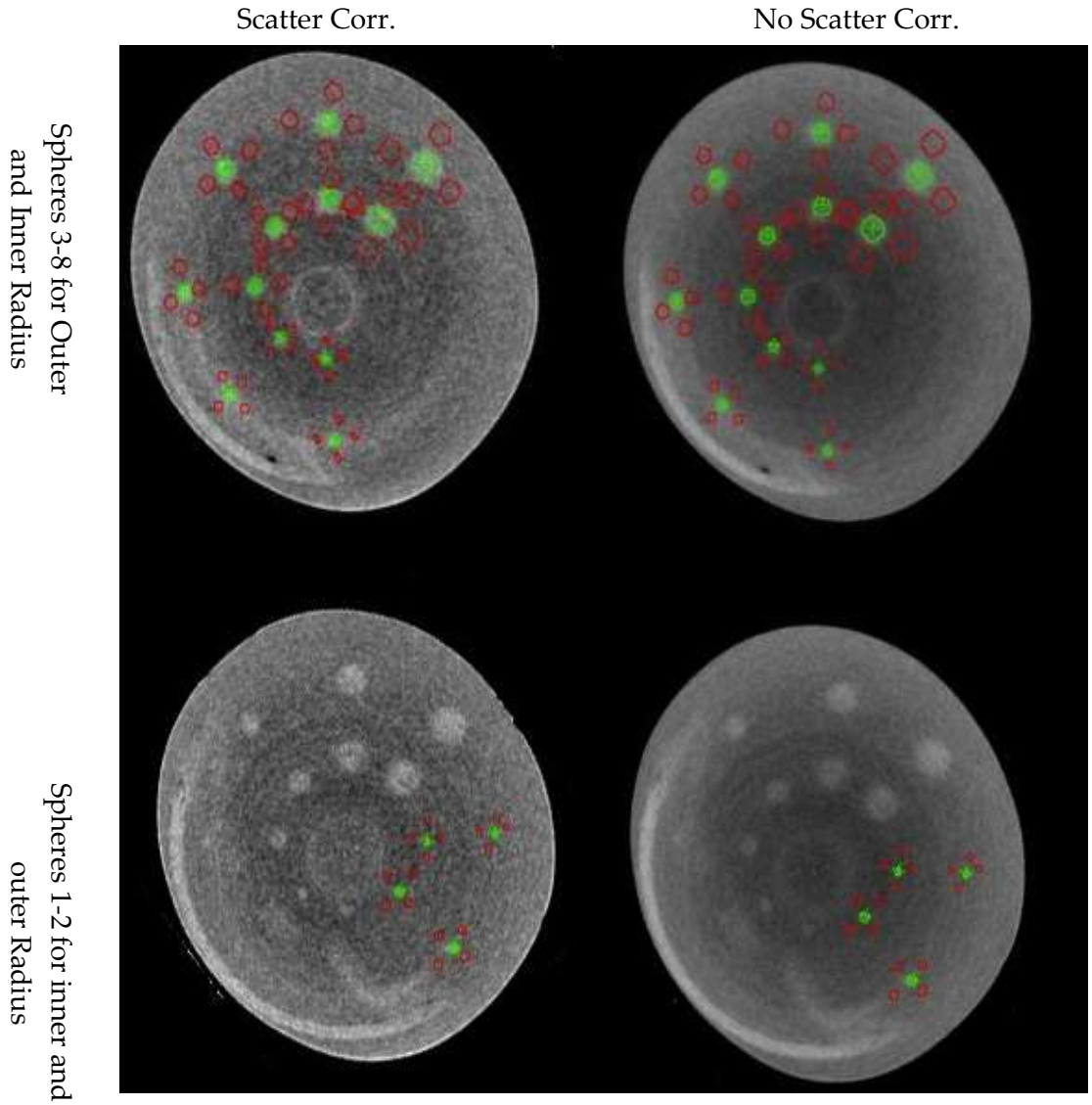

Figure 3-12 Signal (GREEN) and background (RED) ROI selection for spheres in 50% Methanol 50% Water. Top row represents slice that contained spheres 3-8 in inner and outer radius spheres, while bottom shows slice that best represented spheres 1-2 in inner and outer radius.

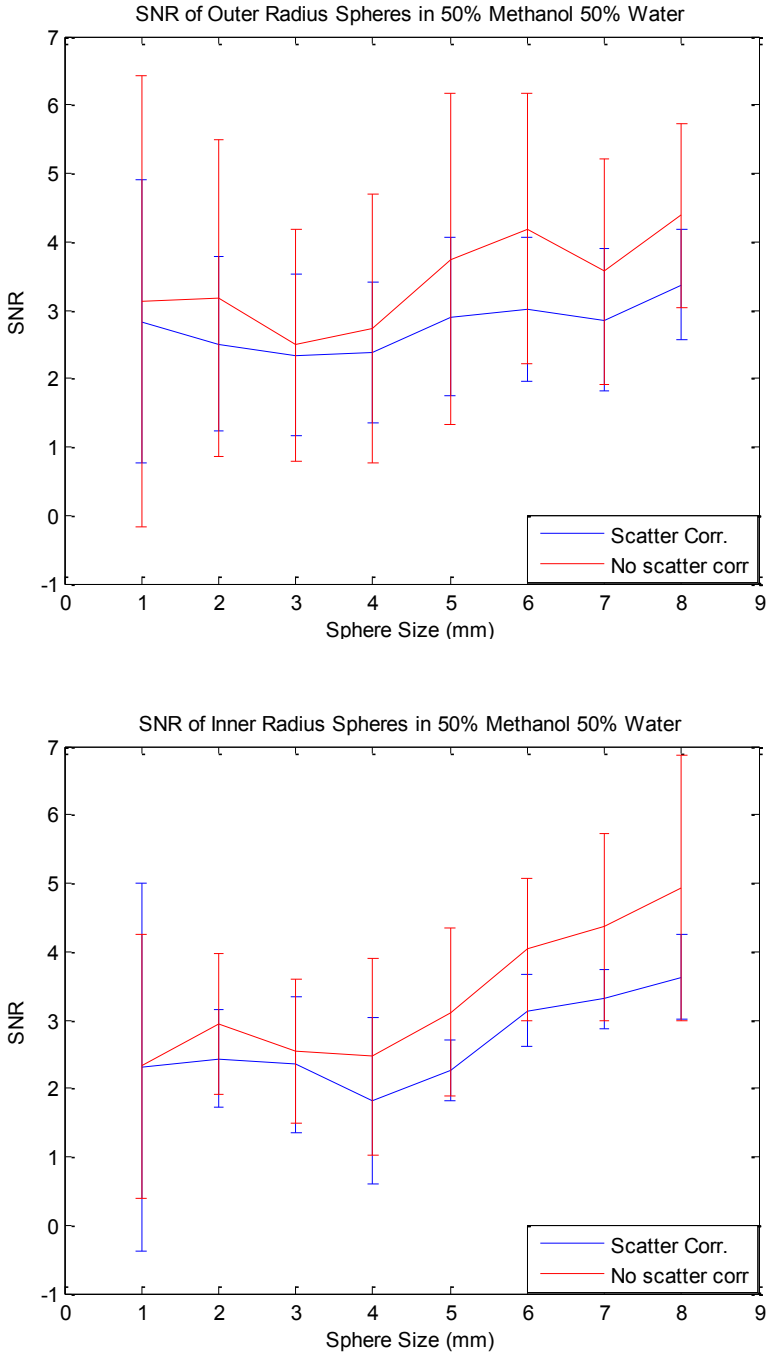

Figure 3-13: SNR plots for (TOP) outer radius spheres (BOTTOM) inner radius spheres in 50% Methanol 50% water. Blue bar signifies a SNR of 5 indicating the minimum criterion from the Rose model.

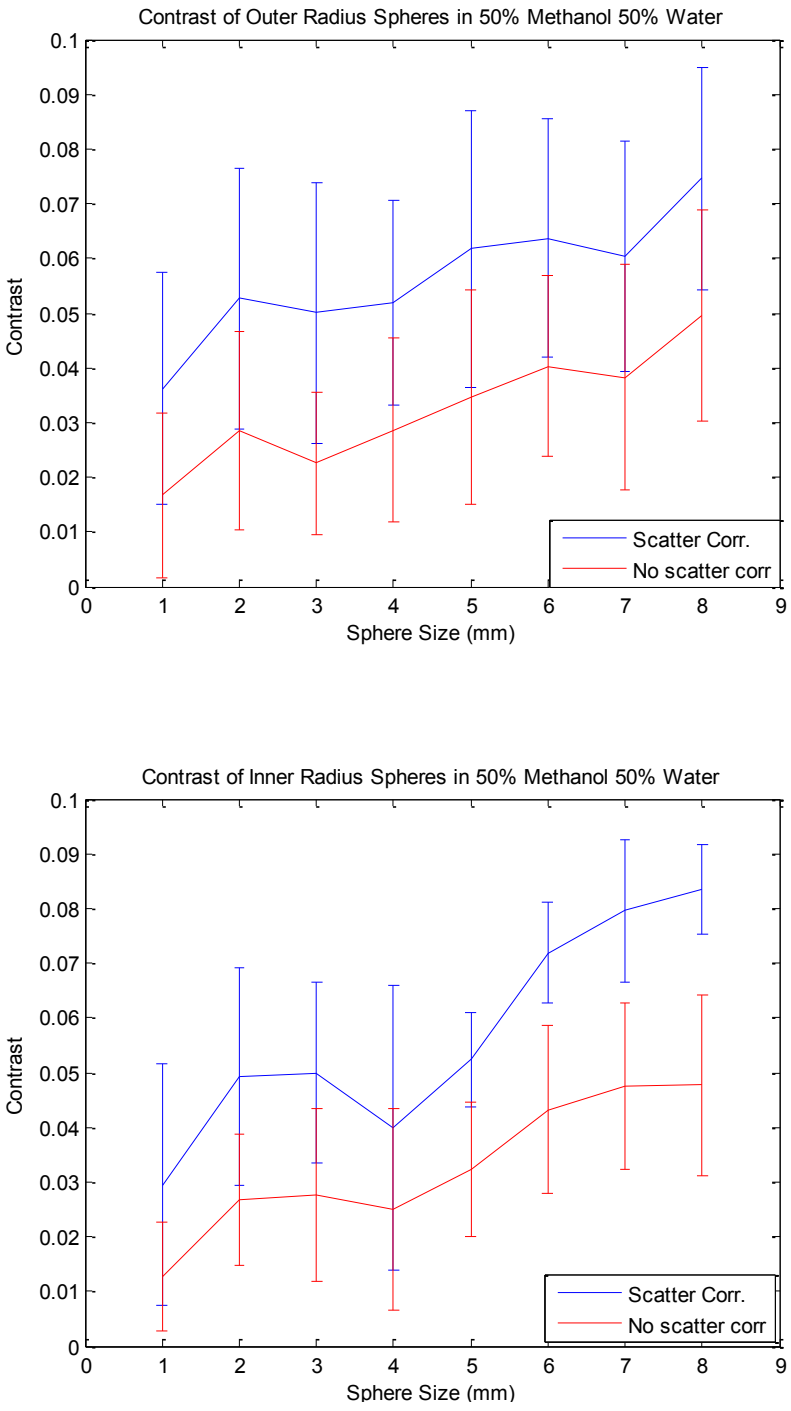

Figure 3-14: Contrast plots for (TOP) outer radius spheres (BOTTOM) inner radius spheres in 50% Methanol 50% water.

Scatter Corr. No Scatter Corr.

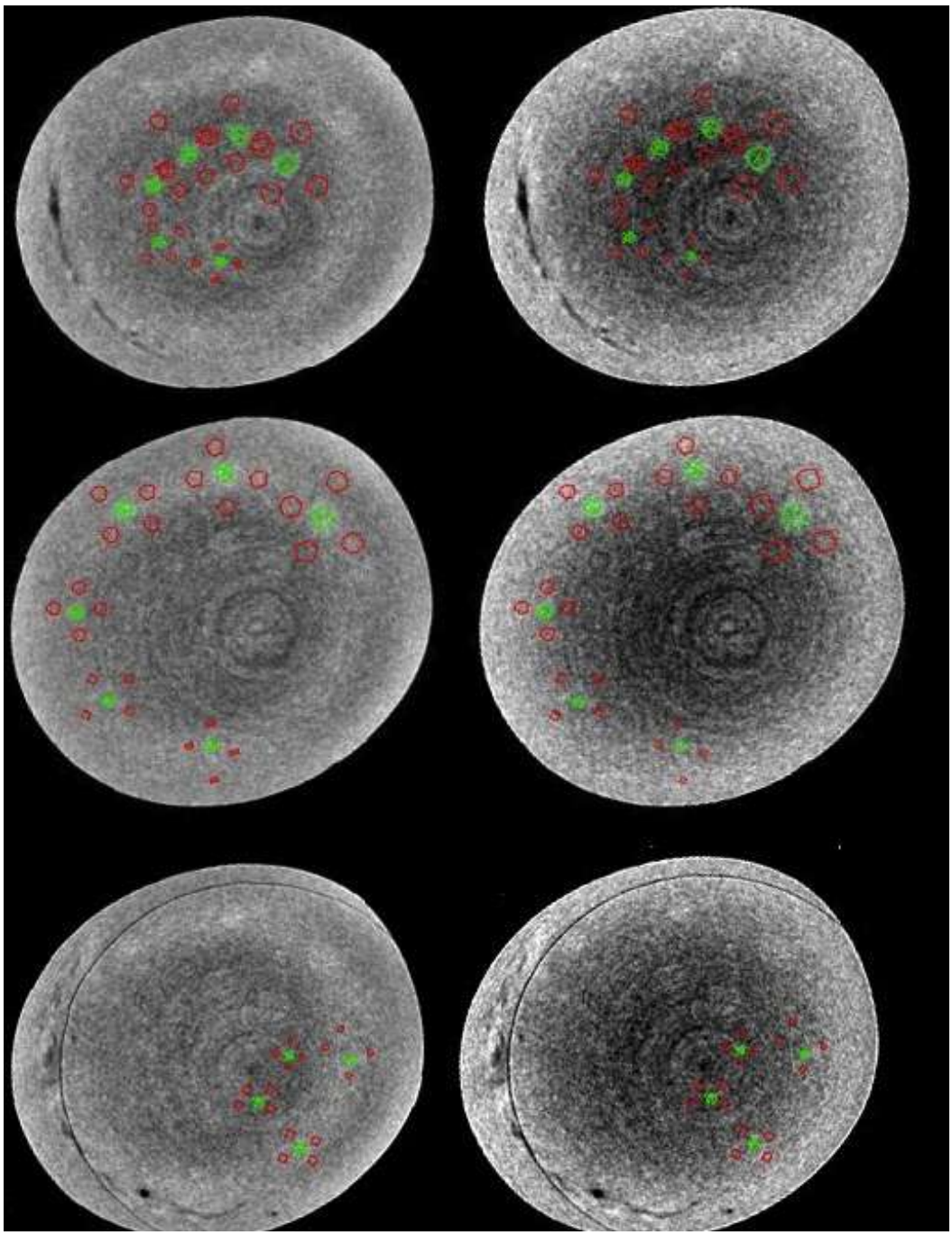

Figure 3-15: Signal (GREEN) and background (RED) ROI selection for spheres in 100% Water. These are representative slices that contained spheres 3-8 in outer radius (TOP row), sphere 3-8 in inner radius (MIDDLE row), and sphere 1 &2 for both inner and outer (BOTTOM row) .

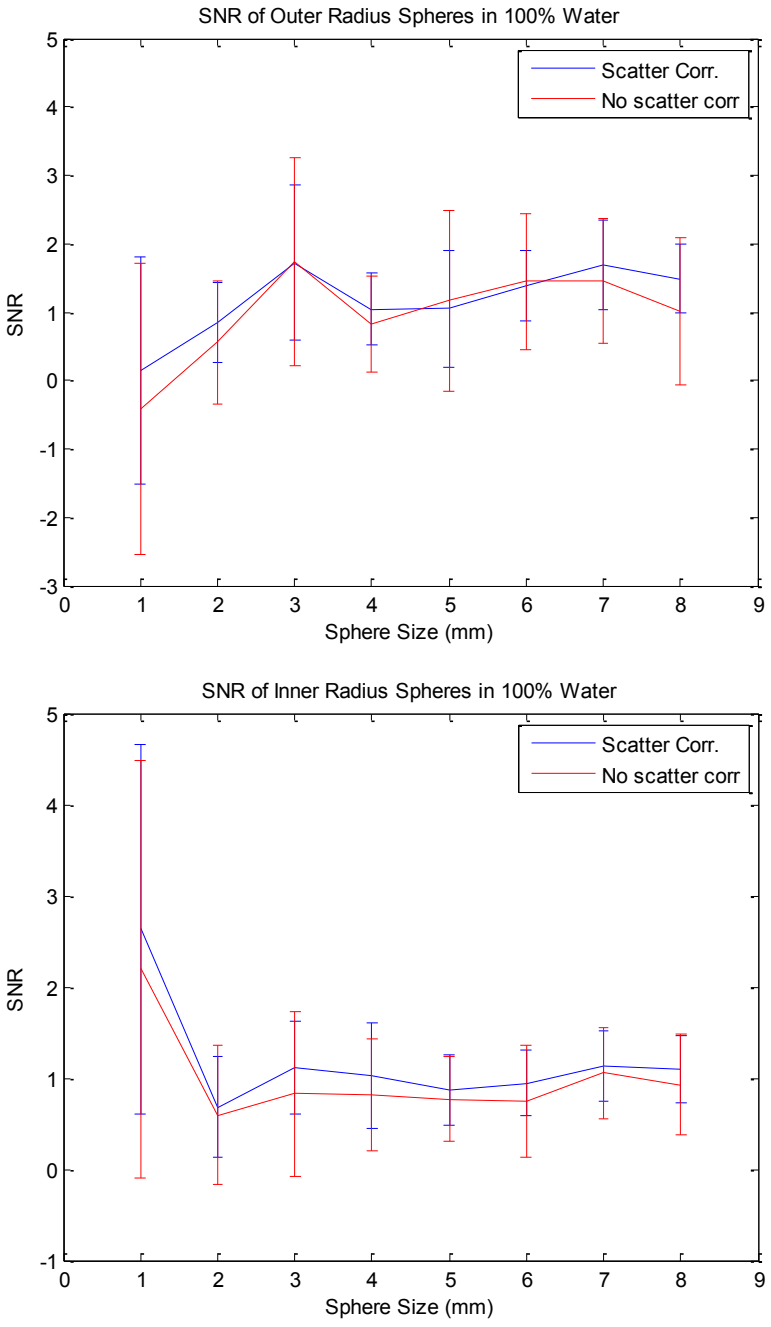

Figure 3-16: SNR plots for (TOP) outer radius spheres (BOTTOM) inner radius spheres in 100% water. SNR of 5 is at the top of each plot indicating the minimum criterion from the Rose model.

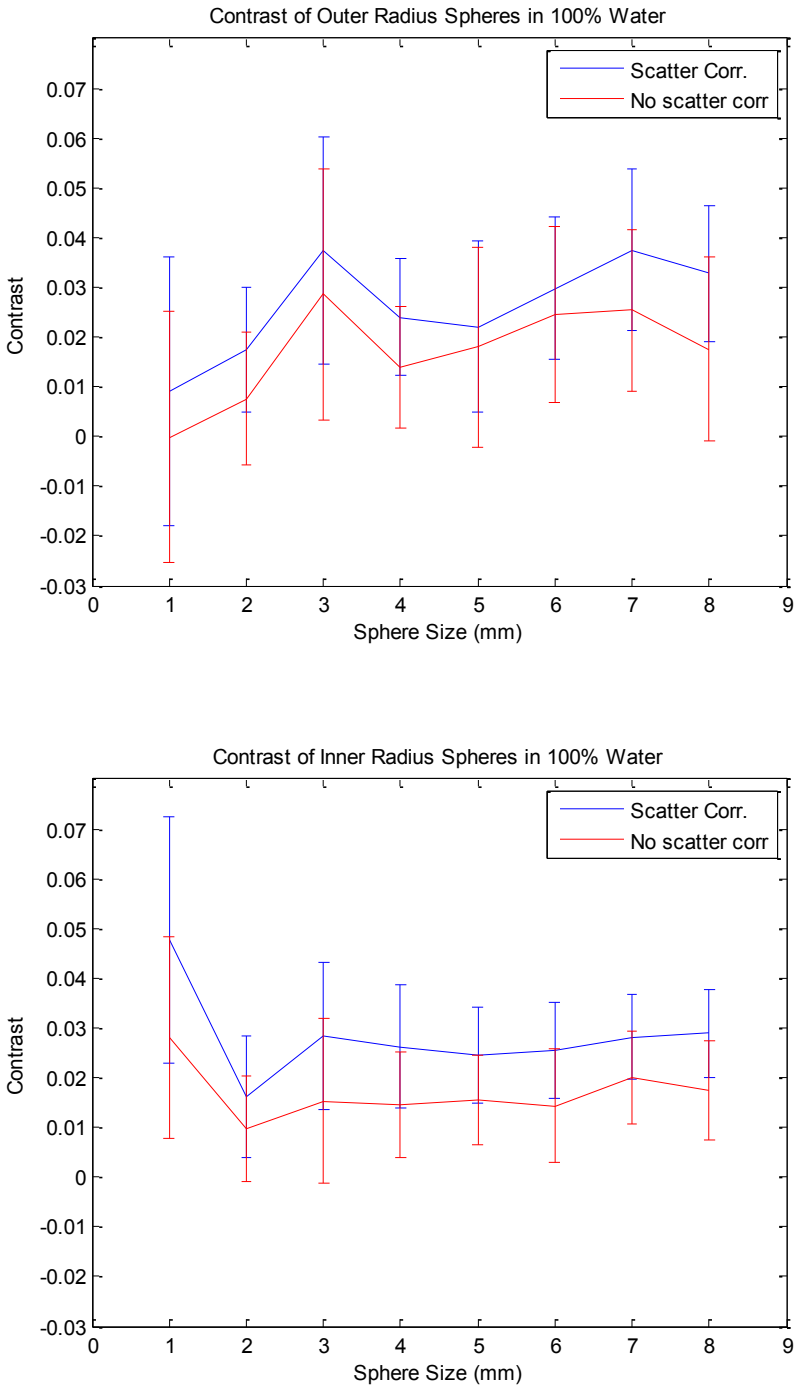

Figure 3-17: Contrast plots for (TOP) outer radius spheres (BOTTOM) inner radius spheres in 100% water.

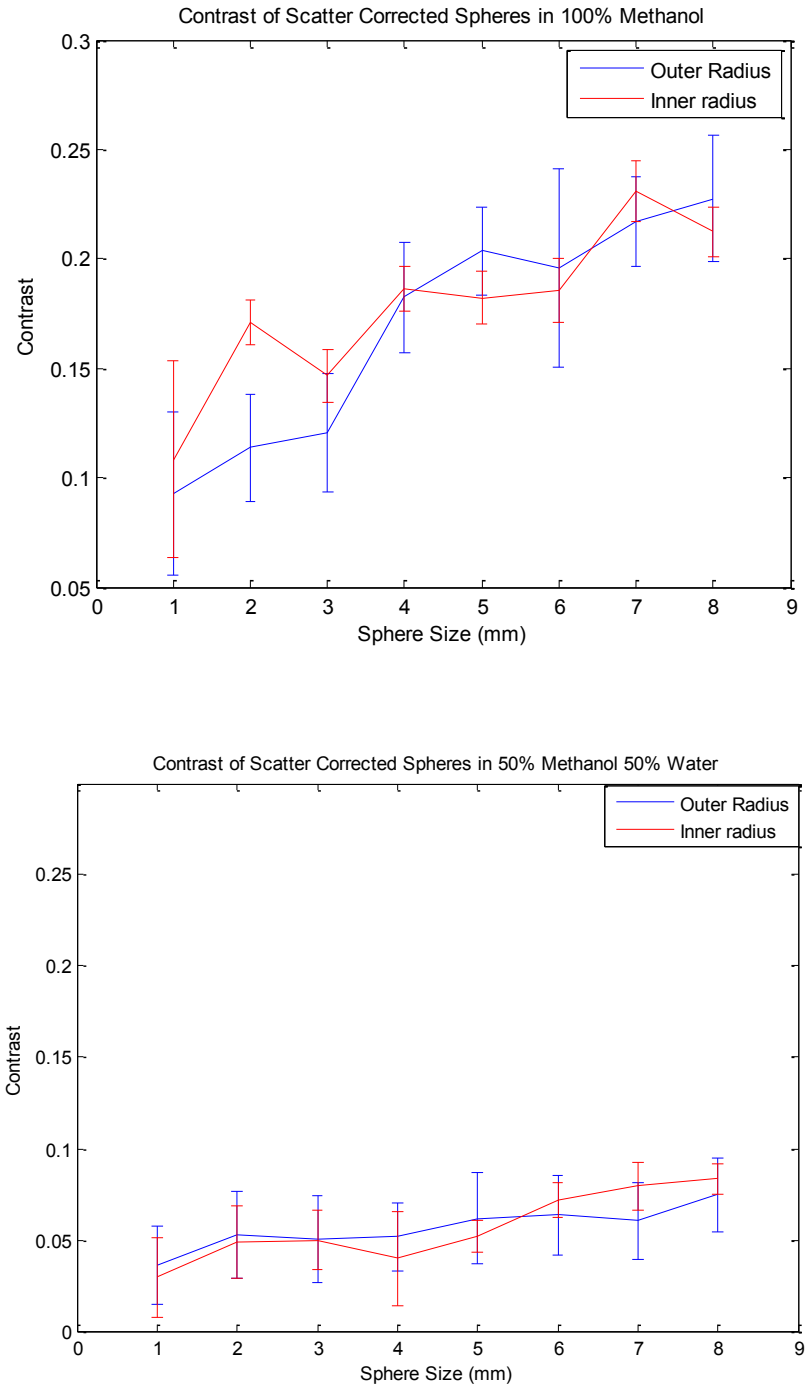

Figure 3-18: Comparison of contrast in inner and outer radius for scatter corrected images in (TOP) 100% Methanol (BOTTOM) 50% water 50% methanol.

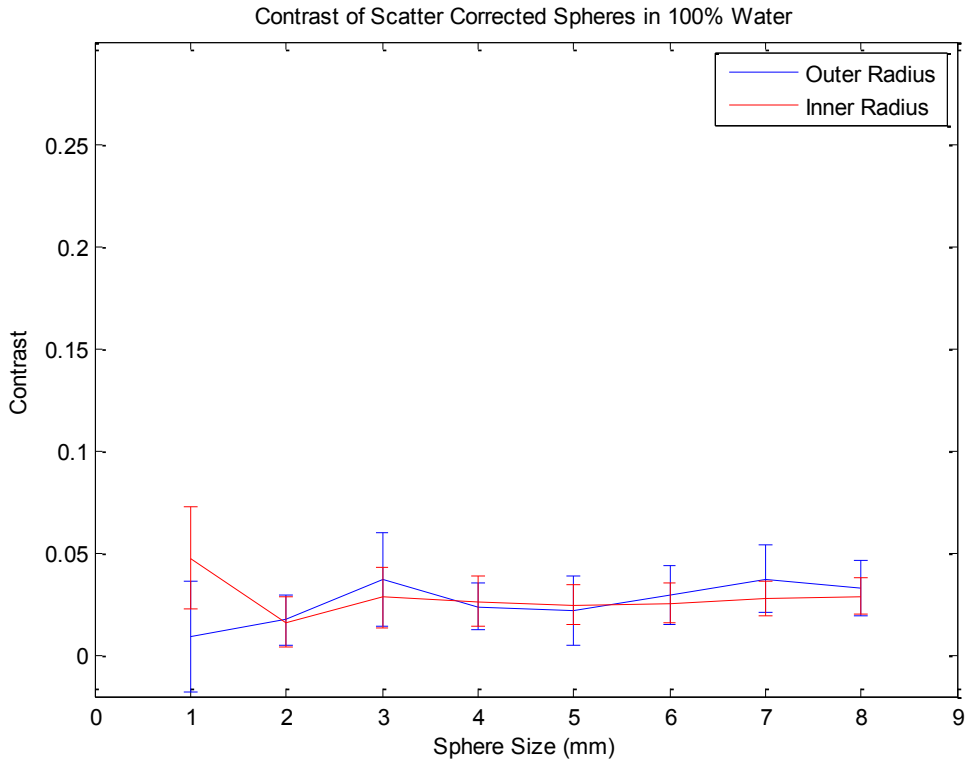

Figure 3-19: Comparison of contrast in inner and outer radius for scatter corrected images in 100% Water.

3.4 Detectability Observer Study

The results of the observer study show the smallest sphere detected in each concentration under the various phantom configurations (Figure 3-20). It was found that the most spheres were detected with the smallest variance in 100% methanol, and fewer and larger spheres were detected in 50-50 and 100% water. Only 4 spheres on average (down to 5 mm in one case) were seen in the 100% water phantom configuration.

A comparison of the smallest sphere detected in uniform vs. yarn, inner vs. outer radius and scatter vs. non-scatter corrected was made for each concentration examined. A paired 2-tail student t-test using 24 degrees of freedom (df) which come from 25 cases for each configuration (5 data repetitions x 5 observes) was made to check for statistical significance between each pair of dependent conditions (Table 3-1, 7). The t-test revealed no statistically significant differences between the smallest observable spheres seen in the yarn vs. uniform condition, except for the 50-50 concentration spheres in the outer radius without scatter correction (Figures 3-21,22,23,24). There were also no statistical differences between the smallest observable spheres seen in the inner or outer radius except for the 50-50 concentration spheres in uniform background under scatter correction (Figure 3-25,26). Finally the t-test showed there were no obvious qualitative differences between the average smallest observable spheres in scatter corrected verse non-scatter corrected conditions for all densities (Figure 3-27). A table summarizing the results lists only two conditions that had statistically significant differences (Table 3-8).

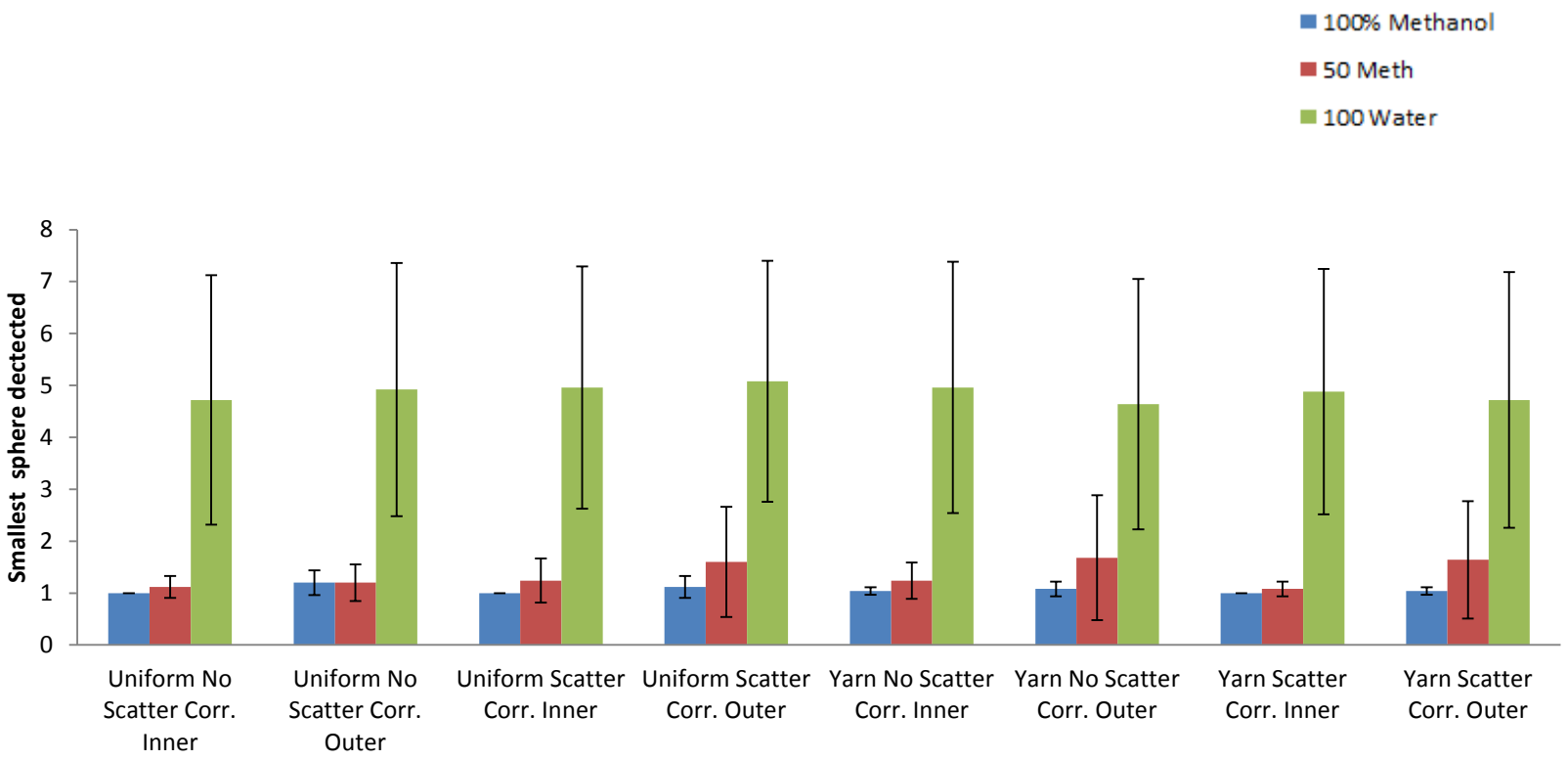

Figure 3-20: Summary of Observer detectability study for smallest sphere detected in each phantom configuration.

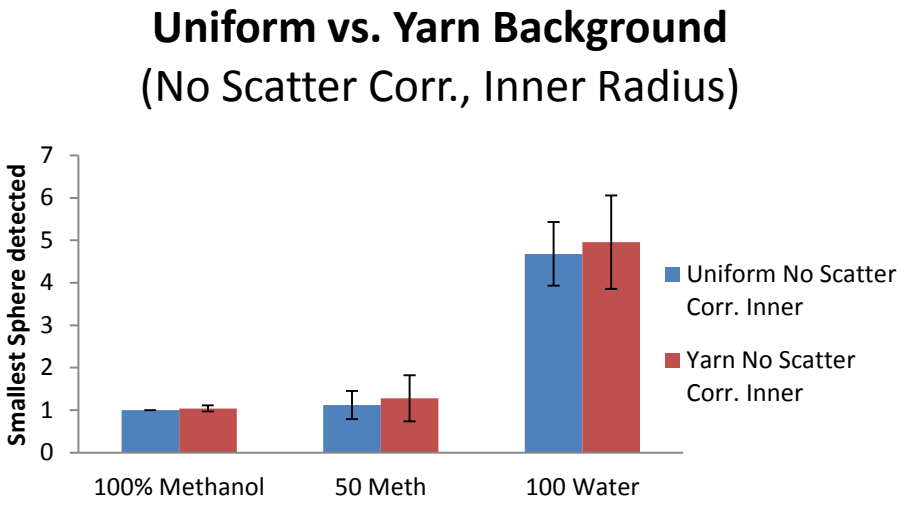

Figure 3-21: Comparison of smallest sphere detected in uniform vs. yarn background for three concentrations. For comparison, both cases were not scatter corrected and the inner radius location was used. Error bars represent standard error over 5 observers.

Table 3-1: Summary of paired two tail student t-test for uniform vs. yarn background detectability for inner radius spheres with no scatter correction.

	100% Meth.	50% Meth. 50% Water	100% Water
2 tail p value	0.3273	0.1034	0.1832
t	1.0000	1.6928	1.3706
Difference of means	-0.04	-0.16	-0.28
95% CI	-0.12 to 0.04	-0.36 to .04	-0.70 to 0.14
Standard error of Difference	0.040	0.095	0.204
df	24	24	24

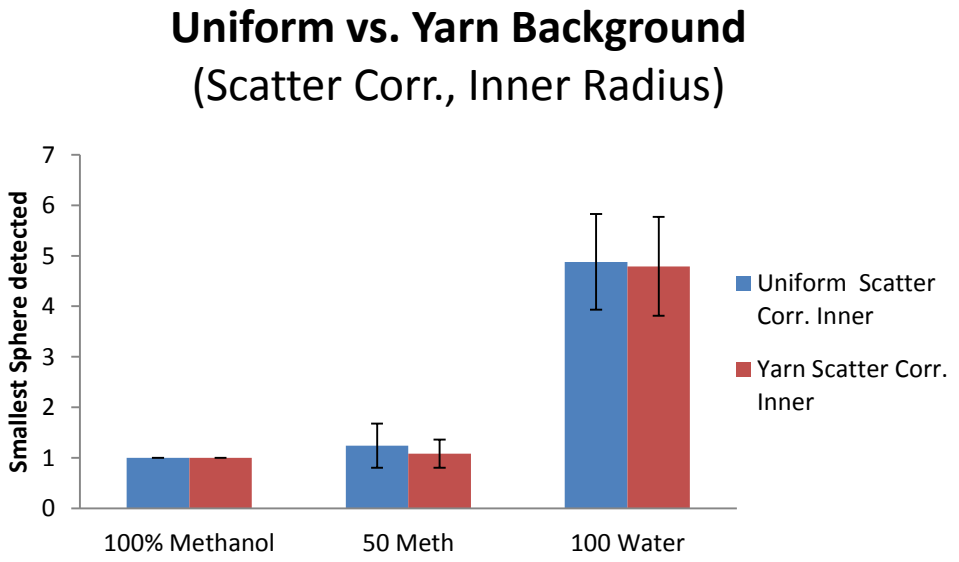

Figure 3-22: Comparison of smallest sphere detected in uniform vs. yarn background for three concentrations. For comparison, both cases were scatter corrected and the inner radius location was used. Error bars represent standard error over 5 observers.

Table 3-2: Summary of paired two-tail student t-test for uniform vs. yarn background detectability for inner radius spheres under scatter correction.

	100% Meth.	50% Meth. 50% Water	100% Water
2 tail p value	NA	0.1034	0.7466
t	NA	1.6928	0.3271
Difference of means	0	0.16	0.08
95% CI	NA	-0.04 to 0.36	-0.44 to 0.61
Standard error of Difference	0	0.095	0.255
df	24	24	24

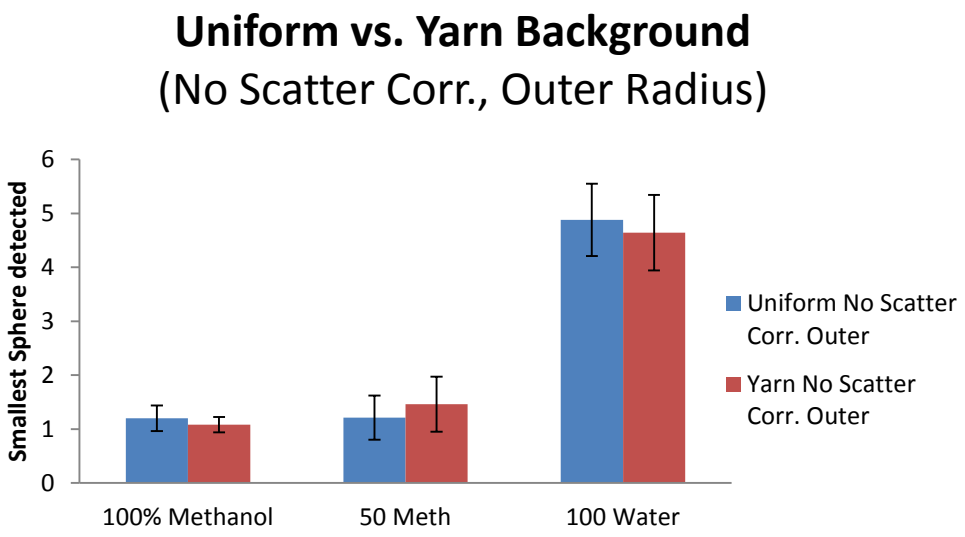

Figure 3-23: Comparison of smallest sphere detected in uniform vs. yarn background for three concentrations. For comparison, both cases were not scatter corrected and the outer radius location was used. Error bars represent standard error over 5 observers.

Table 3-3: Summary of paired two-tail student t-test for uniform vs. yarn background detectability for outer radius spheres without scatter correction.

	100% Meth.	50% Meth. 50% Water	100% Water
2 tail P value	0.3277	0.0109 *	0.0559**
t	1.0000	2.7689	2.0093
Difference of means	0	-0.25	0.24
95% CI	-0.04 to 0.13	-0.44 to -0.06	-0.01 to 0.4
Standard error of Difference	0.042	0.090	0.119
df	24	24	24

*Difference is statistically significant

** Difference is not quit statistically significant

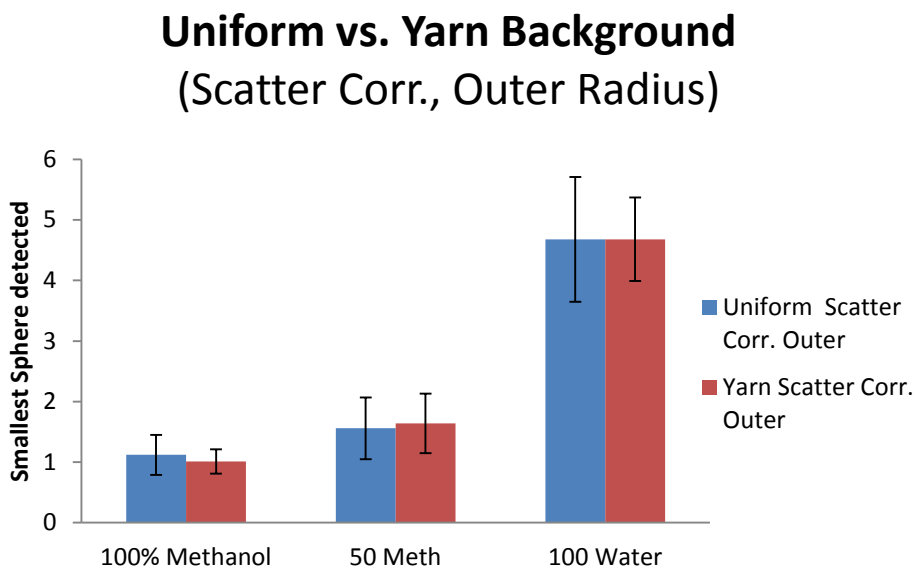

Figure 3-24: Comparison of smallest sphere detected in uniform vs. yarn background for three concentrations. For comparison, both cases were scatter corrected and the outer radius location was used. Error bars represent standard error over 5 observers.

Table 3-4: Summary of paired two-tail student t-test for uniform vs. yarn background detectability for outer radius spheres under scatter correction.

	100% Meth.	50% Meth. 50% Water	100% Water
2 tail P value	0.1615	0.454	1.000
t	1.4446	0.8109	0.0000
Difference of means	0.08	-0.08	0.00
95% CI	-0.03 to 0.19	-0.28 to 0.12	-0.48 to 0.46
Standard error of Difference	0.055	0.099	0.231
df	24	24	24

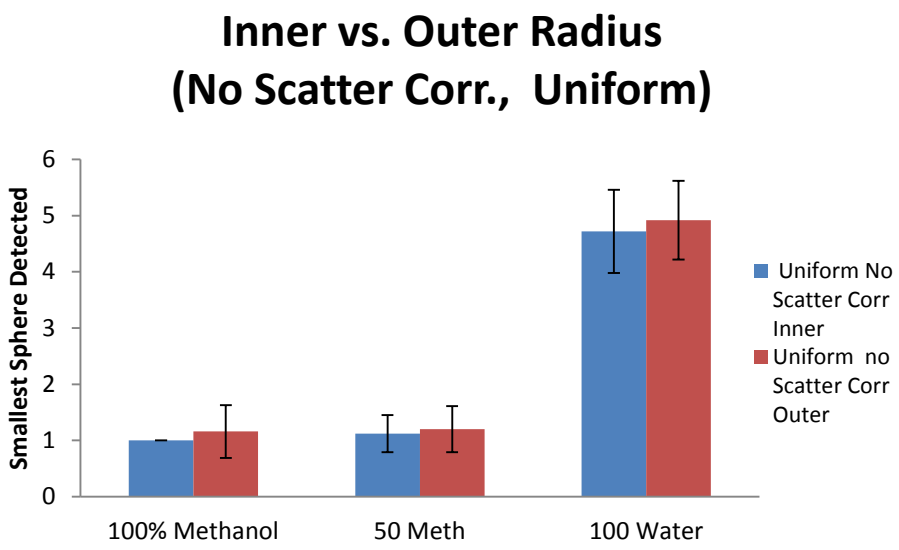

Figure 3-25: Comparison of smallest sphere detected in inner vs. outer radius for three concentrations. For comparison, both cases were in uniform background and images were not scatter corrected. Error bars represent standard error over 5 observers.

Table 3-5: Summary of paired two-tail student t-test for detectability of smallest sphere in inner vs. outer radius in uniform background without scatter correction.

	100% Meth.	50% Meth. 50% Water	100% Water
2 tail P value	0.1034	0.1615	0.1344
t	1.6928	1.4446	1.5492
Difference of means	-0.16	-0.08	-0.20
95% CI	-0.36 to 0.04	-0.19 to 0.03	-0.47 to 0.07
Standard error of Difference	0.095	0.055	0.129
df	24	24	24

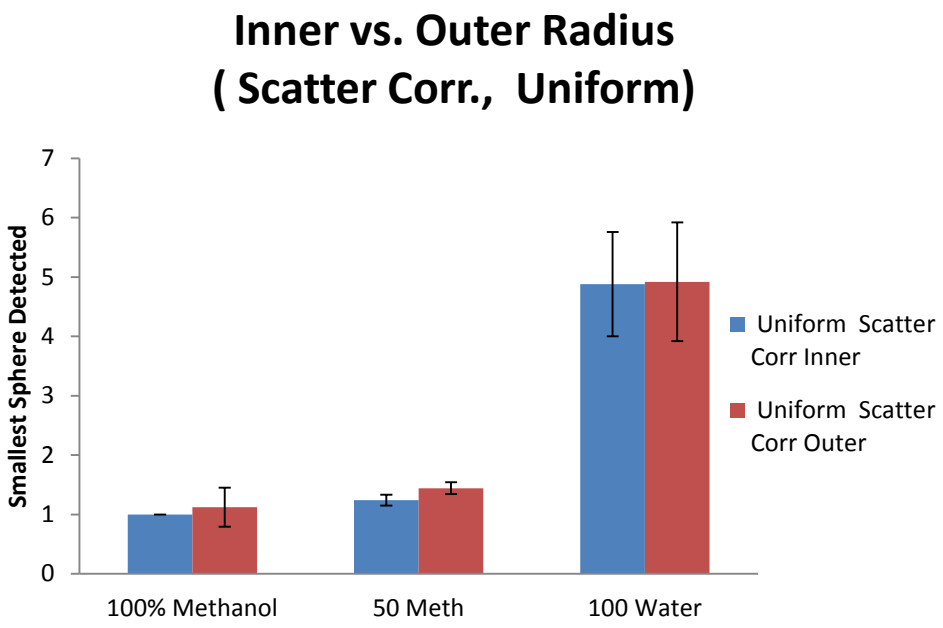

Figure 3-26: Comparison of smallest sphere detected in inner vs. outer radius for three concentrations. For comparison, both cases were in uniform background and images were scatter corrected. Error bars represent standard error over 5 observers.

Table 3-6: Summary of paired two-tail student t-test for detectability of smallest sphere in inner vs. outer radius in uniform background under scatter correction.

	100% Meth.	50% Meth. 50% Water	100% Water
2 tail P value	0.0830	0.0220*	0.6639
t	1.8091	2.4495	0.4399
Difference of means	-0.12	-0.20	-0.04
95% CI	-0.26 to 0.02	-0.37 to -0.03	-0.47 to 0.07
Standard error of Difference	0.066	0.082	0.091
df	24	24	24

*Difference is statistically significant

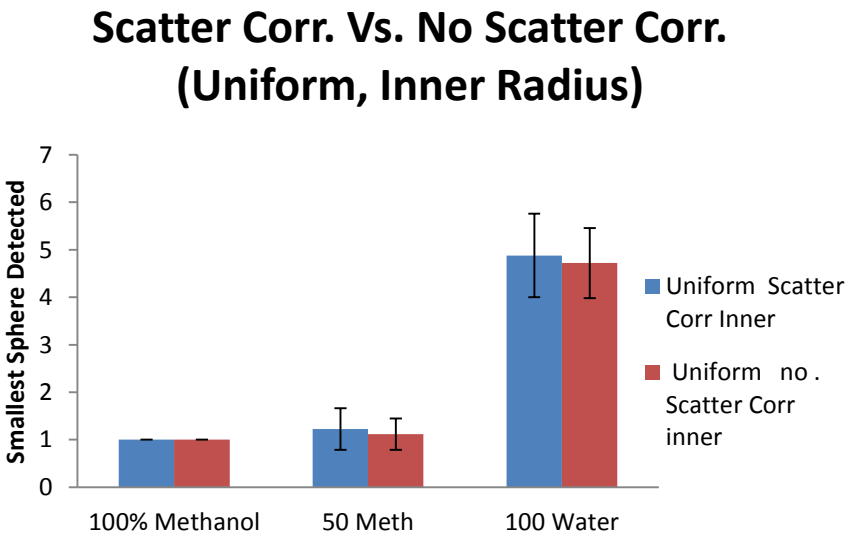

Figure 3-27: Comparison of smallest sphere detected under scatter and non-scatter corrected conditions for three concentrations. For comparison, both cases were in uniform background and inner radius location was used. Error bars represent standard error over 5 observers.

Table 3-7: Summary of paired two-tail student t-test for detectability of smallest sphere under scatter and non-scatter corrected conditions in uniform background for inner radius spheres.

	100% Meth.	50% Meth. 50% Water	100% Water
2 tail P value	NA	0.0830	0.4048
t	NA	1.8091	0.8480
Difference of means	0	0.12	0.16
95% CI	NA	-0.02 to 0.26	-0.23 to 0.55
Standard error of Difference	0	0.066	0.189
df	24	24	24

Table 3-8: Summary: Statistically significant difference found in 2 pairs of the multiple comparisons performed using paired two-tail student t-test between various phantom configuration pairs.

Pair
50% Meth 50% water Uniform No Scatter Corr. Outer vs. 50% Meth 50% water Yarn No Scatter Corr. Outer
50% Meth 50% water Uniform Scatter Corr. Inner vs. 50% Meth 50% water Uniform No Scatter Corr. Inner

3.5 2-AFC Observer Study

Figures 3-28 through 3-31 denote the probability of detection and detectability index of sphere sizes 1-6 mm in 50% methanol 50% water, and 100% water concentration. As can been seen from the plots of detectability index, probability of detection values below 50% or above 95% are not plotted in accordance with Table 2-2. Error bars were calculated from eq. 2.2 and 2.3 for plots of probability of detection and detectability index respectively. From these results we were able to determine which spheres had greater than 90% probability of detection and JND values.

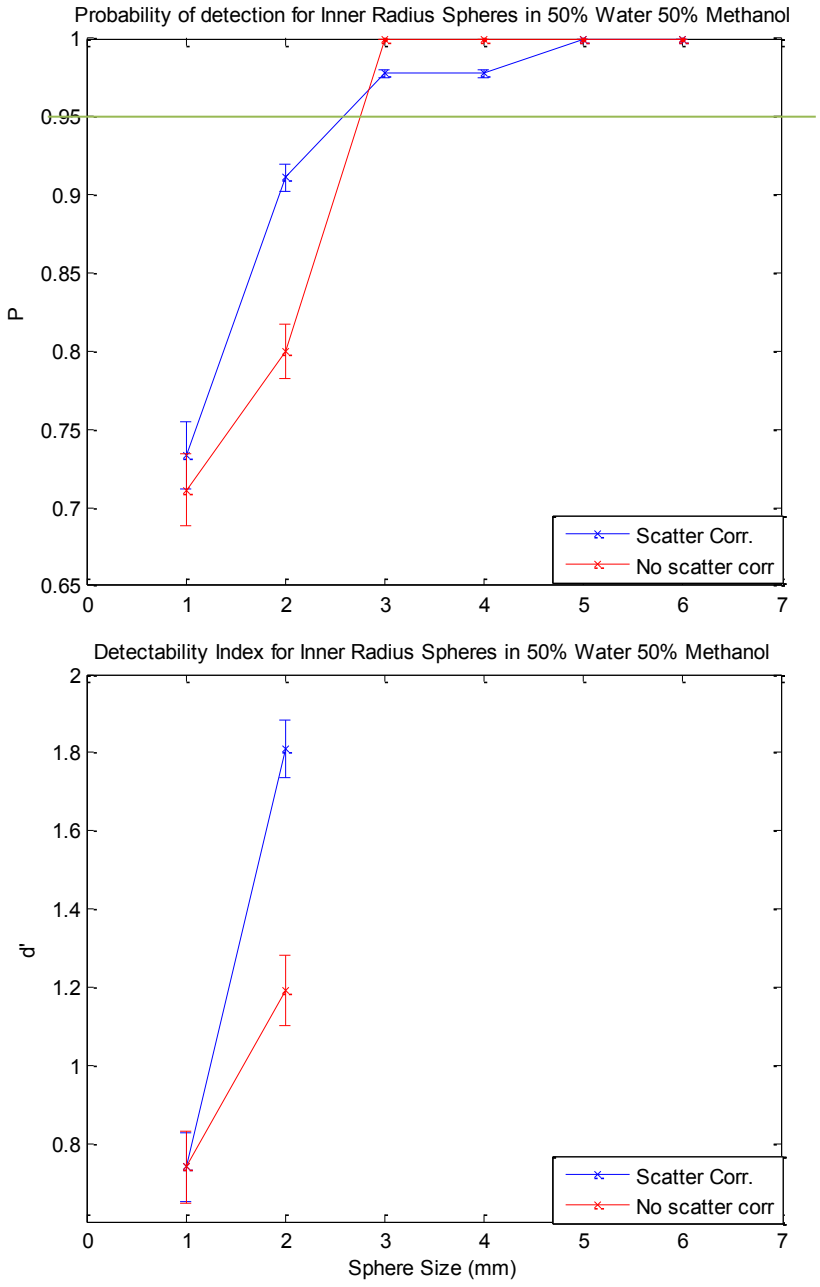

Figure 3-28: Results of the 2-AFC study for the inner radius spheres in uniform 50% water 50% methanol in terms of (TOP) probability of detection and (BOTTOM) detectability index, using transformation of probability values. P values above green bar do not have d' transformations.

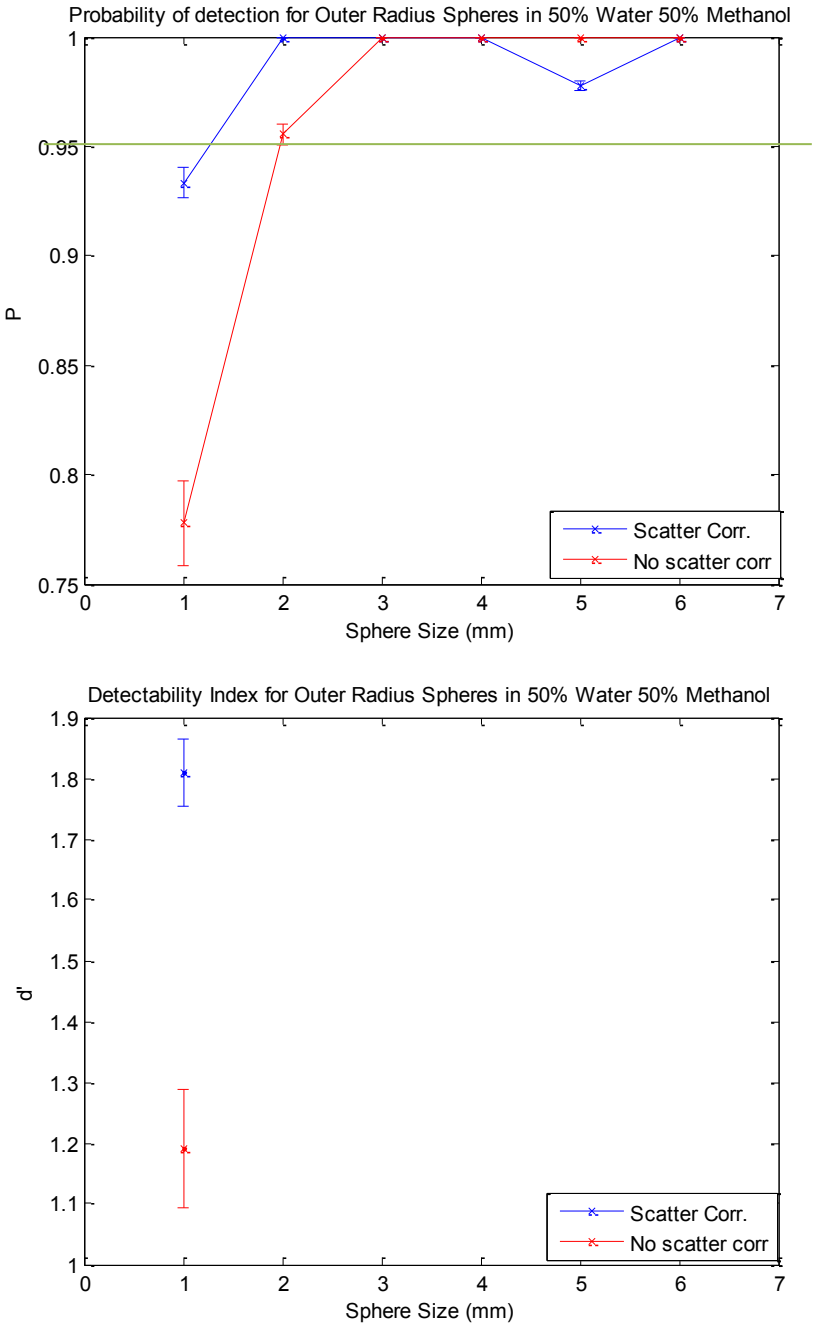

Figure 3-29: Results of the 2-AFC study for the outer radius spheres in uniform 50% water 50% methanol in terms of (TOP) probability of detection and (BOTTOM) detectability index, using transformation of probability values. P values above green bar do not have d' transformations.

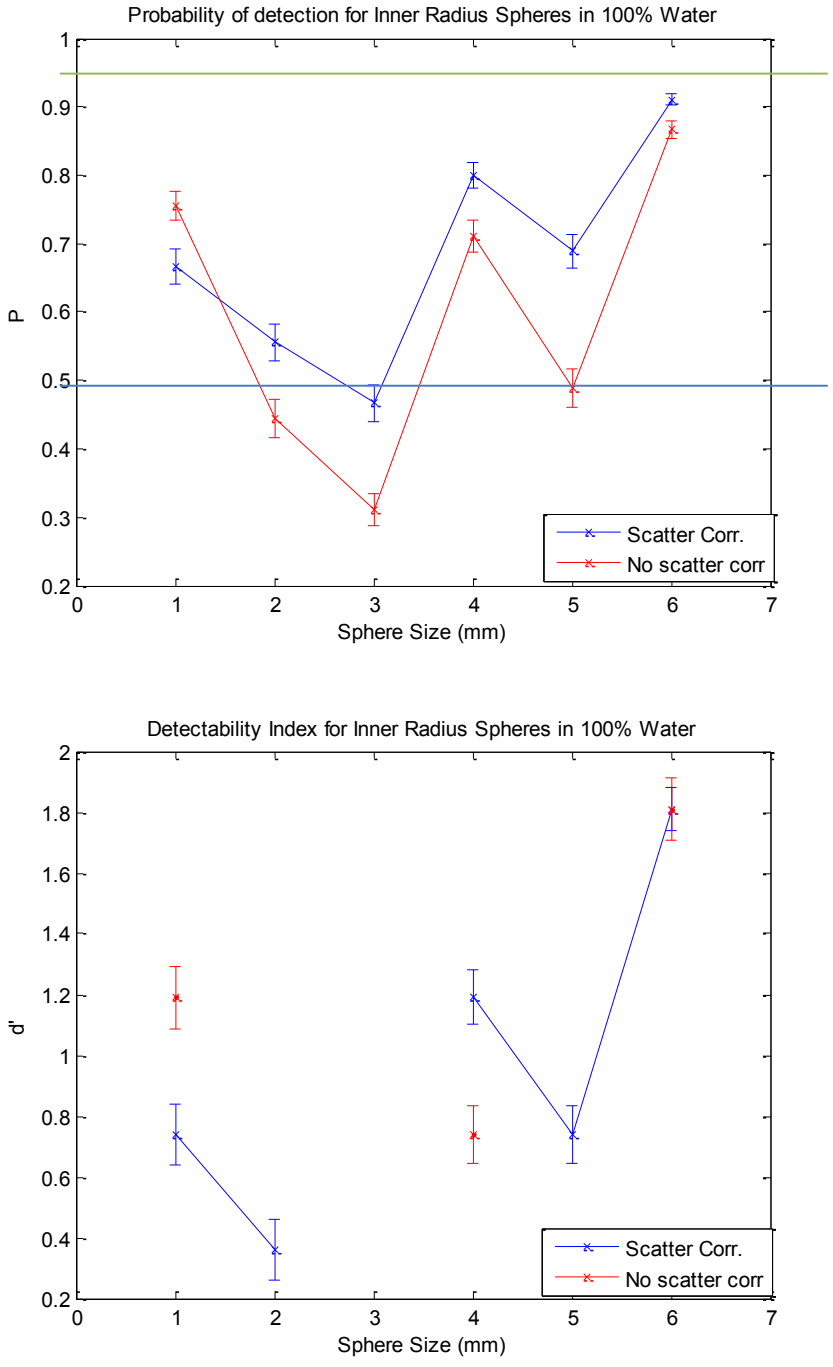

Figure 3-30: Results of the 2-AFC study for the inner radius spheres in uniform 100% water in terms of (TOP) probability of detection and (BOTTOM) detectability index, using transformation of probability values. P values above green bar or below blue bar do not have d' transformations.

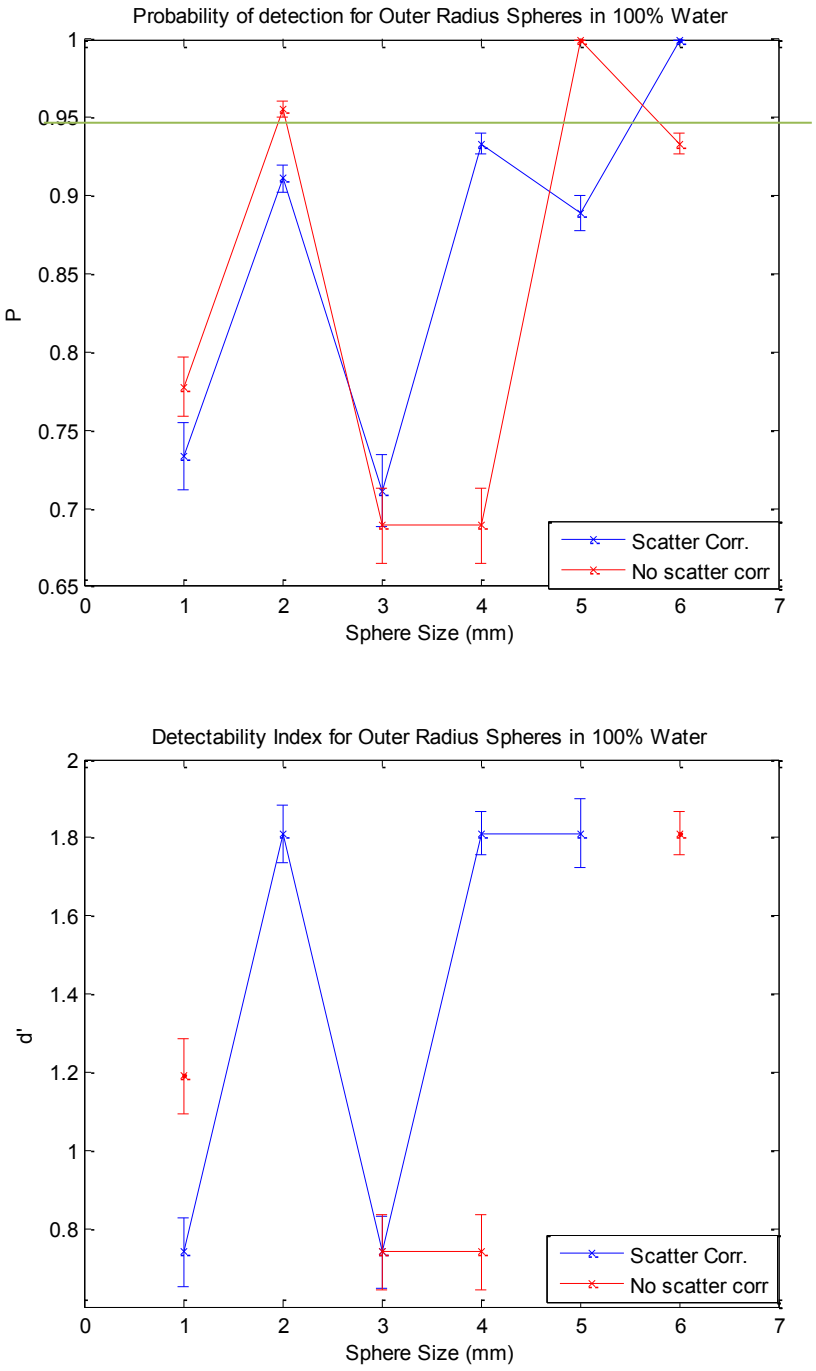

Figure 3-31: Results of the 2-AFC study for the outer radius spheres in uniform 100% water in terms of (TOP) probability of detection and (BOTTOM) detectability index, using transformation of probability values. P values above green bar do not have d' transformations.

3.6 Statistical Analysis of 2-AFC Observer Study

3.6.1 Effects of factors on Signal Detection

Tables 3-9 through 3-13 summarize the results of the chi-squared test on the 2-AFC data to determine how significant each factor was in the overall outcome of the study. As described in section 2.9.3, the significance of scatter correction on the detection task using the chi-squared test was determined by measuring the total number of scatter and non-scatter corrected cases detected independent of size, concentration (contrast), reader, and location. Additionally, the chi-squared results on the effect of concentration (independent of signal size, scatter correction, location and reader), size (independent of scatter correction, concentration, location, and reader), location (independent of scatter correction, concentration, size, and reader), and the inter-observer variability (independent of scatter correction, concentration, location, and size) are summarized in this section for the 2-AFC study.

Table 3-9 Table indicating total number of scatter and non-scatter corrected cases, independent of size, location, concentration, and reader. The resultant Chi square, χ^2, p-value indicates marginal significance between scatter and non-scatter corrected detection of signals.

Scatter correction	**Not Detected**	**Detected**	χ^2, **p-value**
No correction	185	895	0.043*
Correction	150	930	

*Marginally significant

Table 3-10 Table indicating total number of cases detected for 50%Methanol 50% water, and 100% water concentration, independent of size, location, scatter correction, and reader. The resultant Chi square, χ^2, p-value indicates highly significance difference between scatter and non-scatter corrected detection of signals.

Water Concentration	**Not Detected**	**Detected**	χ^2, **p-value**
50%	65	1015	< 0.0001*
100%	270	810	

*very highly significant

Table 3-11 Table indicating total number of cases detected for each sphere size, independent of concentration, location, scatter correction, and reader. The resultant Chi square, χ^2, p-value indicates highly significance difference between the detection of different sphere sizes.

Size	**Not Detected**	**Detected**	χ^2, **p-value**
1	88	272	< 0.0001*
2	63	297	
3	92	268	
4	38	322	
5	43	317	
6	11	349	

*very highly significant

Table 3-12 Table indicating total number of inner and outer radius cases detected, independent of size, scatter correction, concentration, and reader. The resultant Chi square, χ^2, p-value indicates highly significant difference between signal detection in inner and outer radius.

Location	**Not Detected**	**Detected**	χ^2, **p-value**
Outer	105	975	<0.0001*
Inner	230	850	

*very highly significant

Table 3-13 Table indicating the performance of each observer for 240 signals presented. The resultant Chi square, χ^2, p-value indicates no significant difference in the inter-observer performance.

Observer	Not detected	detected	χ^2, **p-value**
1	27	213	0.19
2	45	195	
3	39	201	
4	48	192	
5	40	200	
6	33	207	
7	37	203	
8	31	209	
9	35	205	

4. Discussion, Conclusions, and Future Direction

In this research work, the image quality of a dedicated research breast cone beam CT system was evaluated under scatter and non-scatter corrected conditions for a variety of breast compositions. Both quantitative metrics and observer studies were used to objectively characterize the image quality. The quantitative analysis of the reconstructed images involved line profiles, calculation of non-uniformity indices, SNR and contrast. Detectability of different sized spheres under the different phantom configurations was quantified using both a detectability and 2-AFC observer study. Paired 2-tail t-test analyses were performed on the data from the detectability observer study to determine statistical significance between a pair of dependent conditions. A chi-squared test was performed on the 2-AFC data to determine how significant each factor was in the overall outcome of the study. A maximum likelihood logistic regression model was determined, and the quality of fit was measured. The linear regression model gave the statistical significance of two- and three- factor interactions on the detectability response. From the 2-AFC study, we were also able to determine probability of detection and detectability index of 1-6 mm sphere sizes in two different background density phantom configurations.

4.1 Line profiles

As expected, the line profiles of scatter corrected images demonstrate higher attenuation values and increased contrast of the spheres (Fig. 3-2,4,6). This indicates that

the scatter-corrected attenuation values are closer to the true narrow beam values, as previously quantitatively verified [22]. The line profiles also indicate less cupping in the scatter-corrected cases for each density material (additionally verified by the non-uniformity index discussed in the next section). The line profile result is consistent with earlier results on scatter correction [22].

4.2 Non-uniformity

Non-uniformity was calculated to determine the degree of cupping for each simulated breast density under scatter and non-scatter correction conditions. As expected, non-scatter corrected images exhibited a higher degree (1.5-2.2 times more cupping than scatter corrected images) of cupping for each density used (Fig3-8). The degree of cupping differed depending on the density used: 100% water, which had the highest density of the three concentrations examined, had the highest degree of cupping in the non-scatter corrected case due to the beam hardening that results from the higher density. Non-uniformities other than the cupping artifact, mainly ring artifacts, resulted in a higher degree of variances in the measurements made. The absolute degree of cupping, moreover, could vary based on the choice of location and sizes of the ROIs used to determine the non-uniformity. In these cases, there was a consistent size and general location methodology used in order to minimize variability due to arbitrary selection of ROI size and location.

4.3 SNR

The plots of SNRs (Figs 3-10,13,16) illustrate the increase in noise that results by applying the scatter correction algorithm to the images. Based on mean SNR values, in both the 100% methanol and 50% methanol 50% water at both the inner and outer radii, SNRs of the non-scatter corrected images appear higher for all sphere sizes, however there is enough overlap of the error bars to indicate that the differences are not significant. The degradation of SNR when scatter correction is applied is due to the pixel-to-pixel fluctuations that get amplified when the log transform is applied in the reconstruction algorithm that yields attenuation values from projection intensity images.

For the 100% water concentration, the difference in SNR between scatter and non-scatter corrected signals appears to be far less than for the other concentrations. This indicates that for the signals in high density material, as seen in the 100% water concentration, the signal is equally masked by the image noise due to increased beam hardening artifacts and low contrast.

4.4 Contrast

The plots of contrast (Figs 3-11,14,17) indicate that better contrast is always achieved by correcting for scatter for all three concentrations tested. This is consistent with known improvements in contrast-resolution with CT imaging versus any planar imaging modality. Larger improvements in contrast (less overlap in error bars) are seen

for the lower density concentrations (100% methanol and 50% methanol 50% water). A comparison of contrast between inner and outer radius for scatter correction (Figs. 3-18,19) signify that there is better contrast in the inner radius for spheres smaller than 3mm in the 100% methanol (highest contrast), and improved contrast in the inner radius for spheres greater than 5 mm for the 50% methanol 50% water concentration as compared to the outer radius. There is too much overlap in the 100% water concentration to determine a difference in contrast between inner and outer radius.

4.5 Detectability Study

From the observer study, we found that the most spheres detected with the smallest variance (0-0.23) occurred in the least dense background (100% methanol), and fewer spheres were detected, 6.32-6.88 spheres detected for 50% Methanol 50% water and 3.93-3.28 for 100% water, (along with increasing variance) as background density increased (Fig. 3-20). All 8 spheres (down to 1mm diameter) were seen in the lower density cases, while only 4 spheres on average (down to 5mm in one case) were seen in the most dense background cases (Fig. 3-20). This result is consistent with our earlier results on detectability in various density breast phantoms [27].

The pared 2-tail t-test revealed no statistically significant differences between the smallest observable spheres seen in the yarn vs. uniform condition, except for the outer radius spheres in the 50-50 concentration without scatter correction (Figures 3-

21,22,23,24). There were also no statistical differences between the smallest observable spheres seen in the inner or outer radius except for the 50-50 concentration spheres in uniform background under scatter correction (Figure 3-25,26). Finally the paired 2-tail student t-test showed there were no obvious qualitative differences between the average smallest observable spheres in scatter corrected verse non-scatter corrected conditions for all densities (Figure 3-27). The cases where statistical significance was found (Table 3-8) could most likely be false positives since these statically significant differences were not seen across all densities examined. The possibility of statistically significant false positives was another reason for following up the detectability study with the 2-AFC study.

4.6 2-AFC study

4.6.1 Probability of detection and detectability index

From the 2-AFC study we were able to determine probability of detection and detectability index of sphere sizes 1-6 mm in 50% methanol 50% water, and 100% water concentration. For the 50% methanol 50% water concentration, spheres in the inner radius had greater than 90% probability of detection (P) of spheres greater than 2mm for scatter corrected images, and greater than 90% P of spheres greater than 3 mm in the non-scatter corrected case. 70% P or JND was achieved for 1mm scatter and non scatter corrected spheres also in the inner radius (Fig 3-28).

For outer radius spheres in the 50-50 concentration, greater than 90% P was achieved for spheres greater than 1 mm in the scatter corrected case and greater than 2 mm in the non-scatter corrected case. 1 mm spheres also in the outer radius had JND values in the non-scatter corrected images (Fig 3-29). The reason for better detectability in outer radius after scatter correction was due to beam hardening artifacts that have a detrimental effect, due most likely to residual cupping artifacts, on detectability of inner radius spheres.

In 100% water concentration, 90% P was achieved for the 6mm sphere in the inner radius under the scatter and non-scatter correction condition. JND was seen for inner radius spheres greater than 4 mm under scatter and non-scatter corrected conditions. P values for spheres below 3 mm were not considered due to high variance and high fluctuations of values between spheres 1 and 2 (Fig. 3-30).

For the outer radius spheres in 100% water, 90% P was seen for spheres greater than 4 mm in the scatter corrected case, and 90% P for spheres greater than 5mm for the non-scatter correct case. JND was seen for 3mm spheres in the scatter corrected case, and JND for 4 mm spheres in the non-scatter corrected case (Fig. 3-31).

The reason for better detectability in the outer radius after scatter correction in both concentrations examined was due to the cupping artifacts that have a detrimental effect on detectability of inner radius spheres.

4.6.2 Statistical Analysis of 2-AFC

The chi-squared test revealed the significance of each individual factor on the outcome of the study. From the chi-squared test it was determined that the scatter correction response was marginally significantly better than the non-corrected cases. The chi-squared test also revealed that the responses to the 50% methanol 50% water concentration were very highly significant ($p<0.0001$) as compared to the responses to the 100% water concentration. The effect of size was also found to be very highly significant ($p<0.0001$), with smaller spheres having worse performance. The responses to the spheres found in the outer radius were significantly better ($p<0.0001$) than the response to the detection of the inner spheres in both scatter and non-scatter corrected cases. And finally the chi-squared test found that overall inter-observer variability was not significant ($p<0.19$).

Dr. Choudhury, found appendix equation 1 as the best fit model for the linear regression analysis using AIC which incorporates maximum likelihood regression. This model measures the effect of the two-factor interactions between various factors of the study.

The relative contribution of the factors in the study was determined from the magnitude of the deviance of each factor. It was found that the largest contribution comes from concentration and size, with location being next. The contributions of reader and scatter correction appear minor by comparison (appendix Table 1).

To examine the significance of individual fitted terms, the estimation coefficients (log odds ratio) were considered in the model described in appendix equation 1, as well as their standard errors and significance. As shown in appendix table 1, the overall effect of size is significant, while the overall effect of scatter correction, concentration or location (inner or outer ring) was not significant. However interactions between these latter terms are highly significant. The only significant effect of scatter correction was with the 4 mm sphere, which perhaps occurred due to the noisy data.

Three factor interactions (Appendix Table 3), were also examined, but none were found to be significant.

4.7 Conclusion

For the first time, the image quality of scatter and non-scatter corrected images was quantitatively evaluated for the MMIL dedicated breast cone beam CT system. Through the use of line profiles, non-uniformity calculations, and contrast, it was determined that image quality improves with scatter correction. The analysis of SNR illustrates the increase of noise when images are scatter corrected. This increase in noise is due to relatively large pixel-to-pixel variations that results from applying the scatter correction. These pixel-to-pixel interactions are further amplified by taking the log transform of the attenuation values before the CT reconstruction. The increase of noise can be detrimental to signal detection for small low contrast spheres, however if contrast

is high and the spatial frequency of noise does not mask the spatial frequency of the sphere, then an overall increase in noise should not affect the detection of the signal.

In addition to quantifying the image quality with the metrics mentioned above, the effect of scatter correction on observer detection performance was determined with a detectability and 2-AFC observer study. Both studies indicate that better performance is achieved when signals are in the lower density background.

The detectability study had the main benefit that it indicated the smallest sphere seen in each simulated breast density, and also gave us insight into the effect of individual factors (radial location, structural background, scatter correction) on observer performance. On the other hand, the 2-AFC study allowed us to determine probability of detection and detectability index for each sphere size in two concentrations (100% water, and 50-50) where detectability of spheres was not obvious. We were also able to more thoroughly examine the statistical significance of all factors that affect observer response using chi squared analysis and a multivariate predictive model for probability of detection.

More specifically, from the detectability observer study it was determined that there were no statistical differences in detection of the smallest sphere in each simulated breast density between uniform and yarn, inner and outer radius, and scatter and non-scatter correction conditions, except for two cases which appeared to be false positives.

Using the multivariate predictive model for probability of detection with the 2-AFC results, it was found that concentration and size have the largest effect on response followed by location of the signal, with higher performance for the outer radius spheres. Scatter correction was found to have relatively little effect on observer performance. This model also indicated that the combined effect of concentration and size is highly significant, however scatter correction and size was found to be insignificant for all sphere sizes except for the 4 mm sphere size.

Additionally from the 2-AFC study, we determined the probability of detection and detectability index of sphere sizes 1-6 mm for both concentrations (100% water and 50-50) examined. For the lower density concentration, scatter correction did not play a role in the detection of spheres greater than 3 mm for the inner radius and 2 mm for the outer radius, but it was effective in improving performance for spheres less than 2 mm for both the inner and outer radius. For the higher density (100% water concentration), scatter correction improves the detectability of spheres greater than 3 mm for the inner radius and greater than 2 mm for the outer radius.

4.8 Recommendation

The quantitative analyses including line profiles, non-uniformity, contrast, probability of detection and detectability index do suggest an improvement in image quality when the images are scatter corrected. Moreover, using the results from the 2-

AFC, we can determine a range of SNR values needed to get P>90% and greater than JND for the two simulated breast densities examined. Figures 4-1 and 4-2 show the results of JND and 90% P superimposed on the SNR plots for 50-50 and 100% water concentrations. These plots denote possible SNR values, within the standard error of each mean, for the two breast densities simulated in the 2-AFC study to get P>90% and JND values. These results are noisy and results in large error bars. What could potentially be determined with better data is that we could measure the SNR of a suspected lesion in a breast of a particular density and project its detectability as either JND or greater than 90% without performing a human observer study.

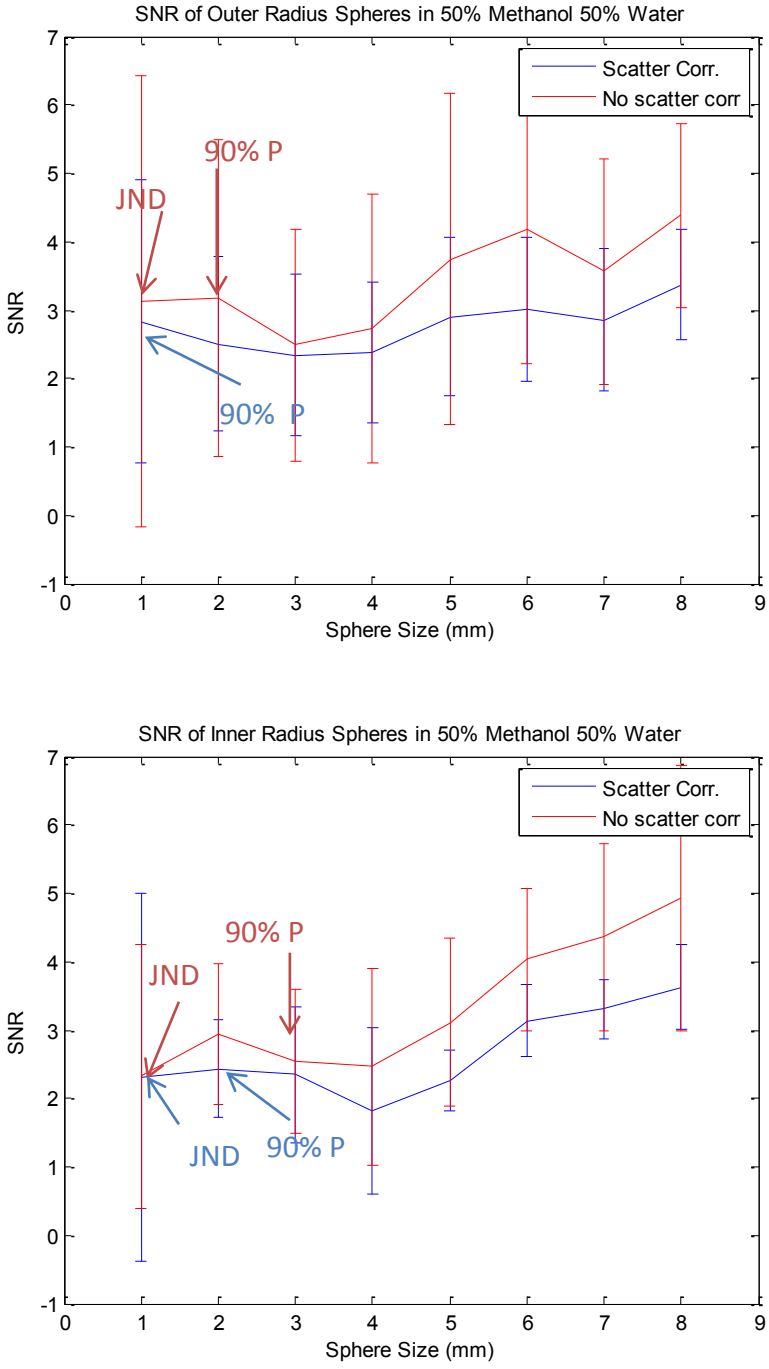

Figure 4-1: SNR Plots for (TOP) outer radius and (BOTTOM) inner radius spheres in 50% water 50% methanol, annotated to indicate at what sphere sizes 90% P and JND values start.

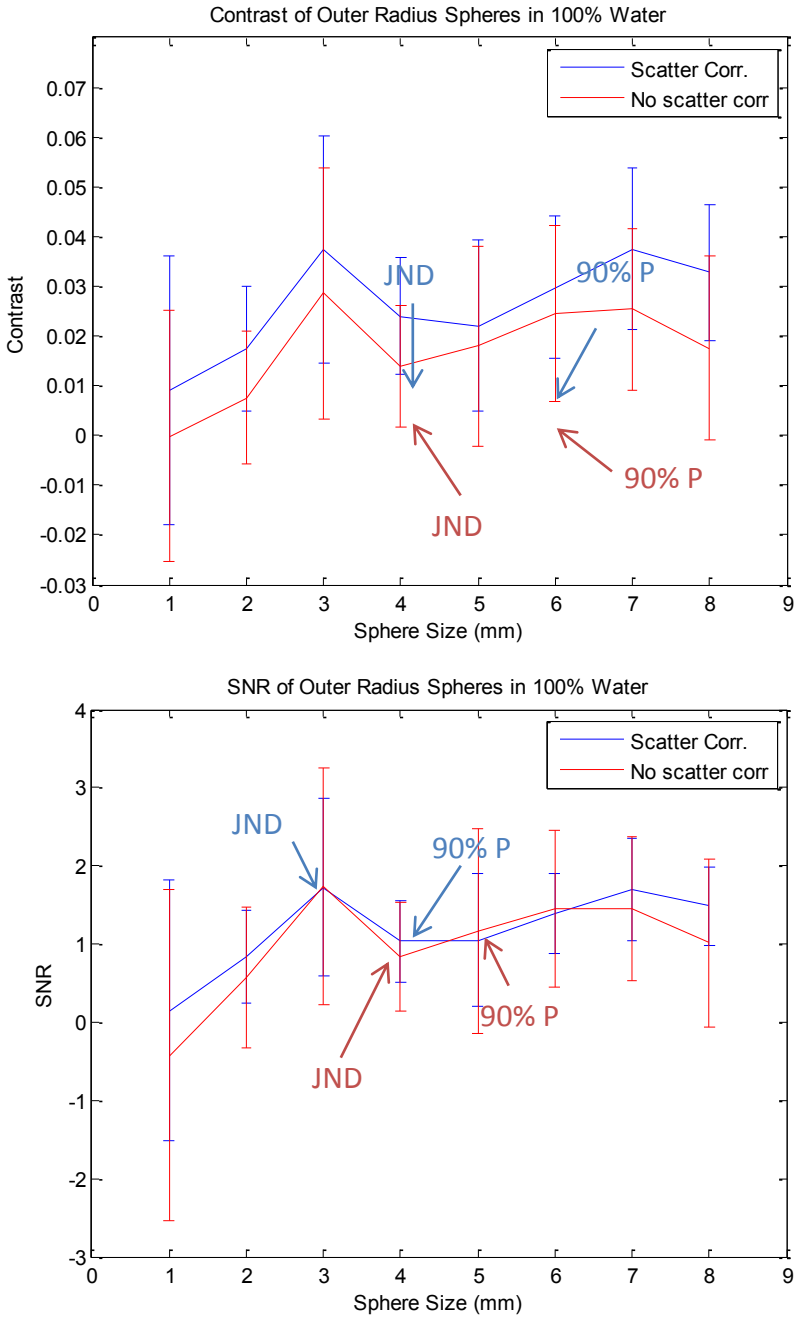

Figure 4-2: SNR Plots for (TOP) outer radius and (BOTTOM) inner radius spheres in 100% water, annotated to indicate at what sphere sizes 90% P and JND values start.

4.9 Future Directions

The ultimate goal of this study would be to determine SNR values that precisely correspond to measured values of JND and 90% P for a wide range of breast densities so that we could measure the SNR of a suspected lesion in a breast of a particular density and project its detectability as either JND or greater than 90% without performing a human observer study. To do this, we would like to determine the probability of detection and detectability index for a wider range of higher density concentrations. Based on the results of this study, concentrations with densities between 0.896 g/cm^2 (50% water 50% methanol) and 1 g/cm^2 (100% water) will give us detectability indices around JND. For completeness, we would also want to examine the detectability of the sphere sizes in densities above 1 g/cm even though we expect to see values below JND for spheres in densities greater than 100% water. We would also like to include more cases and more observers to more accurately determine statistical significance of observer response to scatter corrected cases. Finally we would like to apply better system performance characteristics (mainly better system resolution) as well as better data corrections to significantly improve image quality. Implementing such corrections would go a long way towards positively affecting the results of this current study.

Appendix

Modeling by logistic regression

Dr. Choudhury considered a variety of multivariate predictive models for the probability of detection, given the factors in the experiment. The response (outcome) was the odds of a detection and the predictor was some linear combination of the factors, including two and higher order interactions between factors. Models were fit by the method of maximum likelihood. Based on the quality of fit as measured by AIC [28], the following model was judged to be best fitting:

$$\begin{aligned} E\left[\log\frac{P\left(D_{ijklm}=1\right)}{P\left(D_{ijklm}=0\right)}\right] = a + b_{1i}\text{Reader}_i + b_{2j}\text{Size}_j + b_3\text{Conc}_k + b_4\text{Location}_l + b_5\text{Scatter}_m \\ + c_{1jk}\text{Size}_j : \text{Conc}_k + c_{2jk}\text{Size}_j : \text{Location}_l + c_{3jk}\text{Size}_j : \text{Scatter}_m \\ + c_{4jk}\text{Conc}_k : \text{Location}_l + c_{5jk}\text{Conc}_k : \text{Scatter}_m \\ + c_{5jk}\text{Location}_l : \text{Scatter}_m \end{aligned} \quad (1)$$

Here E stands for expected value (average), D_{ijklm} stands for the event of detection for the i-th Reader, i = 1,2,..,9, j-th size, j = 1,..,6, k-th concentration, k = 0, 1, l-th location, l = 0,1 and m-th scatter correction type, m = 0,1. Terms in the second row onwards of equation 1 denote two factor interactions between the various factors in the study. The interactions between readers and the other factors were not included because they weren't significant.

To examine the relative contribution of these terms to the predictive model, we considered the analysis of variance (ANOVA) appendix table 1. The factors with the greatest contribution were factors with the highest deviance per degree of freedom (df). The null deviance of this model, the deviance with no factors are added to the model, was 1863.8. The largest contributions appear to be for concentration and size, with location being next. The contributions of reader and scatter correction appear minor by comparison.

Table 1 Analysis of deviance for logistic regression model (Appendix eq. 1)

Term	**df**	**Deviance**
reader	8	11.26
scatter	1	4.36
Concentration	1	159.00
location	1	61.15
size	5	129.63
scatter: Conc.	1	0.07
scatter: location	1	0.30
scatter: size	5	8.74
Conc.: location	1	7.32
Conc.: size	5	69.83
location: size	5	33.67

To examine the significance of individual fitted terms, we considered the estimation coefficients (log odds ratios) in the logistic regression model (appendix eq. 1) as well as their standard errors and significance, in appendix table 2. Significance was determined at the standard p value of less than 0.05. From appendix table 2 we note that the overall effect of size is significant, while the overall effect of correction, concentration or location was not significant. However interactions between these latter terms are

highly significant. The only significant effect of scatter correction is with the 4mm sphere size.

Three factor interactions were also examined, however there were no three-factor interactions that were significant (Appendix Table 3).

Table 2: Estimated coefficients, standard errors and p-values for equation 1 in appendix.

	Estimate	**Std. Error**	**z value**	**P(>|z|)**
(Intercept)	1.7529	0.3680	4.76	0.0000
reader2	-0.7650	0.2964	-2.58	0.0098
reader3	-0.5357	0.3014	-1.78	0.0755
reader4	-0.8733	0.2944	-2.97	0.0030
reader5	-0.5753	0.3004	-1.91	0.0555
reader6	-0.2840	0.3085	-0.92	0.3572
reader7	-0.4547	0.3035	-1.50	0.1341
reader8	-0.1936	0.3115	-0.62	0.5343
reader9	-0.3709	0.3058	-1.21	0.2252
Scatter Correction	-0.0881	0.3464	-0.25	0.7993
water100%	0.2866	0.3713	0.77	0.4403
Location: Inner	-0.1164	0.3464	-0.34	0.7368
size2	2.5502	0.5708	4.47	0.0000
size3	2.1270	0.5396	3.94	0.0001
size4	2.6317	0.7806	3.37	0.0007
size5	4.2671	0.8939	4.77	0.0000
size6	3.7642	1.1373	3.31	0.0009
scatterCorrection:water100%	-0.2335	0.3523	-0.66	0.5073
Scatter Correction: location Inner	0.1569	0.2962	0.53	0.5962
scatterCorrection:size2	0.5934	0.4244	1.40	0.1621
scatterCorrection:size3	0.5526	0.4060	1.36	0.1735
scatterCorrection:size4	1.3360	0.4905	2.72	0.0065
scatterCorrection:size5	0.2502	0.4796	0.52	0.6019
scatterCorrection:size6	1.2340	0.7543	1.64	0.1018
water100%:location Inner	-0.6443	0.3752	-1.72	0.0859
water100%:size2	-1.4958	0.4518	-3.31	0.0009
water100%:size3	-3.2065	0.5145	-6.23	0.0000
water100%:size4	-3.0822	0.7898	-3.90	0.0001

water100%:size5	-3.0920	0.7890	-3.92	0.0001
water100%:size6	-2.1744	1.0940	-1.99	0.0469
locationInner:size2	-2.0766	0.5059	-4.10	0.0000
locationInner:size3	-0.3767	0.4099	-0.92	0.3580
locationInner:size4	0.3907	0.4797	0.81	0.4153
locationInner:size5	-1.6022	0.5574	-2.87	0.0040
locationInner:size6	-0.3948	0.7572	-0.52	0.6021

Table 3 Estimated coefficients, standard errors and p-values for three factor interactions.

	Estimate	**Std. Error**	**z value**	**P(> |z|)**
scatterCorrection:water100%:sizef2	-0.1874	0.9541	-0.20	0.8443
scatterCorrection:water100%:sizef3	3.0745	1.3390	2.30	0.0217
scatterCorrection:water100%:sizef4	-12.8279	1007.1316	-0.01	0.9898
scatterCorrection:water100%:sizef5	-15.2456	1023.6329	-0.01	0.9881
scatterCorrection:water100%:sizef6	1.3232	1635.4515	0.00	0.9994
scatterCorrection:locationInner:sizef2	0.8862	1.0612	0.84	0.4037
scatterCorrection:locationInner:sizef3	0.4264	0.8947	0.48	0.6337
scatterCorrection:locationInner:sizef4	-1.1052	1.0802	-1.02	0.3062
scatterCorrection:locationInner:sizef5	16.7144	1023.6320	0.02	0.9870
scatterCorrection:locationInner:sizef6	-15.8017	1280.9896	-0.01	0.9902
water100%:locationInner:sizef2	-0.7153	1.2926	-0.55	0.5800
water100%:locationInner:sizef3	-3.8173	1.3262	-2.88	0.0040
water100%:locationInner:sizef4	-15.9507	1007.1315	-0.02	0.9874
water100%:locationInner:sizef5	-33.7209	1447.6341	-0.02	0.9814
water100%:locationInner:sizef6	-17.3014	1513.9032	-0.01	0.9909

References

[1] "Global Breast Cancer Mortality Statistics - Mettlin - 2008 - CA: A Cancer Journal for Clinicians."*Wiley Online Library*. <http://onlinelibrary.wiley.com/doi/10.3322/canjclin.49.3.138/abstract>

[2] B. A. Miller, E. J. Feuer, and B. F. Hankey. "Recent Incidence Trends for Breast Cancer in Women and the Relevance of Early Detection: an Update." *CA: A Cancer Journal for Clinicians* (1993): 27-41.

[3] J. White "Breast Density and Cancer Risk: What Is the Relationship?" *J Natl Cancer Inst* 92.6 (2000): 443. Web.

[4]"Discovery Health "Mammogram Image Medical Dictionary"" <http://healthguide.howstuffworks.com/mammogram-picture-a.htm>

[5] L. Han, J. H. Hipwell, C. Tanner, Z. Taylor, T. Mertzanidou, S. Ourselin, D. J. Hawkes, Development of patient-specific biomechanical models for predicting large breast deformation, Physics in Medicine and Biology, vol 57, pp 455-472, 2012.

[6] A. Poulos, "The Application of Breast Compression in Mammography: a New Perspective."*Radiography* (2004): 131-37.

[7] "Radiation-Emitting Products." *What Are the Required Quality Control Tests for New Mammographic Modalities?* Web. 21 Apr. 2012. <http://www.fda.gov/Radiation-EmittingProducts/MammographyQualityStandardsActandProgram/Guidance/PolicyGuidanceHelpSystem/ucm143438.htm>.

[8] M. Kheng, M. Tea, and C. Grimma. "The Predictive Value of Suspicious Sonographic Characteristics in Atypical Cyst -like Breast Lesions." *Med Phys.*

[9] C. Kuzmiak, R. Dancel, E. Pisano, D. Zeng, E. Cole, M. Koomen, and R. Mclelland. "Consensus Review: A Method of Assessment of Calcifications That Appropriately Undergo a Six-Month Follow-up." *Academic Radiology* (2006): 621-29.

[10] "Left Breast Cyst on Mammogram MLO View | Flickr - Photo Sharing!" <http://www.flickr.com/photos/heitkamp/2599840242/>.

[11] M.B. McSweeney, P. Sprawls, R. L. Egan, Enhanced image mammography. Am J Roentgenol. 1983;140(1):9–14

[12] A. R. Fábio, L. F. Souza, C. Salmon, and D. N. Souza. "Breast Phantom with Silicone Implant for Evaluation in Conventional Mammography." *Journal of Applied Clinical Medical Physics* 12.1 (2011).

[13] C.A. Swann, D.B. Kopans, K.A. McCarthy, and G. White. "Mammographic Density and Physical Assessment of the Breast." *AJR Am J Roentgeno1* (1987): 525-26.

[14] J. L. Prince, and J. M. Links. *Medical Imaging Signals and Systems*. Upper Saddle River, NJ: Pearson Prentice Hall, 2006.

[15] "Helical CT & Lung Cancer." - *Science in Our World: Certainty & Controversy*. Web. 21 Apr. 2012. <http://www.personal.psu.edu/afr3/blogs/SIOW/2011/12/helical-ct-lung-cancer.html>.

[16] "Tomosynthesis System." *Tomosynthesis System*. Web. 19 Apr. 2012. <http://breast-cancer-research.com/content/10/3/209/figure/F5?highres=y>.

[17] A. Smith, "Full-field breast tomosynthesis." *Radiology management* 27.5 (2005) : 25-31.

[18] A.S. Chawla, *Correlation Imaging For Improved Cancer Detection*. Diss. Duke University, 2008. Print.

[19] TomoTherapy – Highly-Precise, Conformal Helical IMRT." *TomoTherapy - CT Image-Guided, Intensity-Modulated Radiation Therapy*. Web. 25 Apr. 2011. http://www.tomotherapy.com/difference/precision/

[20] D.J. Crotty, S.L. Brady, D.C. Jackson, G.I. Toncheva, C.E. Anderson, T.T .Yoshizumi, M.P. Tornai. 2011. "Evaluation of the Absorbed Dose to the Breast

Using Radiochromic Film in a Dedicated CT Mammotomography System Employing a Quasi-Monchroma.

[21] C. Kamphuis, and F. J. Beekman. "Accelerated Iterative Transmission CT Reconstruction Using an Ordered Subsets Convex Algorithm." *Medical Imaging, IEEE Transactions* 17.6 (1998): 1101-105.

[22] P. Madhav. 2010. Development and Optimization of a Dedicated Dual-Modality SPECT-CT System for Improved Breast Lesion Diagnosis. PhD Dissertation in Biomedical Engineering. Duke University, Durham, NC.

[23] J.H Siewerdsen, and D. A. Jaffray. "Cone-beam Computed Tomography with a Flat-panel Imager: Magnitude and Effects of X-ray Scatter." *Medical Physics* 28.2 (2001): 220. Print.

[24] Cherry, S. R., J. A. Sorenson, and M. E. Phelps, *Physics in Nuclear Medicine*. Philadelphia, PA: Saunders, 2003.

[25] P. Madhav, P., C. Li, M.P. Tornai,, ""Development of In Vivo Characterization of Breast Tissues Through Absolute Attenuation Coefficients Using Dedicated Cone-Beam CT." Proc. of SPIE 2010: Physics of Medical Imaging, 7622: (09-1)-(09-11

[26] A.E Burgess, "Comparison of Receiver Operating Characteristic and Forced Choice Observer Performance Measurement Methods." *Medical Physics* 22 (1995): 643-55.

[27] R.L. McKinley. 2006. Development and Characterization of a Dedicated Computed Mammotomography System. PhD Dissertation in Biomedical Engineering. Duke University, Durham, NC.

[28] Akaike Information Criterion." *Wikipedia*. Wikimedia Foundation, 05 May 2012. Web. 05 May 2012.
<http://en.wikipedia.org/wiki/Akaike_information_criterion>

Biography

Name

Jan Harwin Pachon

Place of Birth

Bogota, Colombia

Education

Medical Physics Graduate Program, Duke University, Durham Master 2012

Dept. of Biomedical Engineering, Washington University in St. Louis, Bachelors of Science May 2009

Dept. of Physics, Loyola University in Chicago, Bachelors of Science May 2007

Papers/ conferences

[1] KL Perez, SD Mann, **JH Pachon**, P Madhav, MP Tornai. "Is SPECT or CT Based Attenuation Correction More Quantitatively Accurate for Dedicated Breast SPECT Acquired with Non-Traditional Trajectories?" Presented at *2010 Nuclear Science Symposium & Medical Imaging Conference*, Knoxville, TN, 30 Oct. – 6 Nov. 2010, and published in *2010 IEEE Conference Record NSS/MIC*, 2319-2324.

[2] KL Perez, SD Mann, **JH Pachon**, P Madhav, MP Tornai. "Is SPECT or CT Based Attenuation Correction More Quantitatively Accurate for Dedicated Breast SPECT Acquired with Non-Traditional Trajectories." Presented at *From Imaging to Understanding: Visualization and Smart Analysis*, Duke University Center for Molecular and Biomolecular Imaging Conference, Durham, NC, 12-13 December, 2010.

[3] **JH Pachon**, J Shah, P Madhav, MP Tornai. "Characterization of Image Quality for 3D Scatter Corrected Breast CT Images." Presented at the *SPIE Conf. on Medical Imaging*, 12-17 Feb. 2011, Orlando, FL, and published in *Proc. of SPIE 2011: Physics of Medical Imaging*, 7169: (58-1)-(58-8).

[4] J Shah, **JH Pachon,** P Madhav, MP Tornai. "Detailed Characterization of 2D and 3D Scatter-to-Primary Ratios of Various Breast Geometries Using a

Dedicated CT Mammotomography System." Presented at the *SPIE Conf. on Medical Imaging*, 12-17 Feb. 2011, Orlando, FL, and published in *Proc. of SPIE 2011: Physics of Medical Imaging*, 7169: (58-1)-(58-7).

[5] J Shah, **JH Pachon**, P Madhav, MP Tornai. "Detailed Characterization of 2D and 3D Scatter-to-Primary Ratios of Various Breast Geometries Using a Dedicated CT Mammotomography System." Presented at the *2011 BME Research Day*, 18 April, 2011, and the *3rd Annual Duke Medicine Research Career Day*, Durham, NC, 20 May, 2011.

[6] **J. H. Pachon**, Girijesh Yadava, Debashish Pal, Jiang Hsieh "Image Quality Evaluation of Iterative CT Reconstruction Algorithms: A Perspective From Spatial Domain Noise Texture Measures "Presented at the *SPIE Conf. on Medical Imaging*, 2012, San Diego, CA, and published in *Proc. of SPIE 2012: Physics of Medical Imaging*